Ultimate Resolution X-ray Spectroscopy of Chemical-Effects in Manganese Compounds

Inaugural-Dissertation
zur
Erlangung des Doktorgrades
der Mathematisch-Naturwissenschaftlichen Fakultät
der Universität zu Köln

vorgelegt von
Malkhaz Jabua
aus Zugdidi, Georgien

Jülich, 2016

Berichterstatter:

Prof. Dr. D. Gotta,
Prof. Dr. A. Zilges

ABSTRACT

High-resolution X-ray spectroscopy offers a powerful tool to study the complex inner-shell interactions of electrons. Corresponding effects are particularly pronounced in the case of $3d$ transition metals. Spectroscopic studies of compounds are widely used in order to obtain structural information both from energy shifts and line shapes by measuring valence-to-core or outer core-to-core transitions, *i. e.* investigating mainly Kβ transitions. Applying ultimate-resolution spectroscopy in a suitable measurement geometry may allow to extend such studies also to the inner core transition Kα, though effects are much smaller here. For cases where energy shift or line shape points to specific compound structures, Kα lines have the advantage being by far the most intense transitions of an element's characteristic X-radiation.

A sensitivity to small effects is accompanied by the need for energy calibrations to about $10\,\mathrm{meV}$ accuracy at energies in the few keV range. Therefore, the exact knowledge of the line shape is essential in order to associate a particular wavelength of the measured spectrum to serve as an X-ray standard, which in turn requires the exact knowledge of the spectrometer response. Typically, the peak value is chosen, where the measure for the accuracy is determined by the knowledge of the experimental response.

Measurements were done by using an ultimate-resolution Bragg spectrometer optimized for long-term high-statistics measurements. This type of spectrometer, equipped with spherically bent crystals, is set up at the Institut für Kernphysik at Forschungszentrum Jülich. The measurements benefit from a suitable choice of target geometry, crystal mounting, and the use of charge-coupled devices as two-dimensional position-sensitive X-ray detectors set up within a vacuum system.

The case study has been performed for a variety of compounds of manganese, which is the transition metal with the half filled $3d$ shell generally being a particular stable configuration for ionic compounds. Kα and Kβ X-ray emission spectra have been measured under identical conditions providing consistency checks with the numerous Kβ data.

Peak energies of the Kα and Kβ lines were measured as envisaged to a precision of $10 - 30\,\mathrm{meV}$ and an almost model-free parametrization of the line pattern was achieved because of the precise knowledge of the spectrometer response. Such a parametrisation may serve as testing ground for detailed theoretical considerations.

ZUSAMMENFASSUNG

Hochauflösende Röntgenspektrospie stellt ein wichtiges Werkzeug zum Studium der komplexen Vorgänge in den inneren Schalen der Atome dar. Die Effekte solcher Wechselwirkungen sind besonders stark ausgeprägt im Bereich der $3d$-Übergangselemente. Bei den Kβ-Übergängen sind spektroskopische Methoden weit verbreitet, um aus Energieverschiebungen und Linienbreiten Strukturinformationen für chemische Verbindungen abzuleiten. Für Kα Linien sollte dies mittels höchstauflösender Spektroskopie auch gelingen können, obwohl die Effekte hier wesentlich kleiner sind. Ein Vorteil ist jedoch, dass die charakteristische Kα-Strahlung am intensivsten ist.

Um auf kleinste Effekte sensitiv zu sein, müssen im einige keV-Bereich Energiebestimmungen mit einer Genauigkeit von ca. 10 meV erreicht werden. Für die Zuordnung einer Energie zu einer Linienstruktur bietet sich als ein ausgezeichneter Punkt das absolute Maximum an. Hierzu ist wiederum eine genaue Kenntnis der Auflösungsfunktion des Spektrometers erforderlich, um Ungenauigkeiten auf Grund der i. a. asymmetrischen Linienformen möglichst zu vermeiden.

Die Messungen wurden mit einem höchstauflösenden Bragg-Spektrometer durchgeführt, das für Langzeitmessungen optimiert ist. Das Spektrometer ist am Institut für Kernphysik des Forschungszentrum Jülich installiert und mit sphärisch gebogenen Kristallen ausgerüstet. Für diese Messungen wurde eine speziell optimierte Geometrie der Fluoreszenztargets und der Kristallhalterung benutzt und zum Nachweis der Röntgenstrahlung ein "charge-coupled device" (CCD) eingesetzt. Alle Komponenten waren in einem Vakuumsystem integriert.

Die Fallstudie wurde am einigen chemischen Verbindungen von Mangan durchgeführt. Mangan selbst ist das Übergangsmetall mit halb gefüllter $3d$-Schale, die i. a. bei ionischen Charakter der Verbindung eine besonders stabile Konstellation darstellt. Kα- und Kβ-Übergänge wurden unter identische Bedingungen gemessen, wodurch eine Überprüfung der experimentellen Ergebnisse an Hand der Vielzahl von Kβ-Daten möglich wurde.

Bei der Energiebestimmung der Kα- und Kβ-Linien wurden die angestrebten $10 - 30$ meV erreicht. Eine nahezu modellfreie Parametrisierung der Linienstruktur wurde möglich wegen der genauen Kenntnis der Auflösungsfunktion, die zum Vergleich mit theoretischen Rechnungen herangezogen werden kann.

Die hier vorgestellte Arbeit beschreibt, dass die Auflösung kleiner, von der jeweiligen chemischen Verbindung abhängiger Details der komplexen Innerschalenprozesse, auch beim Kα-Dublett möglich ist, wenn höchstauflösende Röntgenspektroskopie eingesetzt wird.

ACKNOWLEDGEMENTS

I would like to express my special appreciation and thanks to my supervisor Professor Dr. Detlev Gotta, for being a tremendous mentor for me, for the continuous support of my PhD study and related research, for his patience, motivation, and immense knowledge. His guidance helped me in all the time of research and writing of this thesis. I would like to thank you for encouraging my research and for allowing me to grow as a research scientist. Your advices and personal attitude during my research work have been valuable. I will never forget the first words of our very first dialogue: "don't call me Professor Gotta, just call me by name, we are colleagues here".

My sincere thanks also goes to Professor Dr. Dr. h.c. Hans Ströher, to the director of the Institute for Nuclear Physics at Forschungszentrum Jülich. For his effort to build strong scientific relationships between my home country, Georgia and Germany, for his permanent support that I was feeling through the whole time spent at research centre.

A special thank to Dr. Andro Kacharava, words cannot express how big his role is on my way starting as master student till now, at the end of my PhD study. He, as a kind of person was discovery for me. I could hardly imagine a person with so many positive and energetic characteristics. I can't remeber time, I entered his office on bad mood, overloaded with some negative thoughts and left without positive impressions. Besides being an excellent scientist I found him as a person with unique skills of communicating with people and spreading the positive "charge" among them. Thanks Andro for always being my great friend and supporter.

I would like to gratefully acknowledge Dr. Hubert Gorke, Dr. Norbert Dolfus and Dr. Irakli Keshelashvili for their intensive and inestimable advices and instructive talks and practical guidance. Without them it would be hardly imaginable to successfully deal with crystal spectometer and detector electronics. Special thanks to Dr. Claire Besson for the preparation of the chemical compounds, for her continuous and comprehensive support during my experiments.

A warm thanks to Dr. Christian Weidemann, Prof. Dr. Khalid Rashid and Dr. David Mchedlishvili who always provided me with smart advices in a very detailed shape. I cannot forget the inspirational scientific and private talks with Thomas Krings and Dr. Illhan Engin. Thank you for your amazingly supportive and friendly attitude.

I want to express my gratitude to all the members of the IKP of Forschungszentrum Jülich for their constant support and very familiar and positive atmosphere.

My warm gratitude to my family. I can't express how grateful I am to my mother, father, my brother, and my aunt for all of the sacrifices that they've made on my behalf. Your prayer for me was what sustained me thus far. I would like to explicitly thank all of my friends who heavily supported and encouraged me to strive towards my goal.

Special thanks to my German language teachers, for giving me the strong basis to communicate with my German friends on their own language and to feel the sole of this beautiful country.

To my wonderful grandma,
Vakona,

for her inspirational and motivational talks about the power of knowledge

CONTENTS

1. INTRODUCTION

The shell structure of the atomic levels becomes apparent by the emission of characteristic X-radiation. The wavelengths of at least the main transitions are unambiguously attributed to a particular element $A(Z, N)$ which is synonymous to the nuclear charge Z. Spectroscopic methods contributed significantly to the understanding of the properties of matter governed by the laws of quantum mechanics.

High-resolution X-ray spectroscopy offers a powerful tool to study the electronic structure of atoms and molecules. It was immediately realized, that the simple hydrogen-like approach of one electron moving in a mean electric field had to be modified by a shell-dependent screening and a complex electron-electron and electron-hole interaction. Even more complex are molecular spectra which include also the interaction with valence electrons from neighbouring atoms.

Precision studies of such radiation traces back to X-ray diffraction by crystals discovered by von Laue and his collaborators in 1912 which resulted in the development of two complementary areas of research, (i) the study of crystal structure using X-rays and (ii) the investigation of atomic structure by emission spectra to high precision using diffraction in crystals. An estimate of the wavelength of X-rays already existed and von Laue calculated that the atomic spacing in a solid was of comparable dimension. He considered that a crystal may act like a diffraction grating and, consequently, tried to pass a narrow beam of X-rays through a zinc blende crystal, resulting in a pattern of diffraction spots on a photographic plate.

In this work, the characteristic X-radiation from a medium Z nucleus, manganese, is studied. The transitions of such X-ray fluorescence in the few keV range have typically natural line width of the order of 1 eV. Hence, an energy resolution of the order of one electron volt (eV) or better is mandatory for precision studies which is achievable only with crystal spectrometers. In this energy range, reflection-type Bragg spectrometers have to be used in order to minimise absorption.

1.1. Motivation

The experiment described here originates from the need to make precise energy calibrations at energies in the few keV range for ultimate resolution measurements of X-rays from light exotic atoms [1–3]. Experience from a similar case, where an ultimate energy calibration with scandium X-rays failed [4], led to the question as to what extent chemical shifts must be taken into account for a precise energy determination. For 6 keV, a case study using of manganese fluorescence X-rays began to be applied in a precise determination of barium L$\gamma_{2,3}$ transition [5, 6].

Inspection of the literature reveals that for manganese Kα transitions the data base for compounds is rather scarce. If mentioned at all, the accuracy for the line energy is of the order of 100 meV. Also unsatisfactory is the status for an accurate quantification of the line shape, which makes it impossible to reach the ultimate level of calibration of about 10 meV.

For these reasons the measurements here aim at a precision as was achieved for the metallic state of the $3d$ transition elements [4, 7–9], which will serve as energy calibration standard for the $K\alpha$ and $K\beta$ lines measured for the compounds. A recent review on the $3d$ transition metal complexes may be found in [10, 11].

For the Kβ transition, plenty of data are available. Therefore, such data can be used as consistency check for the spectra recorded with this apparatus. It will turn out, however, that previous data are partly contradictory and this experiment is able to provide supplementary high-quality information.

Obviously, having an ultimate resolution device at hand, it makes sense to study at this occasion the complex inner-shell interactions of electrons in manganese. In particular, because effects are rather pronounced in the case of the $3d$ transition elements, as it can be seen, *e. g.* directly from the well known anomalous Z-dependence of the Kα line widths [12]. Spectroscopic studies of compounds are used in order to obtain structural information both from line shifts and line shapes by measuring valence-to-core or outer core-to-core transitions like the K$\beta_{1,3}$ complex, where the influence of ligands is clearly noticeable [10]. The K$\beta_{1,3}$ satellite transitions K', K'', or K$_{2,5}$ (see Chap. 1.3) are very sensitive to the chemical environment and, therefore, can be used for a chemical characterisation even with medium resolution devices [10, 13, 14].

Chemical effects are less pronounced for the most inner core-to-core transition Kα. However, applying ultimate resolution spectroscopy in a suitable measurement geometry should allow to extend such studies also to these transitions. For cases where energy shift or line shape point to specific compound structures, Kα lines have the advantage being by far the most intense transitions of an element's characteristic X-radiation.

In order to achieve an energy calibration at the level of $10\,\mathrm{meV}$, the exact knowledge of the line shape is an essential requirement in order to associate a particular wavelength of the measured spectrum to serve as an X-ray standard. Typically, the peak value is chosen, where the measure for the accuracy is determined by the knowledge of the experimental response. Sufficient knowledge of the resolution function given, allows a detailed parametrisation of the line shape with the spectrometer response removed, the response of an arbitrary detector can be modelled and a possible offset is under control. Such high quality of the data enables future detailed comparisons with results of theoretical calculations, which in view of the variety of effects and of the complicated structure of compounds may be left to experts in the field.

A complementary tool to access the electronic structure of atoms is photo-electron emission spectroscopy or X-ray absorption which detects electrons after atom excitation [15–18]. The creation of a hole in the $2p$ shell, *e. g.* represents the final sate of the excited atom after K X-ray emission. The results may be compared to the work presented in this thesis, which provides information about so called characteristic X-ray emission spectra, which studies the energy release in de-excitation as electromagnetic radiation stemming from a $1s$ core-vacancy transition.

1.2. Atomic structure

The shell structure of the electron orbits around the central charge Z are determined by the quantisation of the action and the Pauli exclusion principle. Quantisation manifests in a finite value for the quantity h, the Planck constant, and the Pauli principle states that two fermions cannot occupy the same quantum state.

The Bohr model first takes into account the appearance of energy shells, which is characterised by the principal quantum number n. The value of n ranges from 1 to the shell containing the outermost electron of that atom, *i.e.* $n = 1, 2, ...$ This model still ignores an angular momentum of the electron's orbit, which is also quantized and given by the azimuthal quantum number ℓ requiring an extension: the Bohr-Sommerfeld model. It describes the subshell and with that the shape of the orbital and ranges for a given n from $\ell = 0 - (n - 1)$. The length of the orbital angular momentum vector is given by the relation $\hbar\sqrt{\ell(\ell+1)}$, where $\hbar = \frac{h}{2\pi}$ is the reduced Planck constant. In chemistry and spectroscopy, $\ell = 0, 1, 2,$ and 3 are called an $s, p, d,$ and f orbital.

Each orbital angular momentum state may split in $2\ell + 1$ substates, which corresponds to the possibilities of projecting the total angular momentum to an external magnetic field direction leading to an energy splitting. These levels are characterised by the magnetic quantum number m_ℓ. The corresponding projection is $L_z = \hbar m_\ell$, where values of ℓ range from $-l$ to $+l$ in integer steps. With any angular momentum associated is an also quantised magnetic moment which originates in a classical picture from the circular current owing to the electron's orbit.

First evidence, that the electron itself possesses an intrinsic angular momentum came from the fine structure splitting of spectral lines. It turned out, that the electron spin vector has length $\hbar \cdot \sqrt{\frac{1}{2}(\frac{1}{2}+1)}$ and two projections $S_Z = \pm\frac{\hbar}{2}$ relative to an external field. These states refer to "spin up" and "spin down" states. The magnetic moment, however, is twice as large as expected from spin $\frac{1}{2}$, *i.e.* the g-factor $g = 2$, and is only explained within the relativistic treatment (Dirac theory). Angular momentum of an electron and its spin add to the total spin j leading to the two possible combinations $j = \ell \pm \frac{1}{2}$.

Each electron in any individual orbital must have different quantum numbers because of the Pauli exclusion principle, *i.e.* no electron has the same set of quantum numbers (n, ℓ, m_ℓ, m_s). Hence, the maximum occupation numbers for $s, p, d, ...$ states are 2, 6, 10, ... leading to the ordering scheme of elements well-known as periodic table.

The atomic energy levels can be determined in a good approximation based on the levels of the hydrogen-like atoms under consideration of the electron shielding of the Coulomb field of nucleus by the other electrons. Then the binding energy is given by [19]

$$E(n, l, j) = R \cdot \frac{M_A}{M_A + m}[\frac{(Z - \sigma_V)^2}{n^2} + \frac{\alpha^2(Z - \sigma_I)^4}{n^4}(\frac{n}{j + \frac{1}{2}} - \frac{3}{4})]. \tag{1.1}$$

Here, $R = R_\infty \cdot hc = mc^2\alpha^2/2 = 13.6\,\text{eV}$ is the Rydberg energy, M_A - nuclear mass, m - electron mass, Z - atomic number, j - total angular momentum quantum number, α-Sommerfeld fine-structure constant ($\alpha \approx \frac{1}{137}$), σ_V - complete shielding, and σ_I - internal shielding.

The first term, which includes the kinetic and potential energies, represents the main part of the binding energy. The smaller second (fine structure) term represents the interaction energy of magnetic moments from spin and angular momentum.

1.3. X-ray emission

Characteristic X-ray emission spectra stem from photon emission when refilling inner-shell holes produced, *e.g.* by photo effect (see Fig. 1.1). In X-ray spectroscopy, two notations are commonly used. An X-ray transition, *e.g.* Kα_1 denotes the electron transition from the $2p_{3/2}$

to the $1s$ level, which corresponds to the hole or vacancy transition in the opposite direction $1s^{-1} \to 2p_{3/2}^{-1}$.

The width in energy Γ of an X-ray line depends on the life time (τ) of the involved quantum states which is related to the transition probability P by $\tau = \frac{1}{P}$. According to Heisenberg's uncertainty relation, the life time corresponds to an energy spread Γ of the transition given by $\frac{\Gamma}{2} = \hbar \cdot P$.
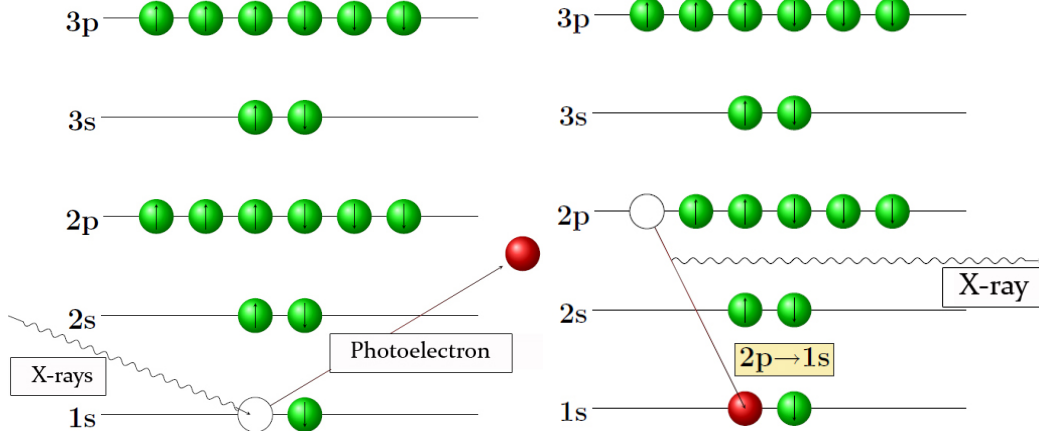

Fig. 1.1. : Schematic representation of the photoionisation and the emission of the characteristic X-rays through the electron transitions.

Radiation-less de-excitation for inner-shell holes occurs by Auger transitions (Fig. 1.2 – left). Here, the energy release when refilling an inner-shell vacancy is transferred to an electron in a higher shell, which is emitted from the atom if the binding energy is exceeded. If the Auger transition occurs within the same main shell, these processes are denoted Koster-Kronig transitions (Fig. 1.2 – right).

Radiative and Auger transitions are competitive processes which depend differently on the atomic number. As decay probabilities add up, the total width Γ of the transition is given by the sum of radiative and Auger widths $\Gamma = \Gamma_X + \Gamma_A$. In light atoms ($Z \leq 30$) Auger effect dominates also for K transitions, which is seen from a K fluorescence yield of less than 50% [20].

The natural line shape of an X-ray transition is described by a Lorentzian

$$I(E_0 - E) = \frac{\Gamma}{2\pi} \frac{1}{(E_0 - E)^2 + \Gamma^2/4},\tag{1.2}$$

where E_0 is the centre energy with the integral $\int_{-\infty}^{\infty} I(E_0 - E)dE = 1$. The width Γ corresponds to the full-width half-maximum (FWHM) of the Lorentz curve.

In the absence of external electromagnetic fields, a characteristic X-ray transition is characterised already by the two sets initial and quantum numbers (n, j) (Tab. 1.1). In an idealised atom, where an electron changes its place ignoring any coupling with other electrons or holes in the atomic shell, a single energy can be attributed to initial and final state and, hence, to the transition. Such lines are called diagram lines and are realised approximately almost exclusively for low-lying atomic levels not affected by coupling to outer shells and binding effects.

In light atoms dipole transitions dominate ($|\Delta l| = 1; |\Delta j| = 0, 1; \Delta n \neq 0$). The only (electric) quadrupole transition ($|\Delta l| = 0.2; |\Delta j| = 0, 1, 2$) appearing within this experiment is the $K\beta_5$ quadrupole transitions at the high energy side of the $K\beta_{1,3}$ doublet.
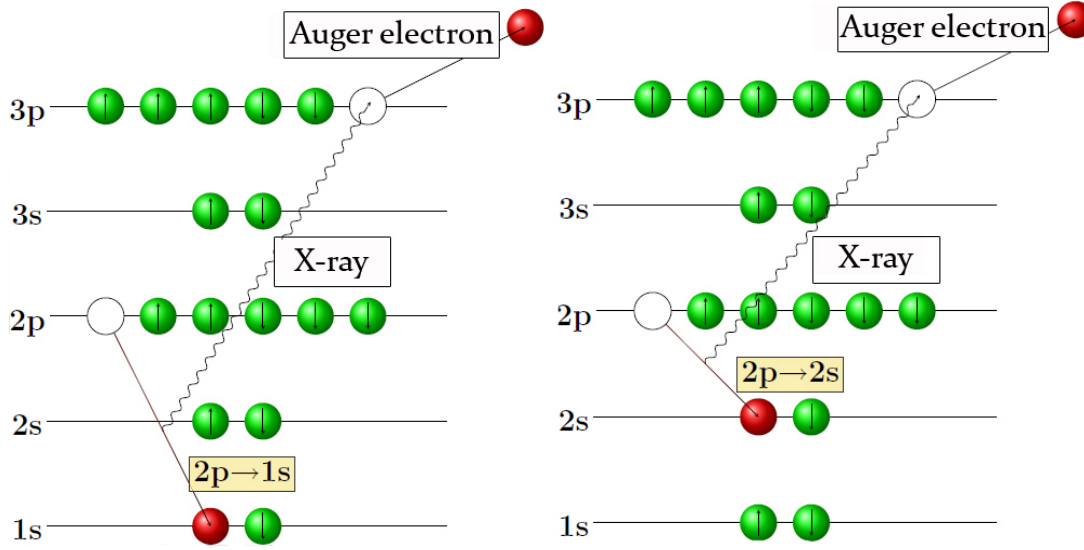
Fig. 1.2. : Schematic representation of the Auger and Coster-Kronig transitions.

Besides the described diagram lines, X-ray spectra exhibit a more complex structure. At first, the ionisation process may lead to multiple vacancies. Such additional vacancies occur predominantly in higher shells of binding energy, where the exceeding energy of excitation of deep-lying holes is used for ionisation. The corresponding change of the electron-density distribution compared to a singly ionised atoms changes the level energies.

The proper description of the atomic shells constitutes a many-body problem which is solvable only approximately. All electrons influence each other by the direct electron-electron Coulomb interaction and symmetries in quantum mechanics require to consider exchange interaction because electrons are identical particles. The coupling between core holes and outer shells leads to an additional level splitting, which however is difficult to resolve for Kα transitions in view of the comparably large natural line width Γ. In contrast, for the Kβ complex, the Kβ' line appears well separated from the K$\beta_{1,3}$ transition [10].

One example on the short wavelength side is represented by the group of Kα satellites in particular visible in the range of the $3d$ elements $Z = 21 - 30$ (α', α_3, α_3' and α_4) [21, 22]. They arise when besides an $1s$ hole one more electron is missing in L shell (Tab. 1.1). Additional vacancies in the M shell can appear on the short ($3p$ hole) and the long wavelength side ($3d$ hole). Such satellites are much closer in energy to the diagram lines.

Table 1.1. : Notation of Kα and Kβ transition energies. EI and MO denote possible contributions from the exchange interaction and molecular orbit formation [10]. For the multiple ionisation case describe the additional terms the coupling of the single angular momentum, $^{2S+1}$L with $L = \sum l$ and $S = \sum s$

Kα_1	$1s^{-1} \rightarrow 2p_{3/2}^{-1}$		Kβ_1	$1s^{-1} \rightarrow 3p_{3/2}^{-1}$
Kα_2	$1s^{-1} \rightarrow 2p_{1/2}^{-1}$		Kβ_3	$1s^{-1} \rightarrow 3p_{1/2}^{-1}$
Kα_3	$1s^{-1}2p^{-1}\,^3P \rightarrow 2p^{-2}\,^3P$		Kβ_2	$1s^{-1} \rightarrow 4p_{1/2,3/2}^{-1}$
Kα_4	$1s^{-1}2p^{-1}\,^1P \rightarrow 2p^{-2}\,^1D$		Kβ_5	$1s^{-1} \rightarrow 3d_{5/2,7/2}^{-1}$
Kα'	$1s^{-1}2p^{-1}\,^1P \rightarrow 2p^{-2}\,^1S$		Kβ'	$1s^{-1} \rightarrow 3p^{-1} + \mathrm{EI}$
Kα_3'	$1s^{-1}2s^{-1}\,^1S \rightarrow 2s^{-1}2p^{-1}\,^3P$		Kβ''	$1s^{-1} \rightarrow 3p^{-1} + \mathrm{MO}$
Kα''	$1s^{-1}3p^{-2} \rightarrow 2p^{-1}3p^{-2}$			

More complicated are satellite structures in solids and compounds. Valence orbitals of the emitting atoms overlap with orbitals of the neighbouring atoms and molecular orbitals (MO) are formed constituting the bond. As a result, so called cross transitions between the different ions can occur. Such effects are seen in the $K\beta$ regime [10]. *E. g.*, the $K\beta_5$ emission band denotes the electrical quadrupole hole transitions from $1s^{-1}$ to $3d^{-1}_{5/2,7/2}$ states which is actually mixed with p states of the ligand. For $73 \leq Z \leq 80$ this can be proven by means of the intensity ratio of the $K\beta_5$ to the $K\beta_1$ transitions. A scheme for the K fluorescence complex is shown in Fig. 1.3 [10].
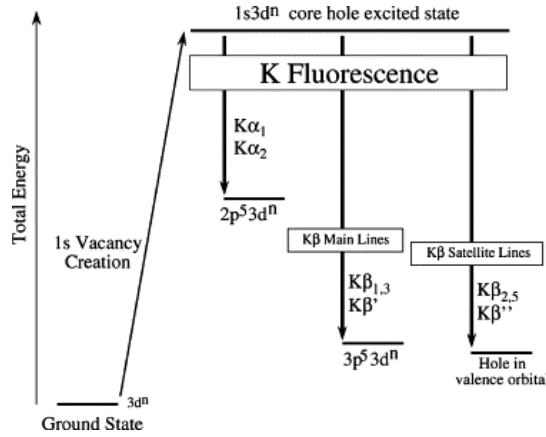

Fig. 1.3. : Simplified energy scheme for K fluorescence emission [10]. The different radiative decay channels of the 1s vacancy give rise to the K fluorescence spectrum. The continuum electron that occurs after 1s photoionization is neglected in the intermediate and final states. Atomic configurations are used for simplicity.

In summary, the complexity of the X-ray spectra and the structure of the satellite spectrum gives insight in structural and bond information of the atom's environment and the status of its outer shells, among others the spin state of an incomplete $3d$ shell. manganese.

1.4. Properties of manganese

The experiment described in this work is a study of the element manganese and some of its compounds. Manganese, having the atomic number $Z = 25$, is a metallic element of 7th subgroup of the periodic system. The nominal ground-state configuration of its atomic shells is $[1s^2 2s^2 2p^6 3s^2 3p^6 3d^5 4s^2]$. From the group of $3d$ elements it is the one with a half full $3d$ shell (see Fig. 1.4).

With the fraction of 900 ppm after iron and titanium it is the heavy metal with highest appearance on the crust of the earth. It plays a decisive role in the oxygen production by the photosynthesis of plants. The only stable isotope of manganese is ^{55}Mn. Manganese appears —depending on pressure and temperature— in four different modifications. At room temperature until 700°C the α-type modification, a cubic structure is found. Between $700 - 1070$°C the β-modification (sc) and between $1079 - 1143$°C the γ- modification (fcc) is stable. At higher temperatures a δ- modification (bcc) exists and at ≈ 1250°C the melting point is reached [23] (see Fig. 1.5). The characteristics of the different modifications, as well as magnetic properties are described in [24].

The experiment described here is performed at room temperature, *i. e.* only the α-type modification of manganese is used. Metallic lattices are of considerable complexity. So,

α-type Mn consists of 58 atoms per unit cell with four non-equivalent sites [25]. From the conductivity, one concludes a free electron density equivalent to 1.95 per atom [26]. Hence, the electron shell configuration at the atom site is practically $[1s^2 2s^2 2p^6 3s^2 3p^6 3d^5]$, *i. e.* the 2 $4s$ electrons are non-localised. The magnetic moment of the various sites of the unit cell almost compensate. The magnetic susceptibility is a factor of about 30 smaller compared to Mn(II) compounds [27].

For this metallic configuration, the Kα and Kβ X-ray energies have been measured to high accuracy [8]. These results constitute the absolute energy calibration for the crystal spectrometer (see Chap. 7). The K series fluorescence yield of manganese is about 30% (in numbers 0.308) [20], the intensity ratio Kβ/Kα was measured to be 0.140 [8].

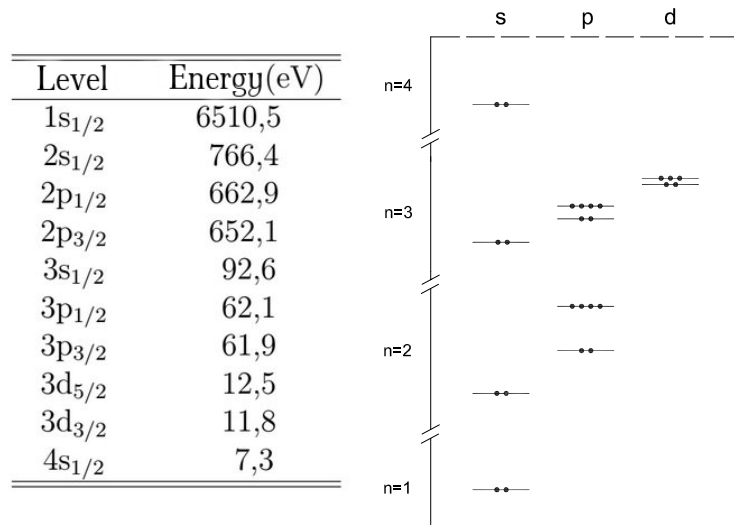| Level	Energy(eV)
$1s_{1/2}$	6510,5
$2s_{1/2}$	766,4
$2p_{1/2}$	662,9
$2p_{3/2}$	652,1
$3s_{1/2}$	92,6
$3p_{1/2}$	62,1
$3p_{3/2}$	61,9
$3d_{5/2}$	12,5
$3d_{3/2}$	11,8
$4s_{1/2}$	7,3

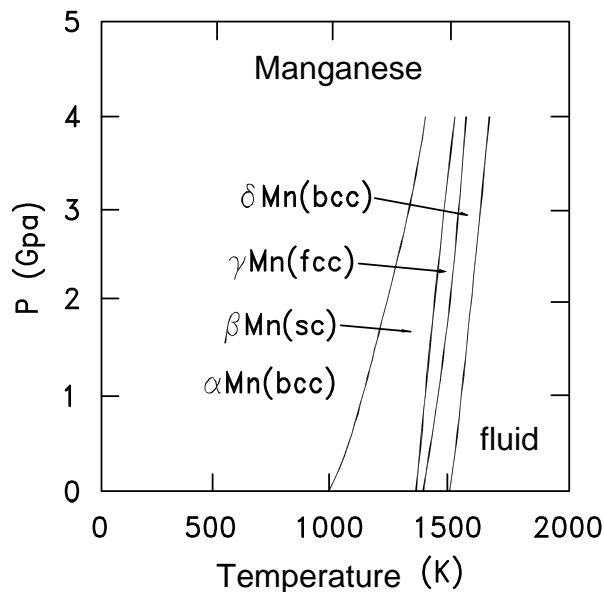**Fig. 1.4.** : Binding energies and nominal electron configuration of manganese.

Fig. 1.5. : Phase diagram of manganese.

7

1.5. Properties of manganese compounds

In compounds, nominal oxidation numbers are attributed to the constituents. It denotes the number of transferred electrons according to the stoichiometric formula of the compound, which is, however, in general only a crude approximation to the true electron distribution. Nevertheless, it provides a classification reflecting the occupation of outer shells. For manganese oxidation states from -3 to $+7$ have been observed. The most common ones are $+2, +3, +4, +6,$ and $+7$, which correspond to ionisation numbers II, III, IV, VI, and VII. In this experiment, compounds with manganese atoms in the states Mn(0), Mn(I), Mn(II), Mn(II), Mn(IV), Mn(V), and Mn(VII) have been studied (Tab. 1.2).

The ordering scheme maybe refined by using electronegativity (EN). EN is defined as a measure of the capacity of an atom to attract an electron participating in a chemical bond. Value reach from 0.7 for francium (actually disposal of the valence electron) up to 4.0 for fluorine (acceptance of an electron) in order to approach as much as possible the noble gas configuration of the valence shell. EN of manganese, carbon, and oxygen are 1.55, 2.55, and 3.44 according to the Pauling scale. Chemical bonds are between the extremes covalent for elements of similar EN where the delocalisation of valence electrons of all constituents form the bond, and ionic where the valence electrons are either completely donated or accepted. According to Pauling, the ionic character is given by $(1 - e^{-(\frac{\Delta\chi}{2})^2})$, where $\Delta\chi$ is the difference of EN. Ionic character values for manganese involved bonds are: MnO - 59%, MnF - 78%, MnC - 22%.

Formal oxidation numbers correlate with the number of electrons remaining in the $3d$ shell. For Mn(II), all 5 d electrons remain, where for Mn(VII) the $3d$ shell is completely empty. Embedded in a structure like a crystal, the complete energy degeneration (in absence of spin-orbit interaction) of the $5d$ orbitals is removed. As known from coordination chemistry, compounds of $3d$ elements with high ionic character often form the maximum spin because it is lower in energy than pairwise compensated. As a rule of thumb, high-(low-)spin states are formed when the interaction energy Δ due to the ligand field is small (large). Fig. 1.6 demonstrates the scheme of energy splitting for the octahedral crystal structure of manganese.

Thus, high-spin states up to $S = \frac{5}{2}$ are possible for Mn because only incomplete shells contribute. The electrons forming these states are denoted unpaired and their number n_{unp} can be read off from the ionisation number (Tab. 1.2). The existence of these high-spin states is proven from the measurements of the magnetic moment, which also show that angular momentum contributions from the $3d$ electrons are quenched [10, 28]. In this case, the magnetic moment μ is given exclusively by the spin part $\mu = g\sqrt{S(S+1)}\mu_B$ with μ_B being the Bohr magneton and $g = 2$ being the g-factor for fermions.

The crystal structure of the various compounds may influence the atomic levels. The compounds studied in this work are all of octahedral structure (typical for the complex chemistry of $3d$ elements), except the one of the MnO_4^- anion in $KMnO_4$ which is tetrahedral. Octahedral and tetrahedral structures have configuration numbers 6 and 4, *e. g.* 6 and 4 nearest neighbours. These two geometries have been used for an attempt to reproduce the energy shifts by means of a molecular orbital calculation (see Chap. 8). Tab. 1.2 shows the basic parameters characterising the Mn compounds used.
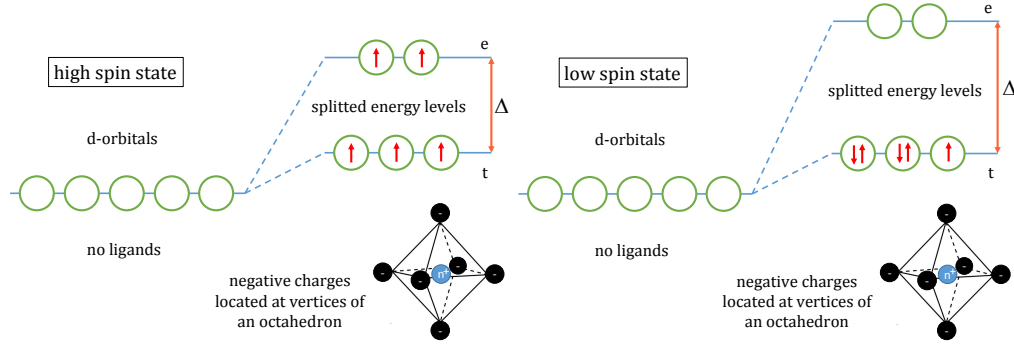
Fig. 1.6. : Energy splitting scheme for the octahedral crystal structure of manganese.

Table 1.2. : Crystallographic parameters of measured Mn compounds.

	ionisation no.	no of unpaired electrons	Crystal structure	Unit cell (a,b,c in A; α, β, γ in °)	Space group
Mn (metal)			body - centered cubic	8.912, 8.912, 8.912; 90.0, 90.0, 90.0	I 43m
Mn(0)	0	5	monoclinic	14.160, 7.110, 14.670; 37.5, 105.0, 37.5	$I2/a$
Mn(I)	I	4	monoclinic	11.990, 7.070, 10.930; 31.1 117.8 31.1	$P2_1/a$
MnF_2	II	5	tetragonal	4.873, 4.873, 3.310; 90.0, 90.0, 90.0	$p4_2/mnm$
MnO	II	5	Halite (cubic), cF8	4.536, 4.536, 4.536; 90.0, 90.0, 90.0	Fm$\bar{3}$m (225)
$Mn(CH_3COO)_2$	II	5	monoclinic/tetrahydrate	9.099, 17.600, 19.560; 42.74, 94.52, 42.74	$p4_2/mnm$
MnF_3	III	4	Monoclinic/octahedral	8.920, 5.047, 13.474; 90.0, 92.62, 90.0	$C2/c(15)$
Mn_2O_3	III	4	cubic	4.506, 4.506, 4.506; 90.0, 90.0, 90.0	$Ia\bar{3}(206)$
MnO_2	IV	3	tetragonal	4.398, 4.398, 2.877; 90.0, 90.0, 90.0	$D_{4h}^{14} - P4_2/mnm$
Mn(V) complex*	V	2	monoclinic	14.261, 8.620, 8.620; 42.906, 94.188, 42.906	$P2_1/c$
$KMnO_4$	VII	0	orthorhombic	9.09, 5.72, 7.41	$D_{2h}^{16} - Pnma$

1.6. Level splitting

1.6.1. Spin-orbit coupling

The energy splitting of the Kα lines, representing the hole transition $1s3d^n \rightarrow 2p^53d^n$, is dominated by a strong spin-orbit coupling, *i. e.* the interaction of the magnetic moment of the electron with the magnetic field created due to its orbit in the nuclear Coulomb field. In the simple case of an ion with complete shells and one inner-shell hole, the fine-structure splitting relative to the energy centre of gravity of the multiplet reads

$$E = -\frac{\xi}{2} \cdot (j+1) - \ell(\ell+1) - s(s+1)], \tag{1.3}$$

where ξ is the spin-orbit interaction parameter. As $j = \ell \pm \frac{1}{2}$ and $s = \frac{1}{2}$, the splitting for the fine-structure doublet is

$$\Delta E = \frac{\xi}{2} \cdot (2\ell + 1). \tag{1.4}$$

In the case of Mn Kα, ΔE amounts to about 11 eV [29].

The spin-orbit parameter decreases rapidly with increasing n while increasing with atomic number Z ($\xi \propto \frac{Z^4}{n^3}$). Therefore, for the K$\beta_{1,3}$ transition the spin-orbit splitting is small and not yet resolved in the case of manganese for $Z = 25$. Its contribution to the total shape of the Kβ complex is, if at all, reduced to a broadening of the K$\beta_{1,3}$ component, the structure of which is dominated by exchange interactions (see Chap. 1.6.2).

1.6.2. Core-hole $3d$-shell coupling

In the case of small contributions of the crystal field to the orbital energy, one expects high-spin states according to the number of unpaired electrons according (Hund's rule). Nominally and depending on the compound, zero to 5 $3d$ electrons are present. As mentioned before, one can assume vanishing contributions from the angular momentum of the $3d$ shell, the total spin of the $3d$ electrons ranges from $S = 0 - \frac{5}{2}$.

For incomplete shells, the interaction of the $2p$ or $3p$ core hole with the $3d$ shell must be considered. *E. g.* for an $S = \frac{5}{2}$ state, in principle on expects a splitting of the Kα_1 and Kα_2 line in 4 and 2 components, respectively, which is dominated by the $(np, 3d)$ exchange interaction. In the case the Kα, it is about one magnitude smaller than the spin-orbit contribution, but is vice versa for the Kβ case, where interacting hole and electrons are located in the shell with the same principle quantum number [10, 19, 28].

The splitting of the fine-structure components itself can be treated analogue to the spin-orbit case. For the splitting of the L_{II} and the L_{III} line caused by coupling to the total spin given by the number of unpaired electrons, n_{unp}, the approximation

$$E_{L_{II,III}} = -\frac{1}{3}a[J(J+1) - S(S+1) - j(j+1)] \qquad (1.5)$$

holds with $J = j + S$, where $j_{L_{II}} = 1/2$, $j_{L_{III}} = 3/2$, and $S = n_{unp}/2$ and a being the parameter describing the exchange interaction. If the splitting is caused exclusively by the exchange interaction $(np, 3d)$ and vanishing $3d$-shell angular momentum, the interval for the splitting is given by

$$\Delta E_{L_{II,III}} \propto J = j + S. \qquad (1.6)$$

Hence, for a splitting not resolved, *i. e.* $\Delta E_{L_{II,III}}$ is less than the natural line width, a linear increase of the total width with $3d$-shell spin is expected [19].

Such core-hole valence-shell coupling has been observed, *e. g.* in photo-electron emission from either $2s$ or $3s$ holes in MnF$_2$, which has d-shell spin $S = \frac{5}{2}$. These final states have ^7S and ^5S symmetry when hole and $3d$-shell spins couple parallel or antiparallel. The case is more complicated if a core p electron ($2p$ or $3p$) is removed, since then four final hole states ^7P and $^5P_{1,2,3}$ can be formed from the parent $3d^5$ terms of ^6S, ^4P and ^4D leading to in total 4 transitions [30, 31].

As on example for a Kβ splitting (see Tab. 1.1), the component $K\beta'$ appears in Mn(II) shifted by -17 eV from the K$\beta_{1,3}$ as a satellite on the long-wavelength side (Fig. 6.6). It represents the component with hole spin aligned antiparallel to the spin state $(^6S)\,^5P$ of the $3d$ shell, where the main part of the K$\beta_{1,3}$ consists of the aligned spin configuration $(^6S)\,^5P$. The other two weaker components $(^4P)\,^5P$ and $(^4D)\,^5P$ are predicted to be in between. The relative importance of exchange and spin-orbit contributions is discussed in detail in ref. [28].

1.7. Theoretical considerations

The theoretical calculation of the transition energies is a demanding task in view of the variety of effects. Theories have been developed describing many-body interactions both for the atomic and molecular cases like multi-configuration-Dirac-Fock [32], molecular orbital or ligand field calculations to differentiate in more detail intra-atomic Coulomb, crystal-field [33], exchange, or spin-orbit contributions [17]. Theoretical calculations including chemical and solid state effects have reached an accuracy of 0.1 eV or better [16].

It is beyond the scope of this work to provide a detailed theoretical analysis of the measured spectra. The interpretation of results is based on the extensive previous work ranging over decades and emphasis is given to the quality of data owing the good resolution of the spectrometer. Nevertheless, an attempt has been made to describe the gross feature of the energy dependence of the X-ray lines by a molecular orbit calculation, which essentially tests the variation of the electron density depending on the compound.

1.8. Outline of thesis

Kα and Kβ X-ray emission spectra have been measured by means of Bragg diffraction using a curved-crystal Johann spectrometer. The basic principles of such a set-up are described in Chap. 2. The performance of crystal spectrometers benefits from a particular type of semiconductor X-ray detector — charge-coupled devices (CCDs). Properties of CCDs are outlined in Chap. 3. Chapter 4 describes the set-up as realised at the Institut für Kernphysik at the Forschungszentrum Jülich and the measurement procedure is introduced in Chap. 5. Data processing and analysis are covered in Chap. 6. Results are introduced in Chap. 7 and the discussion of the results is given in Chap. 8. A summary of the thesis is outlined in Chap. 9.

2. HIGH RESOLUTION X-RAY SPECTROMETRY

2.1. X-ray diffraction

2.1.1. Bragg's law

It was Bragg, who offered a simple interpretation of the diffraction patterns produced by von Laue. He suggested that each of the spots surrounding the central image could be a reflection of the X-ray beam from internal planes within the crystal, that contain many regularly spaced atoms. Such planes should be parallel to the cleavage plane of a crystal and Bragg tried to reflect an X-ray beam from such a surface of a mica crystal. Using a photographic plate he recorded a spot at a specific angle of reflection.

The X-rays emerging from different planes have the same phase if the length difference between their paths is a multiple of the X-ray wavelength. This condition can be satisfied only for a particular value of the X-ray incident angle. Considering two crystal planes spaced by a distance d and X-rays with an incident angle Θ, the path difference is equal to $2d \cdot sin\,\Theta$. The condition for constructive interference between the waves scattered on the atoms of equally spaced planes is given by the Bragg law [34]:

$$n\lambda = 2d \cdot \sin\,\Theta_{\mathrm{B}}, \tag{2.1}$$

where n is the order of diffraction, λ the wavelength of the radiation, d is the spacing of the reflecting planes and Θ_{B} is then called the angle of Bragg reflection or Bragg angle (see Fig. 2.1).

Bragg's law is used in spectroscopy to transform a wavelength determination in an angle measurement. By using the relation $E = hc/\lambda$ with c being the speed of light in vacuum and h the Planck constant one obtains the photon energy.
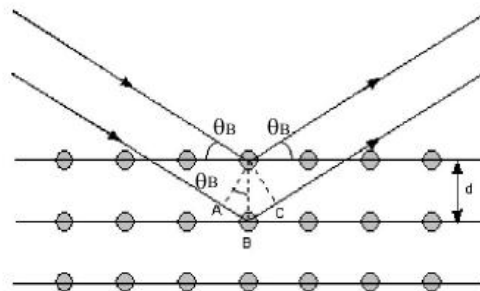

Fig. 2.1.   : Bragg reflection from crystal.

An important correction to Bragg's law stems from the index of refraction of the crystal material. For X-rays the refractive index is slightly less than 1 and so the X-ray path is

bent away from the normal inside the crystal (see Fig. 2.2). This alters the distance traveled by X-rays reflected from each "lower" plane of atoms and consequently changes the path difference for the Bragg condition to occur.
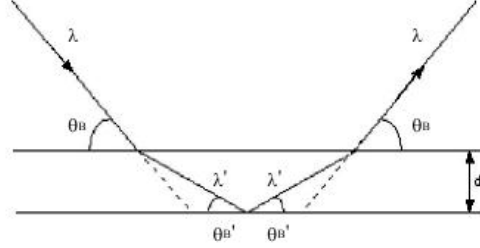

Fig. 2.2. : Bragg correction due to refraction.

The real part of the refraction index μ is parametrised as

$$\mu = 1 - \delta, \tag{2.2}$$

with δ being a small positive number which itself depends on the wavelength. Inside the crystal, the X-ray wavelength changes from λ to λ', and the angle for Bragg reflection becomes Θ'_B. Considering the refraction at the crystal surface due to Bragg's law and rewriting it inside the crystal leads to [35]

$$n\lambda' = 2d \cdot \sin \Theta'_B. \tag{2.3}$$

One obtains

$$\mu = 1 - \delta = \frac{\lambda}{\lambda'} = \frac{\cos \Theta_B}{\cos \Theta'_B}. \tag{2.4}$$

Eliminating μ and primed variables leads to

$$n\lambda = 2d \cdot \sin \Theta_B \left(1 - \frac{2 \cdot \delta - \delta^2}{\sin^2 \Theta_B} \right)^{\frac{1}{2}}. \tag{2.5}$$

Since δ is of order 10^{-5}, we can ignore δ^2, expand the bracket and, again ignoring powers of δ higher than 1 and get

$$n\lambda = 2d \cdot \sin \Theta \left(1 - \frac{4d^2}{n^2} \cdot \frac{\delta}{\lambda^2} \right), \tag{2.6}$$

which is known as the modified Bragg law [35]. The quantity δ/λ^2 is about constant.

The correction factor in brackets (2.6) varies with order of reflection becoming less significant as the order increases. Hence, the diffraction angle Θ' differs from the uncorrected Bragg angle Θ_B and can be expressed as an angular shift $\Delta\Theta_{ind}$

$$\Theta'_B = \Theta_B + \Delta\Theta_{ind}. \tag{2.7}$$

2.1.2. Rocking curve

According to Eq. (2.1), an incident photon with energy E can be reflected by the crystal only exactly at angles according to $\sin \Theta'_B(n) = n \cdot \frac{hc}{2dE}$. However, due to the diffractive nature of the scattering of electromagnetic waves from electrons, a monoenergetic incoming wave is reflected into a finite angular range around the corrected Bragg angle Θ'_B. Conversely, this means that the Bragg crystal accepts radiation within a small angular range which essentially represents the intrinsic resolution of the crystal material. The gross features of the diffracted intensity profile of a monoenergetic wave (Darwin curve) is shown on Fig. 2.3 with a flat top region known as the region of total reflection. Due to the index refraction shift the reflectivity is not peaked at zero given by Θ_B.

The angular range accepted by the crystal corresponds to the fraction of wavelength $\zeta = \frac{\Delta\lambda}{\lambda}$. It can be calculated by means of the dynamical theory of diffraction, which can be applied in case of perfect single crystals [36]. Here, the orientation of the diffracting planes is ideal and the whole wave field interferes. The X-ray beam is very weakly reflected in each crystal layer and the total reflected beam is a coherent sum over the total number of planes crossed by the incoming beam. The full width half maximum (FWHM) of the accepted wavelength range (without absorption) reads

$$\zeta_D{}^{FWHM} = C \cdot \frac{3\sqrt{2}}{\pi} \left(\frac{d}{n}\right)^2 \frac{r_0|F|}{v_c}, \tag{2.8}$$

where d is the crystal lattice spacing, v_c the volume of the unit cell being of the order of d^3 and $r_0 = 2.8179403267(27) \cdot 10^{-15}$ m is the classical electron radius. The structure factor F represents the scattering from the various atoms at their positions in the unit cell.

The polarisation factor C takes into account that the reflectivity depends on polarisation. Any direction of the electric field vector can be constructed by the components parallel and perpendicular to the reflecting plane. The two polarisations are denoted π (stands for parallel) and σ (stands for senkrecht (german for perpendicular)). For σ and π polarisation, $C = 1$ and $|cos(2\Theta_B)|$, respectively. Consequently, $C = \frac{1}{2}[1 + |cos(2\Theta_B)|]$ for an unpolarised beam.

Wavelength and corresponding energy interval are related to an angular spread by

$$-\frac{\Delta E}{E} = \frac{\Delta\lambda}{\lambda} = \frac{\Delta\Theta}{tan\,\Theta_B}, \tag{2.9}$$

as can be shown by differentiating Bragg's law. Hence, the angular width of the Darwin curve at FWHM is

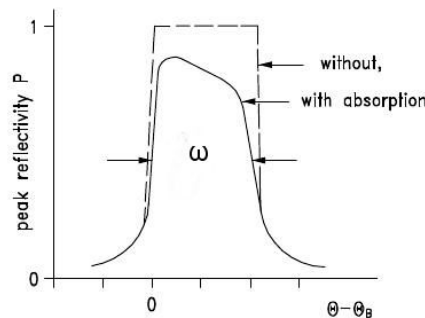$$\omega_D = \zeta_D{}^{FWHM} tan\Theta_B, \tag{2.10}$$

Fig. 2.3. : Typical rocking curve for an ideal flat crystal.

i. e. the rocking curve width describes the divergence of a parallel monoenergetic beam of radiation after Bragg reflection by the crystal. Identifying $\Delta\Theta$ in Eq. 2.9 with ω_D, one obtains the angular width of a monochromatic wave diffracted from an ideal crystal, results in the (relative) intrinsic resolution for X-ray energy or wavelength.

Along its path inside the crystal, more and more intensity of the incoming X-ray beam is diffracted into the outgoing one. A measure for the attenuation with penetration depth is the primary extinction length Λ, which is defined to be the decrease of the incoming intensity to $\frac{1}{e}$. As the reflectivity changes along the Darwin curve, the central value is taken given by [36]

$$\Lambda = \frac{1}{C} \cdot \frac{1}{4} \cdot \frac{n}{d} \frac{v_c}{r_0|F|}, \tag{2.11}$$

Λ/d is a measure of the number of planes contributing to the reflection, which would be of the order 80000 if absorption is neglected.

In addition to diffraction, electromagnetic waves are attenuated by absorption. In the energy range considered here photo effect is by far the dominating process. Hence, the total penetration depth is determined by combining extinction length and linear absorption coefficient μ, where $1/\Lambda > \mu$ is mandatory to achieve sufficient reflected intensity.

The total reflectivity, denoted integrated reflectivity R_I, is given by the integral over the rocking curve. Neglecting absorption the maximum reflectivity, the peak reflectivity $P = 1$. For the total or integrated reflectivity one obtains $R_I = \frac{4}{3} \cdot \frac{2\sqrt{2}}{3} \cdot \omega_D$ [36]. Including absorption, $P < 1$, the integrated reflectivity is in good approximation given by

$$R_I \approx \frac{4}{3} \cdot P \cdot \omega_D. \tag{2.12}$$

2.2. Curved crystal spectrometers

As described above, the Bragg condition is only fulfilled for a small angular interval ω leading to a low rate of reflected X-rays coming from a spatially extended source. Already in the early times of X-ray spectroscopy the use of bent crystals in order to improve the efficiency of Bragg spectrometers was investigated. However, the development of such a method was hindered by the conclusion of a report by E. Wagner [37], which claimed that the fulfilment of both, the Bragg condition and the ordinary law of reflection, where the emission angle is equal to the incidence angle, is impossible to accomplish. It was found by Johann, that by using a cylindrically bent crystal and an extended source it is possible to simultaneously fulfil both constraints up to a small error which can be quantified [38].

2.2.1. Johann geometry

A common set-up for reflection-type spectrometers with bent crystals uses the so called Johann geometry [38]. It incorporates an extended source, a cylindrically bent crystal and a position-sensitive detector. The bending radius of the crystal is equal to twice the radius of R_c of the so called Rowland circle. The Rowland circle, neglecting the difference of the crystal's bending radius and the one of the Rowland circle, constitutes the focusing condition for monoenergetic X-rays

$$R_c \cdot \sin \Theta_{\mathrm{B}}, \tag{2.13}$$

where the detector is placed.

The deviation of the Rowland circle to the crystal surface leads to a defocussing of the parts of the beam that are not reflected at the center of the crystal (Fig. 2.4). Owing to the symmetry of specular reflection, the trajectories of the source rays do not cross the Rowland circle in the same position. From geometrical considerations it can be seen, that X-rays not following the central ray to the crystal are always reflected towards the high energy side, *i. e.* towards smaller Bragg angles. This shift is maximal at the edges of the crystal. Assuming the total horizontal width of the crystal to be b, the so called Johann shift tangential to the Rowland circle reads in leading order [39, 40]

$$\Delta\Theta_J = \frac{1}{2}\left(\frac{b}{2R_c}\right)^2 \cot \Theta_{\mathrm{B}}. \tag{2.14}$$
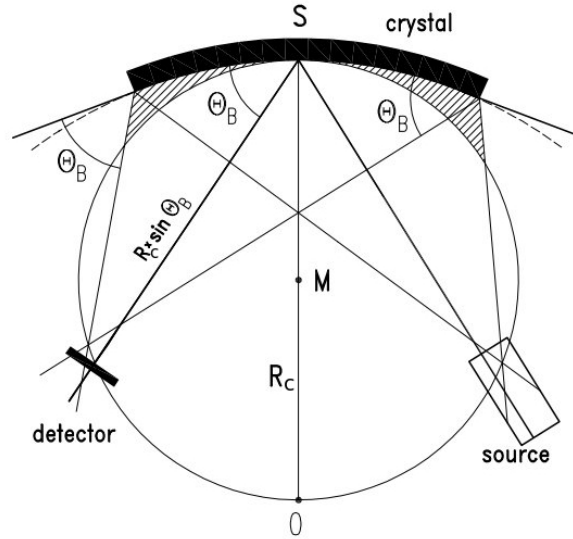

Fig. 2.4. **:** Schematic drawing of a Bragg spectrometer in Johann setup. This type of setup together with an extended source and detector allows for simultaneous measurement of a finite energy interval. Smaller wave lengths (higher energies) belong to smaller Bragg angles Θ_{B}.

The resulting Johann broadening can be tolerated if it is small compared to the intrinsic crystal resolution ω_D. Such conditions can be adjusted by choosing appropriate crystal widths b and bending radii R_c.

In principle, the Johann shift can be avoided using the Johansson set-up [41]. There, the crystal planes are again bent to a radius equal to two times the radius of the Rowland circle, but additionally the crystal surface is ground with the radius of the Rowland circle itself. In this way, the crystal surface coincides always with the Rowland circle. In practice, this is realised for compact industrial spectrometers of moderate resolution. The production of such crystals for ultimate-resolution spectroscopy, however, meets demanding technological difficulties.

Two-dimensional bending of the crystal increases the efficiency of the spectrometer, because the additional vertical focusing reduces the reflection height and, hence, enlarges the hit density on the detector [39]. Usually, spherically bent crystals are used. The crystal expansion in vertical direction leads to a curvature of the reflection in direction to lower energies.

In principle each point of the source, when fulfilling the Bragg condition, is reflected to a hyperbola-like curve in the detector plane. Therefore, the integral distribution at the detector emitted from an extended source comprises of a multitude of superimposed hyperbola (see Fig. 6.5).

Using an extended source together with a large-area position-sensitive detector allows for a simultaneous measurement of an energy interval given by the horizontal extension of the source and the detector. X-rays with different wavelengths are accepted from different places of the extended source and are focused to adjacent places on the detector. In this way the position spectrum measured in the detector plane is equivalent to an energy spectrum.

The local angular and position dispersion at the focus are given by

$$\frac{dE}{d\Theta} = -\frac{E}{\tan \Theta_{\mathrm{B}}} \tag{2.15}$$

$$\frac{dE}{dx} = \frac{E}{R_c \cdot \sin \Theta_{\mathrm{B}} \cdot \tan \Theta_{\mathrm{B}}}, \tag{2.16}$$

where the direction x is perpendicular to the axis crystal-detector centres (see Fig. 2.4).

2.2.2. Energy resolution

The energy resolution of the Johann-type crystal spectrometer depends at first on the intrinsic crystal resolution ω_D according to Eq. (2.9), and, secondly on the aberration effects due to the imaging properties. The intrinsic resolution maybe affected by the quality of the crystal material, miscut surface distortions, and the precision of the curved crystal mounting. Such effects have to be determined in dedicated measurements as described in [42, 43].

Inspecting the aberrations due to the bent geometry, it turns out that the Johann shift dominates when allowing a crystal diameter of about 100 mm and choosing bending radii of 3 m. Effects from the finite heights of the crystal (width) and source are marginal when using a two-dimensional position-sensitive detector of sufficient resolution[44]. In this way, the curvature in the detection plane can be corrected with a precision not distorting the energy information (see Chap. 6.1.3).

The gross features of the energy resolution are therefore already described by the contributions of rocking curve

$$\left(\frac{\Delta E}{E}\right)_\omega = \omega_D \cdot \cot \Theta_B \tag{2.17}$$

and the weighted average due to the Johann shift. For a rectangular shape of the aperture defining the reflecting surface of the crystal (see Chap. 4.4), the weighted average amounts to about $\frac{1}{3}$ of the maximum shift [44]. $\overline{\Delta\Theta_J}^2$ is therefore one third of the maximum Johann shift squared.

$$\left(\frac{\Delta E}{E}\right)_J = \frac{\Delta\Theta_J}{3} \cdot \cot \Theta_B = \frac{1}{6}\left(\frac{b}{2R_c}\right)^2 \cot^2 \Theta_B. \tag{2.18}$$

Hence, for the total energy resolution $\left(\frac{\Delta E}{E}\right)$ one expects the range

$$\left(\frac{\Delta E}{E}\right)_\omega^2 + \left(\frac{\Delta E}{E}\right)_J^2 \leq \left(\frac{\Delta E}{E}\right)^2 \leq \left(\frac{\Delta E}{E}\right)_\omega + \left(\frac{\Delta E}{E}\right)_J. \tag{2.19}$$

The other contributions of aberrations can be taken into account by means of a Monte Carlo ray-tracing simulation, which includes in principles all orders. Also imperfections due to crystal mounting can be modelled here (see Chap. 6.2).

The case of ideal crystals —mandatory for ultimate resolution spectroscopy— is approximately realised in the few keV range when using high-quality material of silicon or quartz and choosing large bending radii even when using curved crystal spectrometers. Typical values achieved are $\frac{\Delta E}{E} \approx 10^{-4}$ for first order reflections.

Tab. 2.1 summarises parameters characterizing the crystal effects for the X-ray measurements described here.

Table 2.1. : Parameters characterizing the crystal effects for the X-ray measurements. Crystal parameters are calculated from XOP [45]. Crystal depth is perpendicular to surface and for intensity. Conversion from μrad to seconds of arc ($''$) is 1 $\mu rad = 0.206''$.

	Mn Kα_1	Mn K$\beta_{1,3}$
Energy (eV)	5898.801	6490.585
reflection 2nd order	quartz (20–2)	
2d (nm)	0.66860 $\pm$ 0.00002	
δ	$1.608 \cdot 10^{-5}$	$1.325 \cdot 10^{-5}$
$\Delta\Theta_{ind}$	$6.77''$	$5.83''$
Θ_B	$38°\ 57'\ 24.7''$	$34°\ 50'\ 54.9''$
$\frac{dE}{d\Theta}$ (meV/$''$)	35.37	45.19
$\frac{dE}{dx}$ (eV/mm)	5.4678	3.8896
ω σ-polarization (R_I)	$3.05''$	$2.62''$
R_σ	$1.64''$	$1.45''$
ω π-polarization	$0.64''$	$0.91''$
R_π	$0.19''$	$0.38''$
Penetration depth σ-polarization (μm)	2.91	2.91
Penetration depth π-polarization (μm)	13.90	8.40
linear absorption coefficient (μm)	44.39	58.64
R_c (mm)	2981.1 $\pm$ 0.7	
$R_c \cdot sin(\Theta_B)$ (mm)	1875.68	1704.86
$\Delta\Theta_J$ ($b = 60$ mm)	$12.90''$	$14.98''$

3. CHARGE-COUPLED DEVICES

3.1. Charge-coupled devices as radiation detector

A charge-coupled device (CCD) represents a semiconductor photon detector, usually fabricated from p-type silicon, comprising an array (one or two dimensional) of elements or pixels capable of storing photon-generated charge. Typically, this charge —after being "shifted" to an output electrode— is amplified and converted into a digital value [46].

CCDs provide an intrinsic two-dimensional position resolution by their surface structure. The charge locally created is kept in place by electric potentials allowing the reconstruction of the impact coordinates. The amount of charge is a measure of the amount of light arriving at the pixel until saturation is reached. The readout process attributes coordinates to the individual pixels, $i.\,e.$ the charge pattern is then converted to an image.
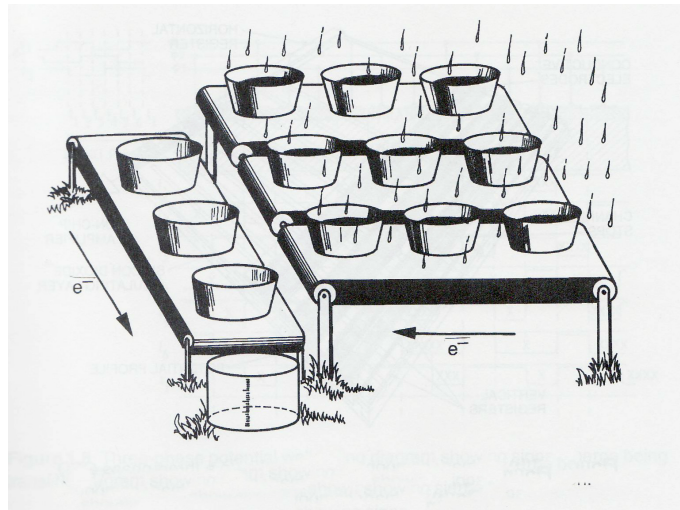

Fig. 3.1. : Bucket analogy used to describe CCD operation [46].

The principle of CCD operation can be demonstrated as a "bucket brigade"(see Fig. 3.1). Here rain drops correspond to photons and buckets to pixels. Determination of the brightness distribution in a CCD image can be linked to measuring the rainfall at different points in a field with an array of buckets. For readout, the buckets in each row are moved down vertically across the field on conveyor belts. As the buckets in each column reach the end of the conveyor, they are emptied into another bucket system on a horizontal belt, that carries it to a metering station where its contents are measured. Counting the steps of the conveyor belts creates a coordinate tuple (x, y) in the buckets plane.

When using CCD detectors for X-ray measurements, they have properties superior to other X-ray detectors:

1. Intrinsic spatial resolution for low-energy X-rays in two dimensions.

2. Good resolution of the collected charge as common for semiconductor detectors.

3. Pattern recognition allows background suppression in particular in accelerator environments [1, 3].

4. High quantum efficiency QE (QE is defined as the ratio of number of X-rays detected to number of incident X-rays and is expressed either as a value between 0 and 1 or as a percentage).

5. Good linearity (Linearity is a measure of how consistently the CCD responds to charge above its threshold).

6. In contrast to optical CCD devices, X-ray detectors are supposed to detect single photons, where photon energies are several orders of magnitude larger than for visible light.

The key feature which makes CCDs effective X-ray sensors and allows the determination of the photon energy is an enlarged depleted layer of silicon near the surface. Its thickness determines the quantum efficiency and the high energy detection limit. Optical CCD detectors have depletion depths of less than $5\,\mu$m, that's why their efficiency decreases rapidly above 2 keV. The penetration depth of 5.90 and 6.49 keV is 28.9 and 38.0 μm, respectively. Dedicated X-ray CCDs have depletion layers of $30\,\mu$m and more. Therefore, charge-coupled devices fabricated on high-resistivity substrates are becoming increasingly popular.

3.2. Architecture and design

A charge-coupled device is usually fabricated from p-type silicon. The storage elements of CCDs are essentially an array of metal-oxide-semiconductor (MOS) capacitors, comprising a conducting electrode deposited onto the silicon substrate with a thin insulating layer of silicon dioxide between. Each pixel actually contains a coupled number of MOS capacitors, commonly three (see Fig. 3.2).

The depletion region, also called depletion layer, is an insulating region within a conductive doped semiconductor material where the mobile charge carriers have been driven away by an electric field. The only elements left in the depletion region are ionized donor or acceptor impurities.

When the photoelectron moves through the silicon lattice of the detector, along its track electrons and holes are created. If the interaction occurs in the depletion layer, electrons feel the electric field and are collected in the potential well underneath the gates.

Application of a positive voltage to one of the conducting electrodes or gates creates a region depleted of holes beneath the electrode. The $n+$ silicon layer modifies the shape of the electrostatic potential profile of this depletion region, creating a "buried channel", allowing charge collection away from the surface, where the trapping sites would reduce the charge collection and transfer efficiency. The epitaxial silicon surface is passivated, first with a $0.1\,\mu$m layer of silicon dioxide and then with a similar thickness of silicon nitride. On top of the passivated layers are the three electrodes, constructed by deposing n-type polycrystalline silicon (poly-silicon) with an insulating layer of silicon dioxide between electrodes. The electrodes overlap as shown in Fig. 3.3. Nominally, they are of 1/3 pixel width providing a similar depletion capability underneath each one.

Finally, a vapour deposition of silicon dioxide (VAPOX) is applied to protect and passivate the CCD surface. When the gate potential is applied to the electrode, a typical depletion depth of $5\,\mu$m is achieved with a corresponding field-free region of $20\,\mu$m.
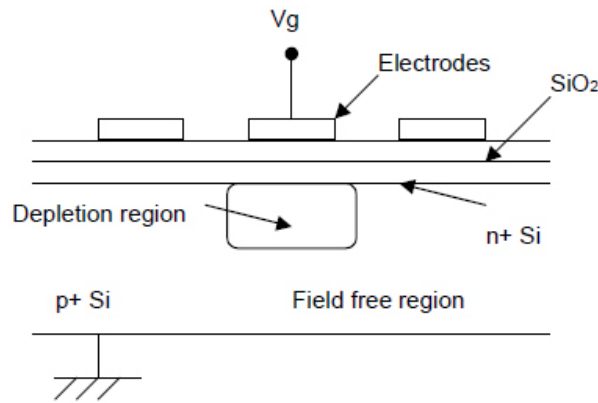
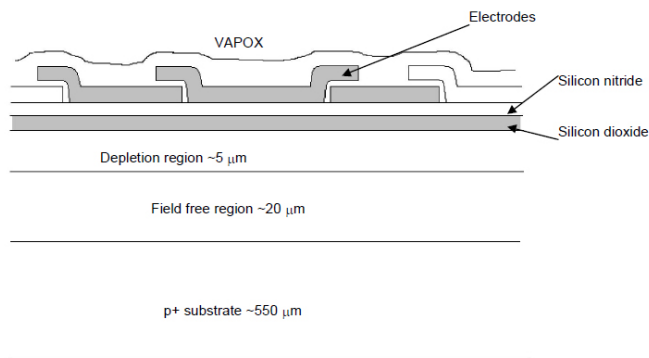**Fig. 3.2.** : CCD pixel structure [47].

Fig. 3.3. : Typical 3-phase CCD structure [47].

For an X-ray to be detected by the CCD, it must interact in the depleted silicon and this process is affected by two areas of CCD design, (a) the electrode structure and (b) the epitaxial thickness. Charge generated in the electrode structure, which essentially forms an $\approx 1.5\,\mu$m dead layer thick on the surface of the CCD, is not collected. Absorption of X-rays in this layer determines the low-energy threshold of the CCD. Charge collected in the $p+$ substrate diffuses and is lost, effectively limiting the high-energy response. Therefore, for X-ray detection in the few keV range CCD detectors with a depletion depth of about $30\,\mu$m are best suited.

3.3. Fast frame transfer CCDs

A typical device is equipped with an image and a line readout section, and its operation is divided into two phases: exposure and readout. The data are collected by exposing the image section to the X-rays. The detector operates as a camera integrating the incoming radiation for a certain exposure time. The created charge is stored in the corresponding pixels. After the exposure time, the pixels are shifted line by line to the line readout register. Each time, the readout register is processed sidewards pixel per pixel to the readout anode with subsequent amplification and digitisation.

While the lines and pixels are shifted, the pixels in the image area continue to collect photons. Thus, if the shifting is not adapted to count rate and exposure time, a "vertical smearing"

occurs. The shift frequency, however, is limited because several μs are needed to process the charge of one pixel.

The smearing is largely eliminated with so called fast frame-transfer CCDs as used in this experiment [47]. In addition to the image area, such CCDs have a store area containing as many pixels as the image area (see Fig. 3.4). After exposure time, the charge in the image region is transferred very rapidly to the storage area. From there, pixel readout via the line register proceeds at the speed necessary to correctly measure the pixels' charge content.
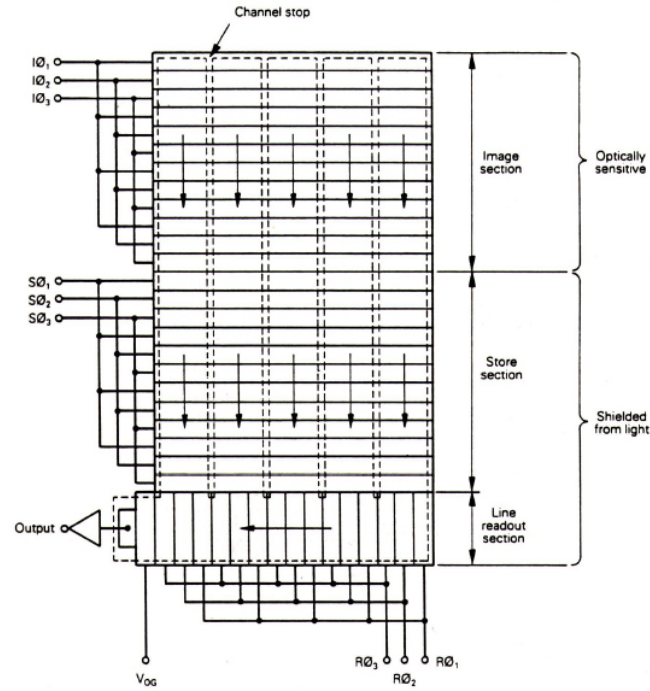

Fig. 3.4. : Scheme of three-phase CCD [47].

Hence, the CCD operation can be divided into three parts: image integration, frame transfer, and store section read out. The CCD type used in this experiment (CCD22 [48]) consists of 600 x 600 40 μm square pixels in the **image region** (Fig. 3.5). The store section has 600 x 602 pixels, but these are not square (600 $\times$ 600 μm) and allow the **store section** to be reduced in size, making a more compact CCD. The **serial register** is split with one read-out node at either end. Charge can be clocked out of either node or both nodes simultaneously, depending upon clocking operation. To maximize the high energy QE, the CCD is manufactured using 80 μm epitaxial, high-resistivity silicon (4000 Ω cm). With the gate potential applied, a depletion depth of $30 - 40\,\mu$m is achieved with a corresponding field free depth of $40 - 50\,\mu$m. The total thickness of the CCD is 350 μm.

The operation of CCDs, in contrast to many other (X-ray) detectors, requires a large number of control signals and bias voltages. These include clock signals for the various sections of the device and a number of different voltage sources for correct biasing of the detector. In addition, low noise operation is required, which in turn needs low noise electronics to drive the CCD and the application of signal processing techniques to remove inherent detector noise. Noise contributions from "dark current" are reduced to negligible levels by cooling the detector to temperatures of order of $-100°$C, which is now the standard technique for scientific CCD operation.

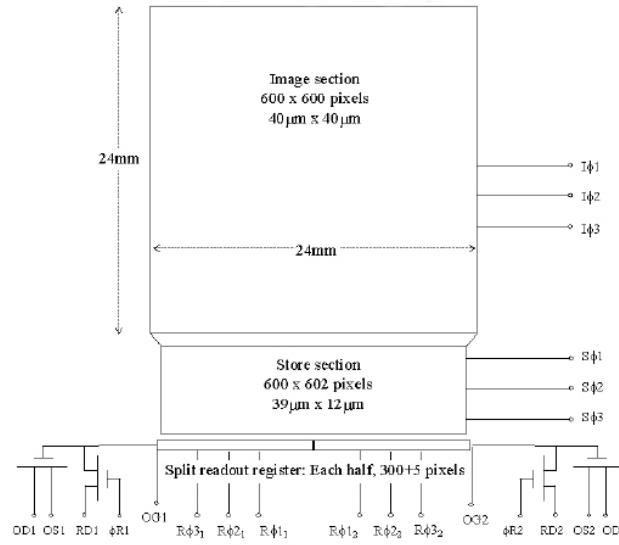A CCD as a CMOS integrated circuit comprises a large number of complementary metal-

Fig. 3.5. **:** Scheme of CCD22 [48] used in our experiments. The meaning of the signals is given in Appendix A [47, 49].

.

oxide-semiconductor (CMOS) capacitors and an output amplifier [46]. The capacitor-type structures facilitate charge storage and transfer, whilst the output amplifier provides charge-to-voltage conversion.

Electronic circuits like shown in Fig. 3.6 provide the bias voltages and a clock-sequencing device generates the clocking signals. The CCD output is amplified and passed through a signal processor. Finally, the output signal is digitized using an analog-to-digital converter (ADC) and stored on a computer. Details are given in Appendix A.
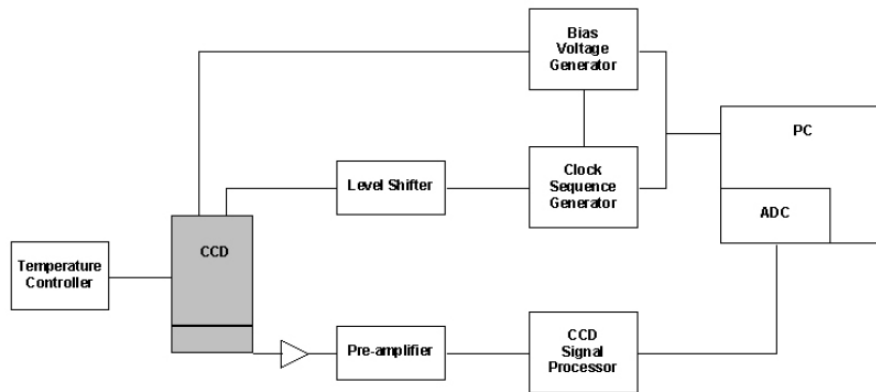

Fig. 3.6. **:** Clock and bias voltage requirements for a CCD [47].

4.   EXPERIMENTAL SET-UP

4.1. Mechanical set-up of the crystal spectrometer

The bent crystal spectrometer used is set up at the Institut für Kernphysik (IKP) at the Forschungszentrum Jülich, Germany. The principle scheme consists of three main components: an extended X-ray source (fluorescence target), a spherically bent crystal, and a position-sensitive detector (Fig. 4.1).
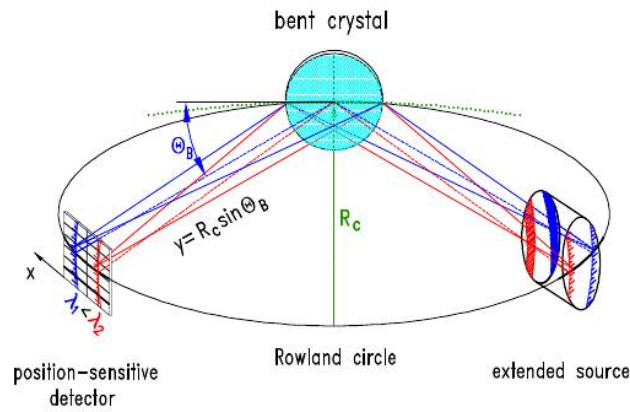

Fig. 4.1. : Schematic view of a crystal spectrometer in Johann set-up [3].

All parts are connected through the vacuum pipes in order to prevent the absorption of the few keV X-rays in air. The bent Bragg crystal and the X-ray detector are mounted on a single robust mechanical support in order to guarantee stability in long-term measurements (Fig. 4.2). Fig. 4.3 shows the set-up as realised at IKP. Details on imaging properties and applications are given in ref. [44].

4.2. X-ray tube

An X-ray tube is an electron accelerator, consisting of a high-voltage generator accelerating electrons to high kinetic energies. X-radiation is produced when the electrons hit the anode material, thus, the fluorescence X-rays are excited by means of a customary X-ray tube with high voltage and anode current adjustable from $2 - 60 \, \text{kV}$ and $3 - 60 \, \text{mA}$ (ISOVOLT 3003, Rich. Seifert & Co - Fig. 4.4). A collection of characteristic parameters is given in Tab. 4.1. The set-up panel for voltage and current is shown in Fig. 4.5.

Typical high voltages applied in this experiment were $22 - 30 \, \text{kV}$, *i.e.* excitation of X-rays in the secondary targets (see Sec. 4.3) occurs mainly through the continuous Bremsstrahlung spectrum, which has its maximum at about 10 keV. The anode current was set typically to $10 \, \text{mA}$. As exit window serves a $250 \, \mu\text{m}$ thick beryllium foil, which suppresses emission below $4 \, \text{keV}$.
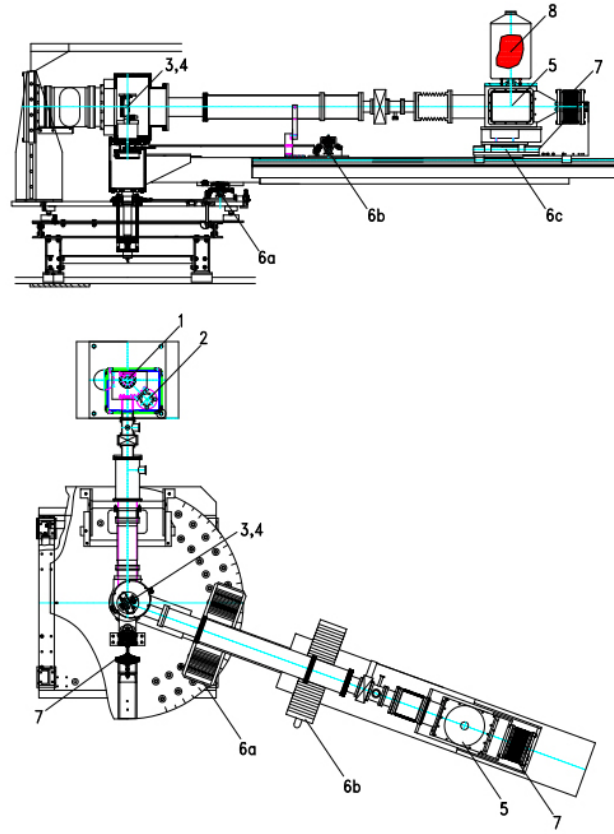
Fig. 4.2. : top - side view of the detector arm, bottom - top view. 1: position of fluorescence target, 2: X-ray tube, 3,4: Bragg crystal, support, 5: detector cryostat, 6: linear tables for a) arm, b) crystal and c) detector movements, 7: traction relaxation, 8: LN_2 -dewar. To reduce the mechanical stress between the crystal support and detecor cryostat, a compensator is installed in front of cryostat allowing small movements in vertical direction.

The direct emission spectrum of the X-ray tube as measured with a high-rate CCD [50] is shown on Fig. 4.6 - left [51]. The low and medium energy range is suppressed by a 1 mm thick aluminium filter in order to avoid an over illumination of the CCD. Also for count rate reasons, the anode current was reduced in this measurement to 3 mA.

4.3. Target chamber and fluorescence targets

The X-ray tube was attached to a vacuum chamber equipped with a $50\,\mu$m thick Kapton entrance window (Fig. 4.4). The chamber houses the fluorescence targets, where its inner walls are covered by a 3 mm thick layer of pure aluminium to suppress the excitation of contamination fluorescence X-rays. The chamber is equipped at its top central flange with a vacuum-tight feedthrough. It allows to rotate a stainless steel rod, which carries the support for the various fluorescence targets (Fig. 4.8), around a vertical axis. The support rod also was covered by pure aluminium. In this way, a practically background free X-ray emission of the selected material was achieved. As an example, the secondary emission spectrum of MnO_2 is shown (Fig. 4.6 - right). The target chamber is connected to the spectrometer volume. This part is evacuated to about 10^{-6} mbar.

Typically, target materials were spread over an area of about $(30 - 60)\,\mathrm{mm} \times 30\,\mathrm{mm}$ (horizontally $\times$ vertically) and glued to pure aluminium plates by a two component adhesive
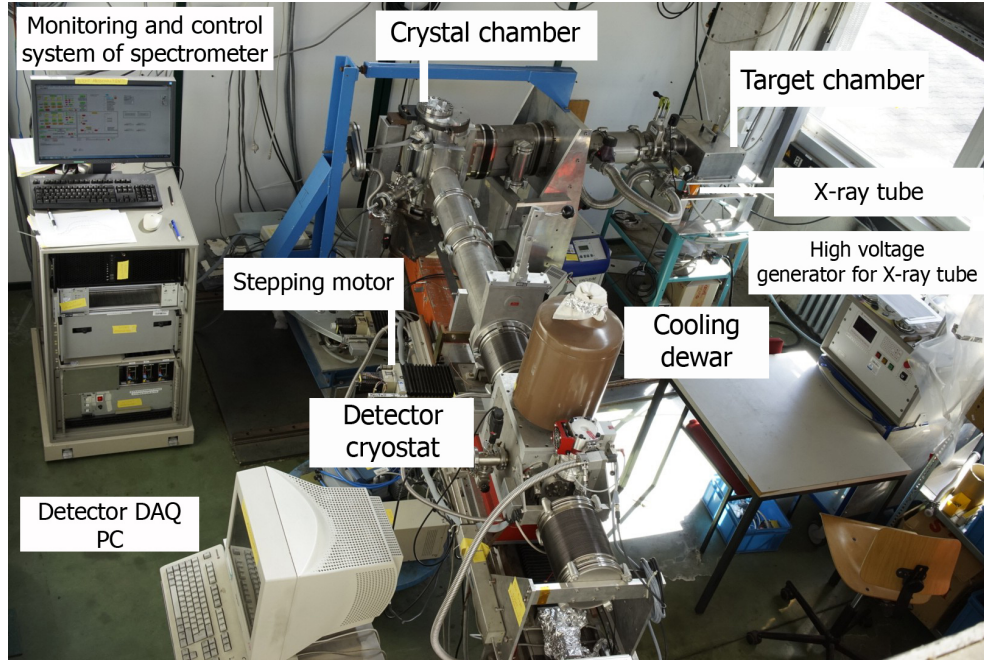
Fig. 4.3. : Set-up of the crystal spectrometer at the Institute of Nuclear Physics 2 (IKP 2) of the research centre Jülich (FZJ)

Table 4.1. : Table of parameters being controlled and monitored.

High voltage generator	Isovolt 3003
X-ray tube	DX-$\mu_0$12x0.4-S
Anode material	molybdenum
Tube voltage	2-60 kV
Filament current	3-60 mA
Be window	0.25 mm
Cooling water requirement	4.5 liters per minute
Cooling water intake temperature	Maximum 35°C
Cooling water pressure	Maximum 7 bar
Power consumption	3.5 kW

(Fig. 4.7). The support for one compound was always mounted together with the one for Mn metal back-to-back at the vacuum feedthrough rod. The thickness of the Al plates is sufficient to absorb any contribution from the back side. By rotating the support bar by 180° (Fig. 4.8), measurement and calibration target can be alternated without breaking the vacuum thus avoiding any tensions in the mechanical set-up or the need to touch the angular setting of the spectrometer.

The emission axis of the X-ray tube had an angle of $-45°$ to the axis target centre to crystal centre. The target materials were illuminated from the front side with the target plate rotated by 22.5° (accuracy $\pm1°$) towards the tube's emission axis which results in an almost uniform illumination. The emitted intensity was measured by a scan using the crystal spectrometer (see Chap. 5.1.5).

The distance of the fluorescence targets to the Bragg crystal was fixed to 1.65 m, which is a position about 20% inside the Rowland circle. In this way, inhomogeneities of the target surface are average out. The horizontal target extensions were large enough not to cut into
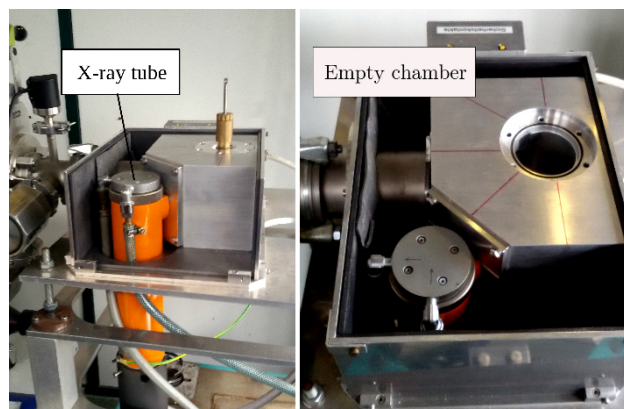
Fig. 4.4. : Mounting of the housing of the X-ray tube at the target chamber. The front and top cover of the shielding consisting of Al/Pb (5 mm/5 mm) sandwich is removed. The X-ray tube is equipped with Molybdenum anode.
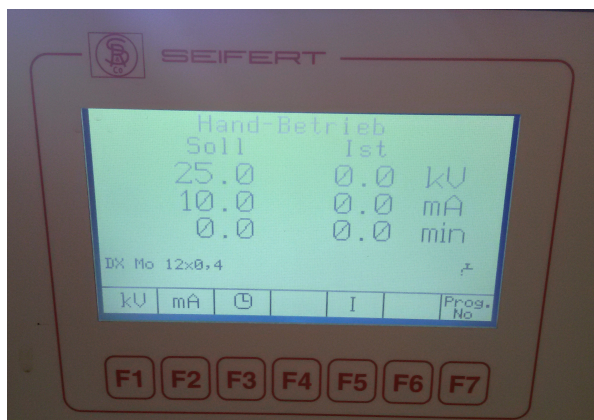

Fig. 4.5. : Setup panel for voltage and current parameters of the high-voltage generator.
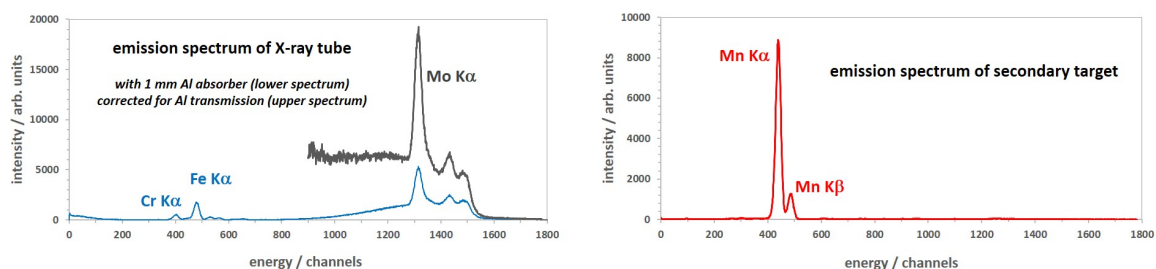

Fig. 4.6. : Left – emission spectrum of the X-ray tube for 25 keV high voltage and an anode current of 3 mA. The intensity has been measured to depend linearly from the anode current of the tube. A 1 mm thick aluminium plate is used to limit the rate in the detector. In the high-energy part, the characteristic K radiation of molybdenum (17.5 keV) is seen. The upper curve represents the emission spectrum after correction for the Al filter. Fluorescence X-rays below 7 keV originate from the steel tube walls behind the Al absorber close to the detector. Right – almost background free emission spectrum of the secondary fluorescence target bearing the manganese metal or compound.

the angular acceptance of the crystal. There is no need to change the distance to the target or the orientation towards the crystal between Kα and Kβ measurements.

The metallic manganese of 99% purity was used in a form of fragmented pieces. Exposed to air metal is covered by a few tens of nanometer thick oxide layer. Other compounds were used in a form of a powder. Purity information of the measured Mn compounds can be found
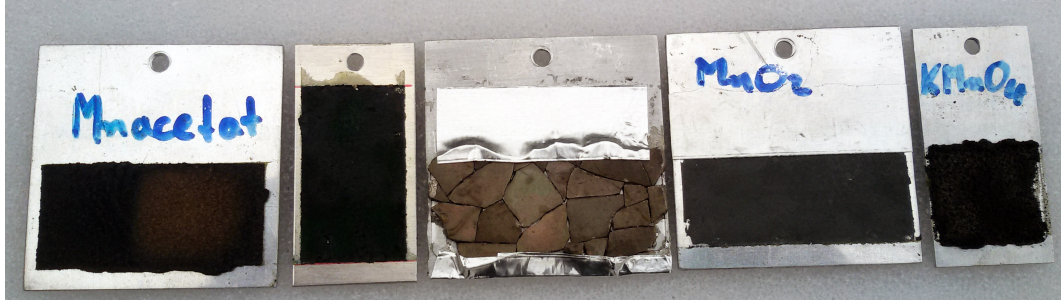
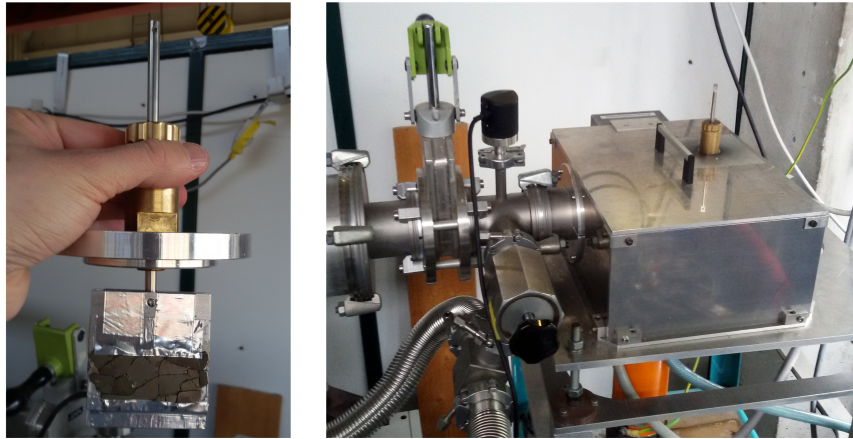**Fig. 4.7.** : Examples of measured fluorescence targets.

Fig. 4.8. : Left - fluorescence target mounted on a metallic rod belonging to the vacuum feedthrough. Right - vacuum chamber for the fluorescence targets. The orange cylinder (bottom left) houses the X-ray tube. By rotating the metallic rod carrying simultaneously two back-to-back mounted targets, measurement and calibration are possible without breaking the vacuum.

in Tab. 4.2.

4.4. Bragg crystal

A spherically bent quartz crystal is used of 100 mm in diameter and cut along the (10-1) plane. A 0.19 mm thick quartz plate is attached by molecular forces to a glass disk, which was polished on one side to a spherical surface of optical quality. The curvature of the spherical side determines the crystal's bending radius and was measured to (2981.1 ± 0.7) mm. The cutting, polishing and bending processes were performed by Carl Zeiss inc., Oberkochen, Germany [52]. The miscut angle was found in a dedicated measurement to be with $(0.11 \pm 0.11)°$ negligibly small [43].

The glass disk, having a diameter of 120 mm and thickness of 30 mm is mounted in an adjustable support frame (Fig. 4.9). In this frame, the crystal can be rotated remotely around a horizontal axis allowing the vertical adjustment of the reflection. The reflecting area of 10 cm in diameter is restricted by a circular aperture to 95 mm in diameter to avoid edge effects. For the small Bragg angles, as applied in these measurements (see Tab. 2.1), in addition a limitation to ± 30 mm horizontally is applied to reduce the Johann broadening (see Chap. 2.2).

Table 4.2. : Purity information of the measured Mn compounds.

Metallic Mn	99.5%
MnF_2	99.5%
MnO	99%
$Mn(CH_3COO)_2$	99.5%
MnF_3	99.5%
Mn_2O_3	99.9%
MnO_2	95%
Mn(V) complex ($C_{20}H_{22}MnN_3O_2$) [53]	99.3%
$KMnO_4$	99.5%
Mn(0) $Mn_2(CO)_{10}$ [54]	99%
Mn(+I) $C_5H_5Mn(CO)_3$ [55]	99%

Fig. 4.9. : Crystal support with crystal and aluminum aperture of 60 mm width. On the bottom left side the servomotor with linear potentiometer for tilting of the mirror is shown.

4.5. X-ray detector

In this experiment, a frame transfer device of type CCD22 was used, which is optimised to high quantum efficiency (QE) by an open-electrode structure design for X-ray detection in the $1-10$ keV range for astronomy missions (see Chap. 3.3) [48]. QE is increasing from $\approx$ 75% at 2 keV to a maximum of 90% around 4 keV and then decreasing according to the linear absorption coefficient of silicon. Its pixel structure is described in Chap. 3.2. Fig. 4.10 shows the detector assembly consisting of two CCD22 devices.

The CCD devices are mounted on a cooling finger connected to a liquid nitrogen (LN_2) dewar. Fig. 4.11 shows a cross section of the cryostat housing the detector arrangement. A closed-loop temperature control maintains the CCD temperature at $(-100 \pm 0.5)°$C to reduce thermally generated dark current to negligible levels. At room temperature, the pixel size is 40 μm to a precision of about 0.5 nm. As the detector material size undergoes thermal expansion, the pixel size had to be determined with high precision in a dedicated experiment. The pixel at the operating temperature $-100°$C was found to be (39.9775 ± 0.0006) μm [56].

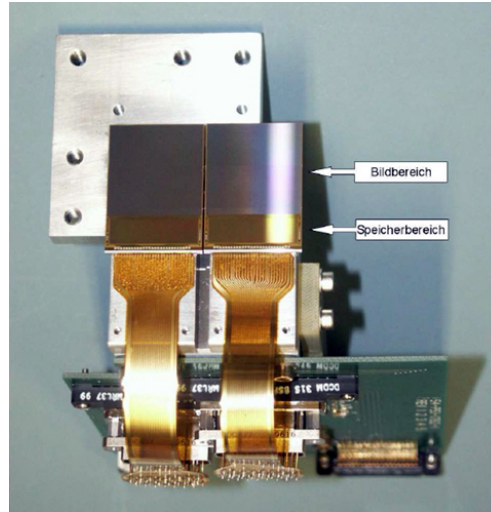The voltages are provided from a bias voltage and a clock sequencer located outside

Fig. 4.10. **:** Picture of the Detector system prior installation insode vacuum cryostat.
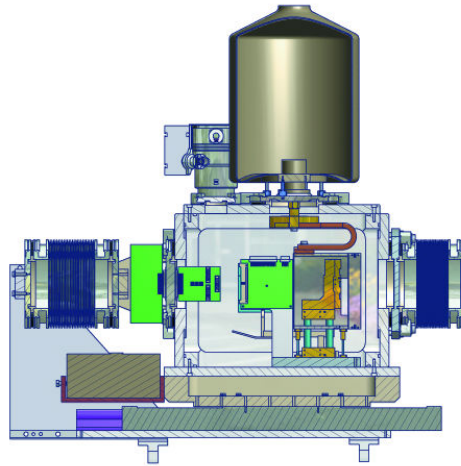

Fig. 4.11. **:** Cross section view of the detector vacuum cryostat.

the cryostat (Fig. 3.6). Details on the CCD readout and the final set of optimised CCD operating voltages is provided in Appendix A. The CCD devices are connected directly to the preamplifier boards inside the cryostat containing also distribution boards for the timing signals and bias voltages. In addition, the temperature information of CCD and cooling finger measured by means of PT100 devices are generated inside the cryostat. All signals are transferred via the 50 pin vacuum connector. The vacuum in the detector cryostat is approximately $2 \cdot 10^{-7}$ mbar and is separated from the spectrometer vacuum.

4.6. Spectrometer operation and monitoring

Key point in setting up for an experiment is to meet the geometrical conditions for the Bragg reflection together with a proper adjustment of the crystal with respect to the fluorescence target and the X-ray detector. The basic movements involved in the set-up as shown in Fig. 4.2 are sketched in Fig. 4.12.

Operations related to the spectrometer maybe divided in the two categories control and monitoring: first motion/action type operations and second readout/status check which are
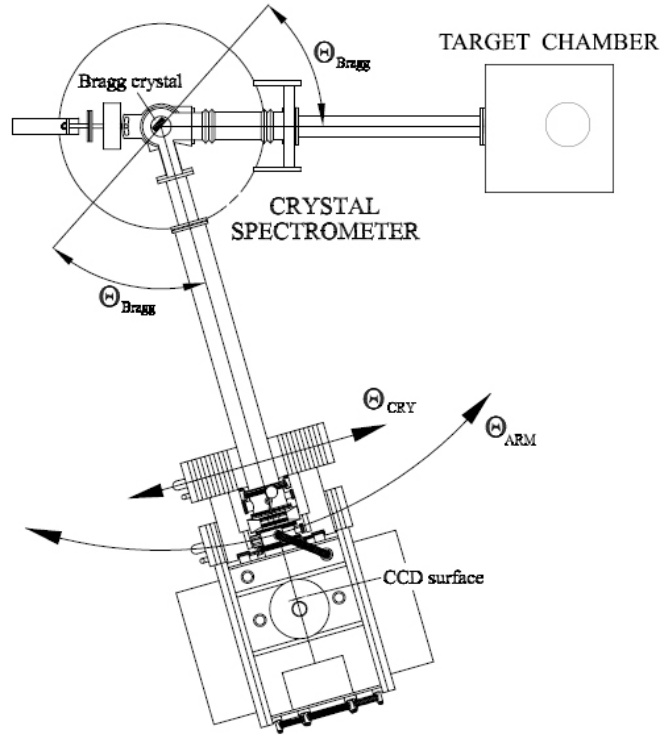
Fig. 4.12. **:** Parameters of the crystal spectometer which are controlled by Labview$^©$-based monitoring and control system. Bragg condition Θ_{Bragg} are set up by adjusting the angles Θ_{CRY} and Θ_{ARM} by means of linear tables (see text).

recorded during operation. The parameters are summarised in Tab. 4.3.

The Bragg condition is fulfilled, when the directions target-crystal and crystal-detector enclose the angle $180° - 2\Theta_{\mathrm{B}}$, which is realised by adjusting the arm bearing crystal and detector relative to the fixed axis target-to-crystal by means of the angle parameter Θ_{ARM}. In order to fulfil the Bragg condition at the crystal, the angle between the reflecting surface and the directions towards X-ray source and X-ray detector both have to meet Θ_{B}, which is set up by means of the angle parameter Θ_{CRY}. The angular movements are done remotely using the stepper motors driving linear precision tables. The angles are measured independently by high-precision angular encoders.

The focal condition $\mathrm{Y}_{\mathrm{CD}} = R_c \sin \Theta_{\mathrm{B}}$ is adjusted by another linear table carrying the detector and is measured by a linear potentiometer. Finally, for positioning the reflection vertically, the the crystal holder allows a rotation around the horizontal crystal axes (tilt angle). Again, these operations are performed remotely and under vacuum conditions. The set-up procedure for the experiment is described in detail in Chap. 5.

The remote control and monitoring is based on a Labview$^©$ and FieldPoint$^©$ Supervisory Control and Data Acquisition [57] (SCADA) systems and was developed at Forschungszentrum Jülich and dedicated specifically for this experiment (for an elaborate overview see Appendix C).

Table 4.3. : Spectrometer parameters.

function	parameter	device	precision
MONITOR			
angular setting			
Bragg angle	Θ_{CRY}	angular encoder	0.2"
arm angle	Θ_{ARM}	angular encoder	≈ 3"
distance crystal-detector	Y_{CD}	linear potentiometer	$0.2\,mm$*
crystal tilt		linear potentiometer	$0.1°$
temperatures			
crystal	crystal support	PT100	$\pm 2°C$
	crystal chamber	PT100	$\pm 2°C$
detector	CCD22	PT100	$\pm 2°C$
	cooling finger	PT100	$\pm 2°C$
vacuum			
spectrometer low	pre vacuum	Leybold TR211	$10^{-3}\,mbar$
	high vacuum	Leybold PR 25	$10^{-7}\,mbar$
detector	pre vacuum	Leybold TR211	$10^{-3}\,mbar$
	high vacuum	Leybold PR 25	$10^{-7}\,mbar$
SETTING			
Bragg angle	Θ_{CRY}	stepper motor	$10\,\mu m$
		PIEZO feedback	0.2"
arm angle	Θ_{ARM}	stepper motor	$10\,\mu m$
distance crystal-detector	Y_{CD}	stepper motor	$0.1\,mm$*
crystal tilt		DC motor	$0.1°$
CCD temperature		feedback loop	$\pm 1°C$

* The error in the focal length exceeds the precision of the linear table, because additional
uncertainties of the parts connecting crystal and detector contribute.

5. MEASUREMENT SET-UP AND PROCEDURE

5.1. Preparation of measurement

5.1.1. Pre-adjustment of geometry

With respect to the crystal, both target and detector angular width are of the order of $1°$. Hence, a manual pre-adjustment is sufficiently precise to meet the initial geometrical conditions for later optimisation.

At first, the arm bearing crystal and detector is set manually to an angle corresponding to the actual Bragg condition, *i. e.* to $180^0 - 2\Theta_B$ (see Chap. 4.6). This is achieved by means of the marks at the arm support table (Fig. 4.2 - bottom) with an accuracy of about 0.1-$0.2°$.

The crystal orientation towards the detector is found when a laser beam emitted from the position of the fluorescence target and reflected from the crystal centre meets the detector window centre in front of the CCD. In case of diffracting planes parallel to the crystal's surface the Bragg reflection condition is then already established. Subsequently, pumping of the spectrometer vacuum to about 10^{-6} mbar is started.

5.1.2. Detector calibration and start-up

For operation and readout of the CCD devices is used the software package xcCCD [58], which can be configured for the CCD22 frame transfer type. The basic parameters set up within the xcCCD program are the clocks, bias voltages, sequencer timing and the gain level. Figs 5.1 and 5.2 show corresponding set-up windows. The parameters of the sequencer and the voltage settings can be stored in and uploaded from parameter files. Readout direction of the line register (see Chap. 3.3) can chosen either forward or backward in case of node damages. For normal operation both the horizontal and the vertical directions are clocked forward.

Two kinds of voltages are to be set: clock voltages responsible for charge transfer and the bias voltages supporting the detector itself (see Fig. 5.2). These voltage values are fixed after optimisation for minimum noise level and maximum charge collection determining the energy resolution of the CCD.

All pixels of a CCD contain charge due to noise contributions of dark current and also the electronics chain contributes even without the charge created by a signal stemming from X-ray conversion. In order to minimise the amount of stored CCD data only thresholded data are stored. Therefore, at first a calibration procedure is performed which determines the noise level (noise peak) and its distribution (characterized by the noise peak width). The absolute noise level represents the average charge offset of all pixels in the readout chain. After subtraction of the offset, the origin of the charge spectrum for true X-ray events is obtained.

Fig. 5.1. : Setup of the basic operational parameters of the CCD detector.

For energy calibration of the charge spectrum, X-rays of known energy are recorded, *e. g.* from an ^{55}Fe radioactive source emitting manganese X-rays or the manganese target irradiated by means of the X-ray tube. From this calibration the noise level width is determined (in eV) and a threshold for data recording is chosen. Typical values for the offset and the noise level ($1\,\sigma$) are 1.2 keV and 80 eV, respectively. In this experiment, a threshold value of $5\,\sigma$, *i. e.* 400 eV, was chosen.

The absolute noise level depends on the device set-up itself and possible contributions from the environment and may vary during long-term measurements. Therefore, the calibration procedure was performed at regular intervals (usually once per week) to ensure that the system was operating as expected.

The calibration procedure is performed by using the XCAM [59] spectrum analyser tool (Fig. 5.3). Noise peak and X-ray peak are determined by placing the mouse pointer and clicking first on the low- and then on the high-energy side. Noise calibration is also the same, but it is usual to place cuts at a height of approximately 10% that of the peak height. The calibration algorithm calculates the energy per channel and the FWHM of the X-ray peak and the noise in electron rms (1 e$^-$ rms = 3.65 eV).

As a result of the calibration, when using thresholded data, per frame about 1900 of the 360.000 pixels of CCD22 are stored for further analysis. For data taking, in the XcCCD interface the number of frames to be collected per data file is selected. The data are stored on the PC controlling the CCD operation (see Chap. 3.3).

The data files are organised as preceding header containing the CCD set-up and calibration parameters as well as operator added information followed one block per recorded frame containing the pixel data. Pixel data are encoded binary by using 5 bytes. Two bytes contain the data provided by the 12-bit ADC (thresholded charge content) and the others the address information of the pixel (Fig. 5.4).

The XcCCD interface supplies during the measurement information of the number of pixels recorded per frame. For usual measuring conditions, this number should be around 2000-4000. Increasing values indicate a possible incorrect CCD operation, *e. g.* by additional noise contributions from external sources or warming up of the detector.
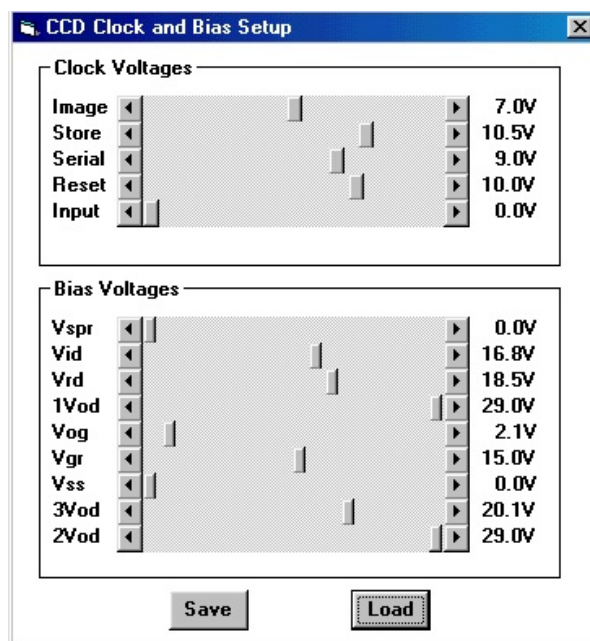
Fig. 5.2. : Setup of the detector support voltages.

5.1.3. X-ray tube

The hit pattern from an individual frame and the corresponding energy spectrum can be directly displayed on the screen of the PC serving the data readout from the detector (Fig. 5.5).

As the CCD integrates the incoming photon flux, for proper single photon detection an over illumination has to be avoided. Therefore, the maximum density of hits in the reflection region must be kept at maximum at the few per cent level. The degree of illumination was adjusted by the anode current of the X-ray tube individually for the various targets.

5.1.4. Crystal scan (positioning reflection on the detector)

Usually, it is of advantage to choose for the diffracted X-rays the centre of the X-ray detector to ensure that the tails of the pattern are fully covered. The exact positioning is achieved by rotating the crystal around its vertical axis (angle Θ_{CRY}, see Chap. 4.6). In case the Bragg reflection condition lies outside the fluorescence target, a readjustment of the arm angle Θ_{ARM} may become necessary (see Chap. 5.1.5).

5.1.5. Target scan

This procedure measures the intensity of radiation emitted by the fluorescence target along the direction of the dispersion to select the region of maximum intensity of emitted X-rays. This is achieved by rotating only the arm (changing the arm angle Θ_{ARM}) of the spectrometer. Moving only the arm does not affect the alignment between Bragg crystal and detector. Typically, the X-ray intensity was measured in steps of $5'$ of the angle Θ_{ARM}. The spectrometer was set to an arm angle which covers the maximal intensity both of the $K\alpha_1$ and the $K\alpha_2$ emission (see Fig. 5.6) or the maximum of the $K\beta$ intensity.
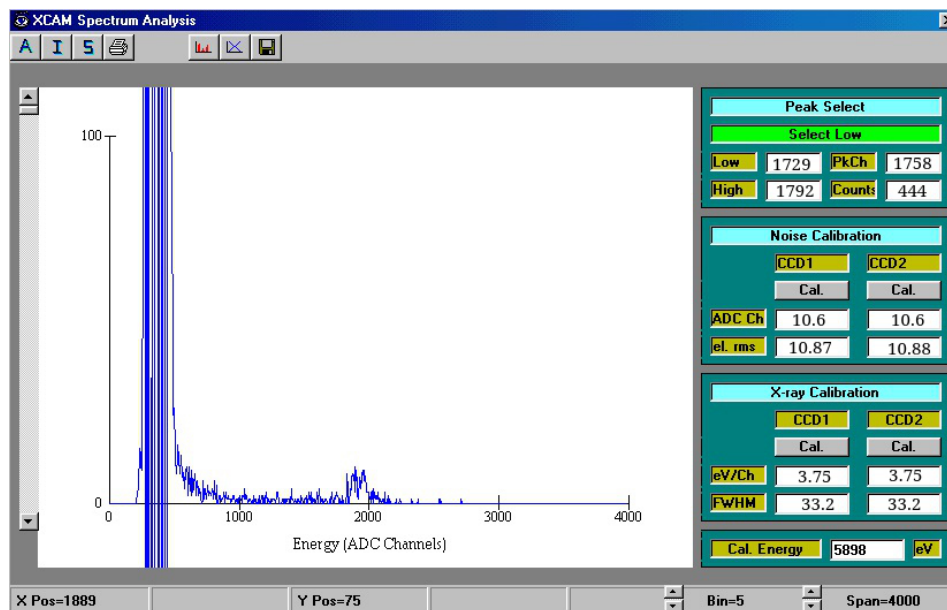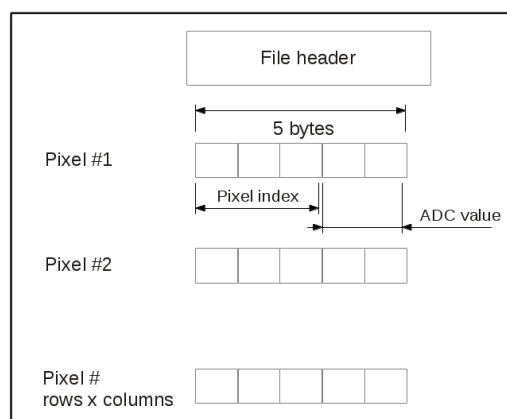
Fig. 5.3. : Detector calibration.

Fig. 5.4. : Structure of raw data file.

5.1.6. Crystal tilt scan

Vertical positioning of the reflection is achieved by rotating the crystal around its horizontal axis and searching for maximum overlap of reflection and detector. The intensity distribution from a scan over the tilt range of the crystal is shown in Fig. 5.7.

5.2. Measurement procedure

5.2.1. Alternating targets

Each experiment consists of two series of measurements: one for metallic manganese providing the energy calibration and another one for manganese compound.

The two fluorescence targets are back-to-back mounted on the support bar which is housed in the flange of the target chamber (see Figs. 5.8 and 5.9). Because both targets have similar geometry and as the energies of metal and compound differ by less than 2 eV, the reflection
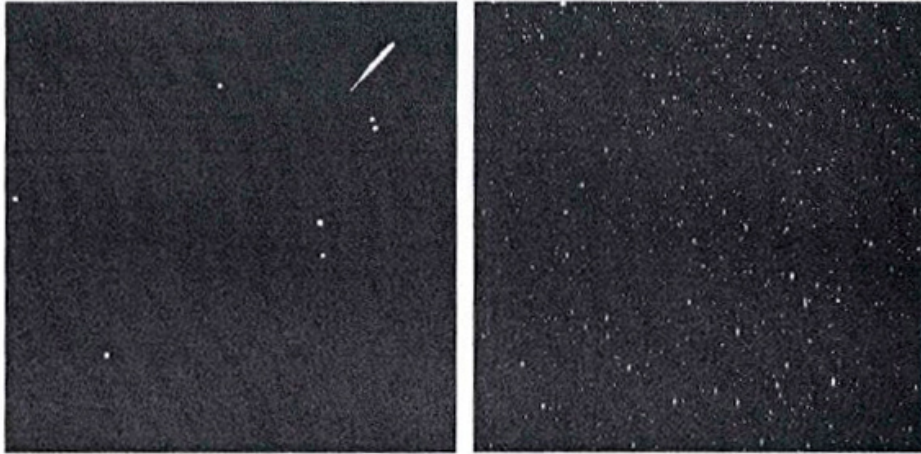
Fig. 5.5. : CCD22 detector hit pattern, demonstrating the pixels hitted by X-rays [47]. Left - track of cosmic ray. Right - events from a radioactive source.
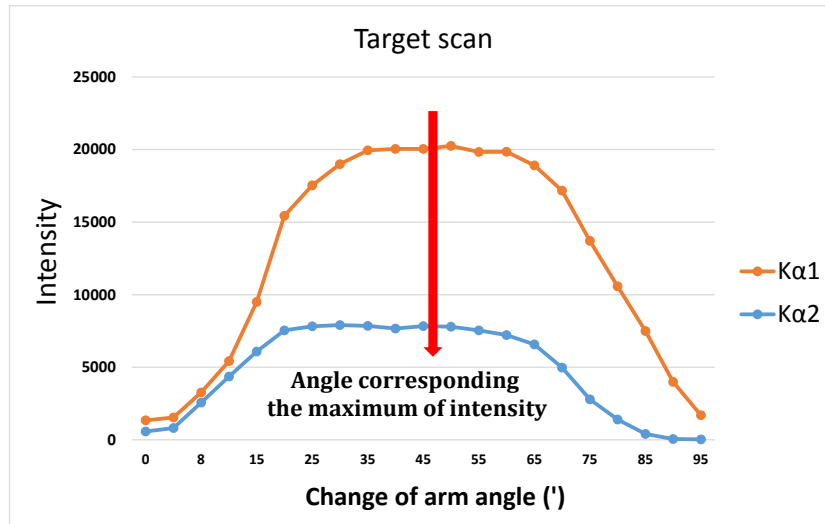

Fig. 5.6. : Result of the target scan demonstrating the maximum of X-ray emission intensity.

and focusing conditions of their fluorescence X-rays are identical. By rotating the feedthrough support bar by 180°, measurements could be performed without breaking the vacuum or touching the angular set-up of the spectrometer.

5.2.2. Measuring sequence and duration

During the measurement, metal and compound are interchanged several times. Usually per one alternation of target 300 frames of X-ray data are recorded. One frame refers to one complete readout of the CCD. Recording 300 frames takes approximately one hour. At the end of the experiment about equal statistics is needed for the metal and the compound spectra.

Usually emitted intensities are lower for the compound than for metal. Therefore, more frames are required to be recorded for compounds. In our case, in total approximately 300×25 frames of X-ray data were recorded per metallic manganese, which corresponds to 25 hours
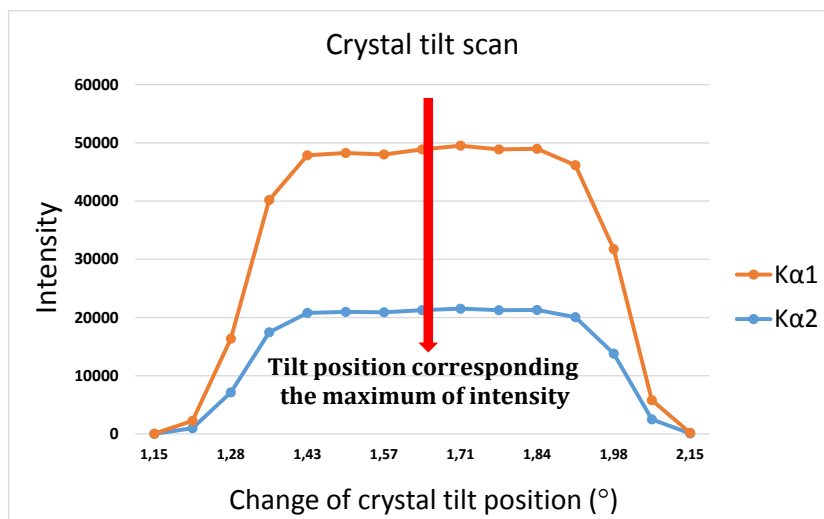
Fig. 5.7. : Result of the crystal tilt scan demonstrating the vertical adjustment of the reflected intensity.
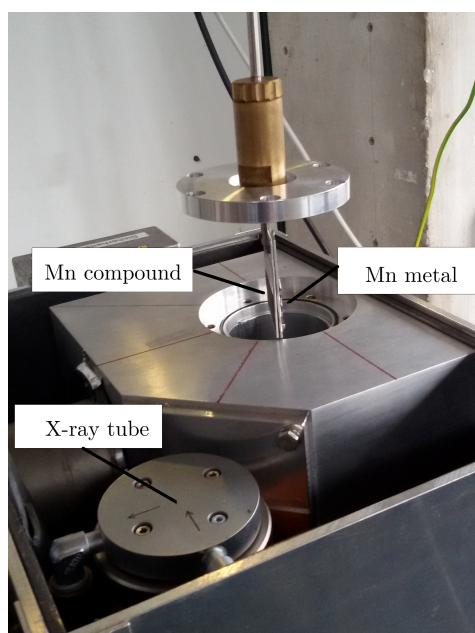

Fig. 5.8. : Target chamber and fluorescence targets mounted on the support bar. For radiation protection, the target chamber and the X-ray tube are surrounded by a 5 mm lead shield embedded in an aluminium cover.

measuring time. The exact relation of the counts of metal to compound is determined from a first analysis comparing the integral accumulated in the spectra normalised to the number of frames. In the end approximately two weeks in total is needed for the whole measurement of one metal-compound pair. This was done by measuring 8 hours per day. Typically, a one hour measurement of the metallic manganese was followed by a longer period for the manganese compound.

5.2.3. Background studies

In the beginning of the experiment, the set-up was studied for a possible occurrence of contamination lines. Therefore, the target support of pure aluminium covered by a layer
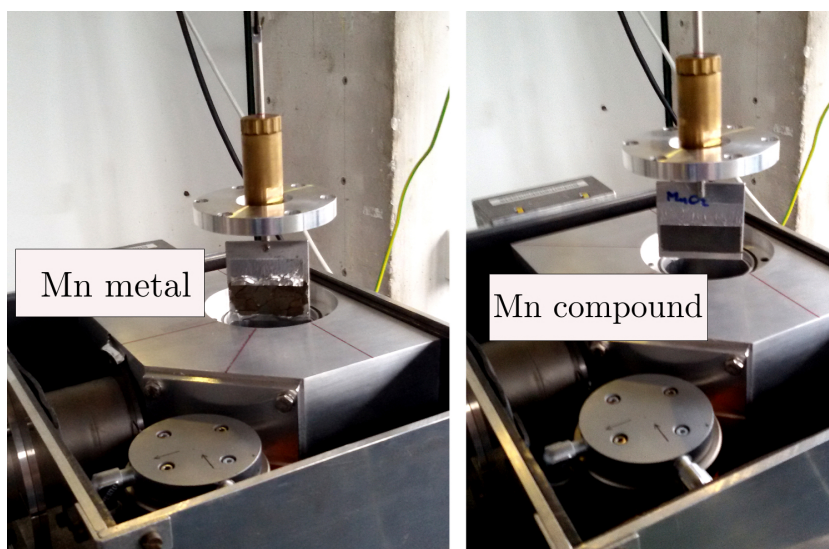
Fig. 5.9. : Fluorescence targets and holding container. By rotating support bar by 180^0, alternation of back-to-back mounted targets are possible without breaking the vacuum or touching the angular set-up of the spectrometer.

of the glue (see Fig. 5.10) as used to fix the fluorescence material was irradiated. In this way it could be verified, that the energy range of the manganese K radiation is free of background lines.
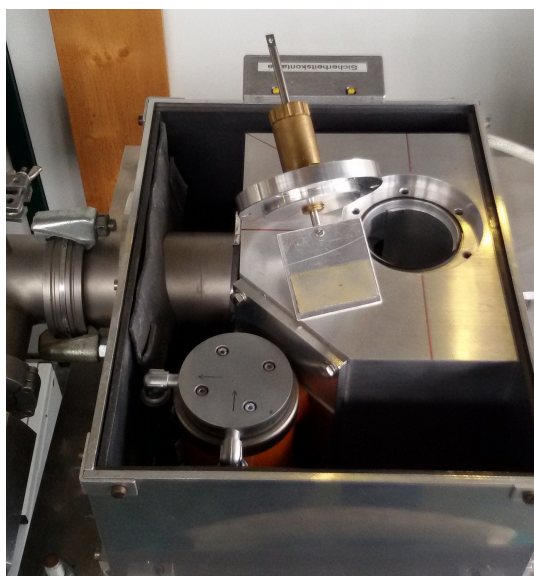

Fig. 5.10. : Pure aluminum with a glue as a target.

5.2.4. Monitor for the spectrometer stability

From the experimental point of view it is of advantage that from the data itself a criterion for the stability of set-up can be extracted. For this, the peak positions in the spectra generated from the reflection data can be used. Stability was checked every single day of the measurement period separately for Mn metal and compound, *i. e.* metal to metal and compound to compound. The peak positions varied at maximum one pixel during the whole measurement period. As an example, the measurement of the pair metal/Mn (V) compound

43

is shown for metal (see Fig. 5.11). From Fig. 5.11 one can deduce that during the measurement process the fluorescence X-rays reflected from the Bragg crystal are focused on the same position of the CCD semiconductor detecor with a deviation of maximum one pixel. The same tendency was observed in case of manganese compounds, which makes possible to conclude that our experimental measurements are conducted under a long-term stability of the set-up.

Actually this procedure tests the performance of the Labview[©]-based monitoring and control SCADA system monitoring and stabilizing the various spectrometer components. Noteworthy the long-term stability being crucial to conduct such high-precision measurements.
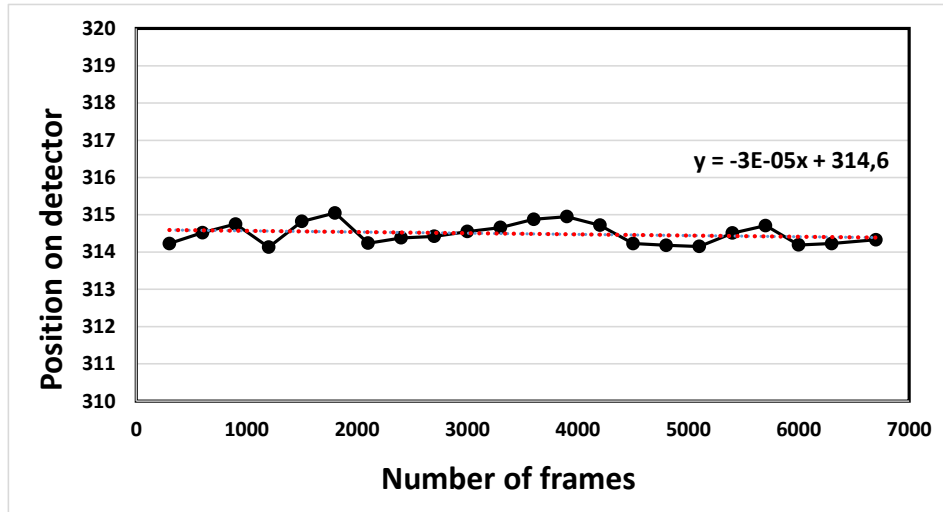

Fig. 5.11. : Time dependence of the metallic manganese $K\alpha_1$ peak position. One pixel corresponds to 156 meV in X-ray energy. Total measuring time was 104 hours spanning over 2 weeks.

6. DATA ANALYSIS

6.1. Data processing

6.1.1. Raw data

The files containing the raw data are processed, displayed and manipulated with the program CSDCLUSTER [60]. It decodes the raw-data format (see Fig. 5.4) back to an (x, y) coordinate corresponding to the pixels' location in the CCD plane and its associated charge contents. Pixels having a charge contents lower than the threshold applied for data taking are set to an ADC value of zero. The recorded frames are processed individually and then summed up for various parameters. Display options are among others the X-ray hit pattern (scatterplot), energy spectrum (ADC spectrum), and the position spectrum along the direction of dispersion being equivalent to the energy spectrum.

6.1.2. Charge contents

In the few keV range photons convert almost completely via photo effect. The range of the photo electron is a few tenth of μm only. Therefore, all charge is kept under one pixel or in two adjacent pixels if conversion happens in the depleted region and the X-ray spectrum maybe generated from single- or two-pixel cluster only.

Fig. 6.1 - left shows the charge spectrum collected in individual pixels. The prominent peak corresponds to the full energy of the manganese Kα radiation of 5.9 keV where the complete charge is collected in one pixel (photo peak). For this energy, X-rays can reach also the silicon bulk part close to the depleted region of the CCD from where the charge may drift into several pixels forming larger clusters (charge splitting). The average cluster size increases with increasing X-ray energy and has been analysed for a CCD22 device [49]. The increasing intensity on the continuum towards lower charge is entirely due to split events, on top of which the single escape peak of silicon appears. The noise peak is completely removed by the cut at channel 100.

A small numbers of double hits is visible at the charge value corresponding to twice the photo peak (Fig. 6.1 - right). The fraction of such double hits has to be taken into account for the analysis of the hit pattern. Therefore, this type of events was kept on purpose at the level of a few % at most. The level of double hits was adjusted by means of the current of the X-ray tube (see Chap. 5.1.3).

The treatment of the double and split events affects strongly the position spectrum. A detailed description of the strategy to perform a cluster analysis is given in Chap. 6.1.4.

6.1.3. Hit pattern and position spectrum

The position spectrum is generated by projecting the hit pattern to the direction of dispersion which eventually constitutes the energy spectrum aimed at. In order to keep the resolution of the Bragg spectrometer, any curvature or tilt of the reflection has to be corrected.
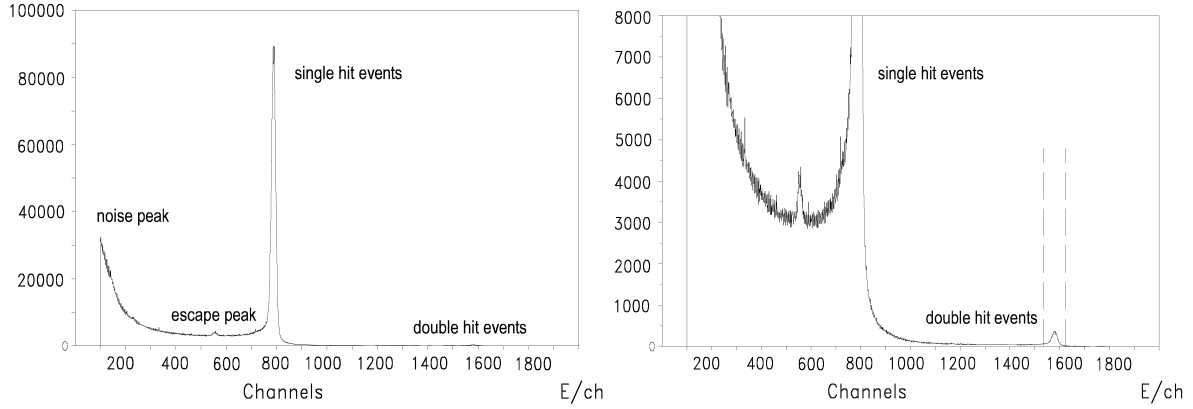
Fig. 6.1. : Left - Charge contents of single pixels from a manganese Kα reflection. Right - As spectrum left but extended vertical scale. The small peak at the charge corresponding to twice the photo peak shows double hits of a Mn Kα X-ray in one pixel during the illunmination period.

The hit pattern of the Kα doublet emitted from metallic manganese is shown in Fig. 6.2. As discussed in Chap. 2.2.1, the image of the source for monoenergetic X-rays is approximately a hyperbola in the detection plane (see Fig. 6.5). In addition, a tilt of the reflection appears if the symmetry plane of the Johann set-up and detector are not ideally aligned.

In this experiment, due to the small detector size and target dimensions compared to the bending radius of the crystal, the curvature of the reflection turns out to be negligibly small. Here, the detector size covers only about 25% of the diffracted intensity (see Fig. 6.5). Therefore, only the tilt correction remains, which is sufficiently well parametrised by a straight line ($f(x) = bx + c$). The result of the curvature correction is demonstrated in Fig. 6.2.

Usually the curvature fit is done for the double hit distribution. It is narrower than the X-ray line, because double hits preferentially occur only around the peak maximum. ADC cuts around the corresponding charge peak further improve the result. Fitting procedure is continued until the value of χ^2 is nearby 1 and stays stable. The coefficients of the fit are expected to be equal within the errors for metal and corresponding compound and serve as an additional stability check. Noteworthy, for the analysis of the metal-compound pair identical curve correction parameters must be used.
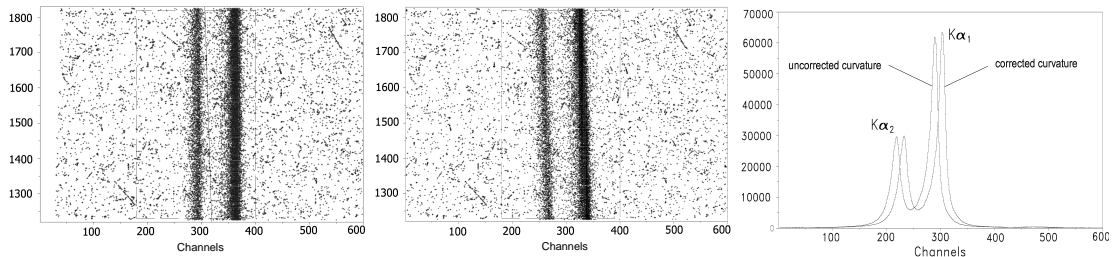

Fig. 6.2. : Hit pattern of the Kα doublet of metallic manganese in the detector plane, before (left) and after (middle) curvature correction, and position spectrum before and after curvature correction (right).

6.1.4. Cluster analysis and charge cuts

A cluster is defined as the pattern of adjacent pixels of the detector, which is separated from all other clusters by at least one empty pixel distance. Usually, the cluster analysis is essential to suppress X-ray events from background, which may be enormous when working

in accelerator environments [1, 3]. The beam-induced background typically stems from charge particles or Compton scattering which produce extended clusters. The program CSDCLUSTER provides a cluster analysis where the range of cluster sizes can be varied between 1 and 25.

As discussed in Chap. 4.3, data collected in this experiment can be regarded as background free and all pixel contents besides the photo peak can be attributed to split or double events (Fig. 6.1). Two main sources of distortion of the position occur:

- The cluster analysis switched off, accepting all individual pixels with all possible charge contents for the position spectrum, leads to double counting. This is avoided, if for single hit events a charge window is set for ADC channels $450 - 900$ (in the case of Kα radiation) assuming that the maximum charge of the second or higher pixel of a split event is at maximum half of that of the photo peak. However, events may be missed when a charge is distributed about equally over several pixels. For double hit events the cut is set to channels $900 - 1650$ charge an area from the end of single events peak until the end of double events peak. The position spectrum of the double hits is then added twice to the one for single hits.

- When using sharp cluster cuts, it turned out that restricting to cluster 1-2 events suppresses events in the peak. There the density of hits is so high, that 1-2 cluster events are no longer isolated and, therefore, interpreted as larger clusters and rejected.

  The effect of overlapping clusters can be verified from the charge spectrum of the clusters with sizes 1-25 (Fig. 6.3). The total charge adds up to an amount corresponding to the energy of several photons of 5.9 keV, *i. e.* the large clusters can be interpreted as overlapping clusters. Cluster size 1 and 2 events are collected in sharp peaks corresponding to the photo peak of single, double and even triple hits. Larger clusters suffer from incomplete charge collection and form the broader peaks at the low-energy side of the photo peaks.

  The position spectra corresponding to the various multi-hit events are extracted individually using the appropriate charge cuts and then added up to the total position spectrum. Numbers in Fig. 6.3 indicate the multiplier which has to applied to multiple hit events (number 2 corresponds to double hit events, 3 to triple and so on). Individual position spectra are saved by the CSDCLUSTER program separately in a form of ASCII files. These files are summed up by the program FITOS [61] used also for the final analysis to fit the line shape.

In order to decide which cluster treatment is most appropriate, the total line width of the Kα and Kβ peaks of metallic manganese can be used, which well known from literature [8] (these numbers are for Kα_1 - 2.47 eV, for Kα_2 - 2.92 eV and for $K\beta_{1,3}$ - 2.97 eV).

Comparing the position spectra metallic manganese when using no cluster, cluster size 1-2, and cluster size 1-25, reveals that cluster size 1-2 clearly suppresses the peak region of the spectrum (see Fig. 6.4). The best agreement was found in case of Kα when using cluster size 1-25 and for Kβ cluster off.

6.2. Spectrometer response

An important aspect of the data analysis in the field of high-resolution X-ray spectrometry is the response function of the spectrometer. Here, the response function of the spectrometer is build up from various components. At first, the intrinsic resolution of the crystal material is
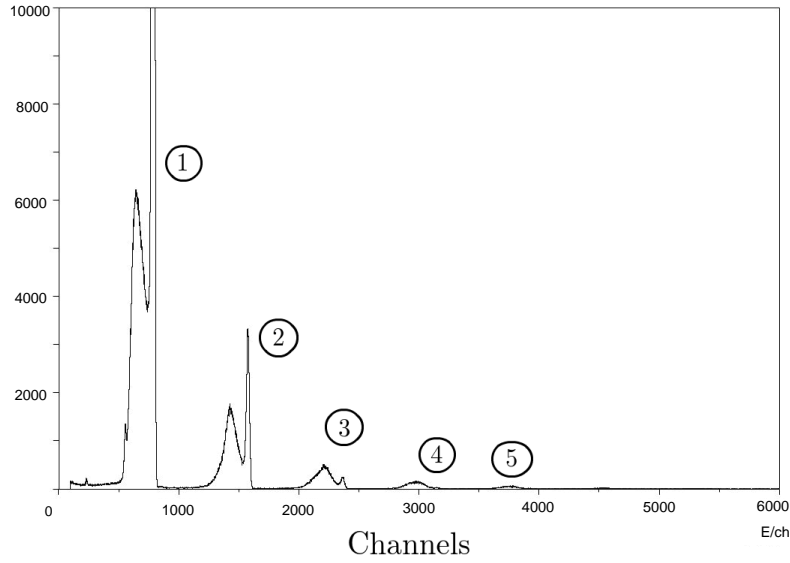
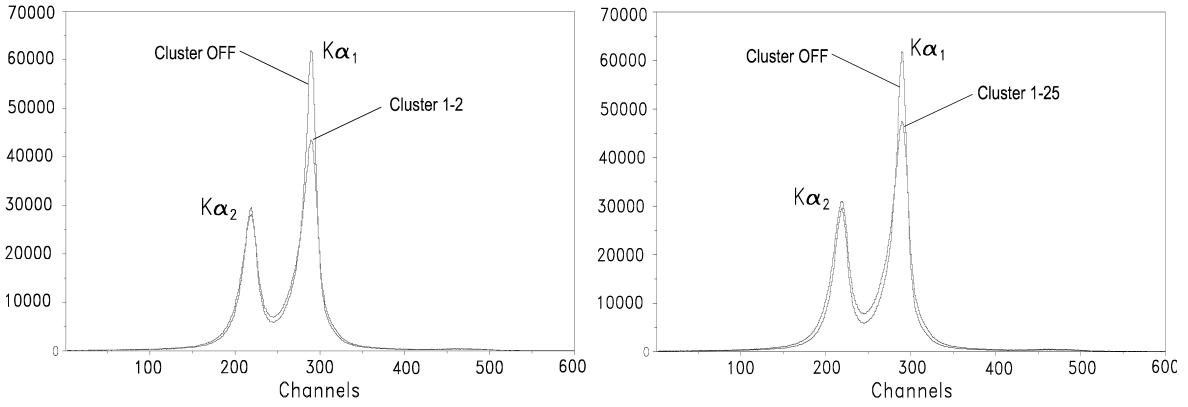**Fig. 6.3.** : ADC spectrum using clusters 1-25.

Fig. 6.4. : Position spectrum of metallic manganese considering different cluster analysis approaches.

calculated for the specific reflection by using the XOP package [45] (narrow lines in Fig. 6.5-right). By interpreting the XOP result as a probability density function of the reflection angle around the Bragg angle, it is input of the tracking routine XTRACK [62] simulating the imaging properties of the bent crystal and other geometrical conditions of the experimental set-up. The routine XTRACK produces a hit pattern in the detection plane (Fig. 6.5- left). After applying curvature and tilt correction, the pattern is projected to the axis of dispersion, which constitutes the calculated response of the spectrometer. Though being in principle asymmetric, it turns out that the response can be parametrised well enough by a Gaussian (Fig. 6.5-right).

Additional information for the spectrometer response is obtained from measurements using the narrow M1 transition in medium Z helium-like atoms [42]. The experimentally determined resolution is then compared with the intrinsic resolution of the crystal material as calculated by using the code XOP and convoluted with aberrations due to the set-up again by means routine XTRACK. It was found, that deviations are sufficiently well modelled by an additional Gaussian contribution and are assumed to stem from surface distortions and crystal mounting imprecision. Therefore, the total response can still be parametrised by a single Gaussian.
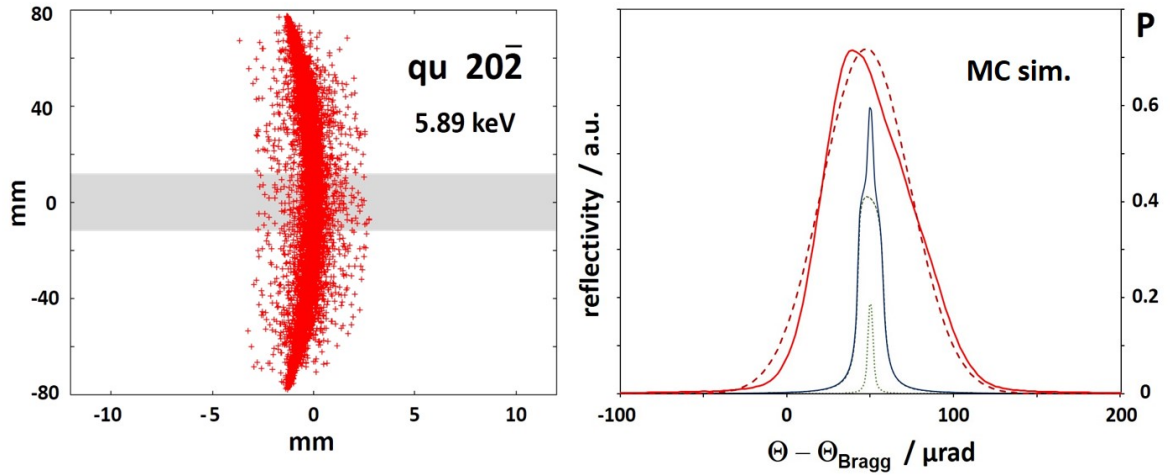
Fig. 6.5. : Monte-Carlo simultion of the spectroemter response for the Mn Kα line. Left – Hit pattern in the detection plane. The grey area corresponds to the size of the detector (Horizontal and vertical directions are not in scale). Right – Projetion of the hit pattern to the axis of dispersion after curvature correction (only from the part covered by the detector). The dashed line is the approximation of the resolution function by a Gaussian. The narrow lines show the intrinsic resolution of the quartz $20\bar{2}$ reflection consisting of the sum of the contributions σ and π (small) polarisation. The right scale represents the corresponding peak reflectivity P.

In measurements with sulphur (2.4 keV) and argon (3.1 keV), the additional Gaussian width was determined to be (42 ± 2) and $(32 \pm 3)\,\mu$rad (FWHM), respectively [42]. As the additional broadening decreases with X-ray energy, the value obtained at 3.1 keV is considered to be an upper limit for the energies considered in this experiment, which corresponds to 6.6 seconds of arc or 230 and 300 meV for the Mn Kα and Kβ energies, respectively.

The rocking curves for 5.9 and 6.5 keV for a plane crystal have widths of about to 15 and 13 μrad (FWHM), which corresponds to about 110 and 120 meV. After convolution with the experimental geometry and including the additional Gaussian, energy resolutions of (420 ± 40) and (610 ± 50) meV (FWHM) are obtained for the Mn Kα and Kβ case. This corresponds to 2.7 CCD channels or pixel for the Kα and 2.8 for Kβ position spectra.

This constitutes resolutions of $E/\Delta E \sim 14000$ and $E/\Delta E \sim 10500$. Omitting completely the Gaussian contributions yields already 350 and 530 meV, respectively, *i. e.* the experimental resolution is dominated by geometrical aberration. these values are about 40% larger than expected from the simple estimate given in eq.(2.19). As the line widths of the Mn Kα and Kβ lines are between 1.5 and 5 eV, the influence of the uncertainty of the resolution function is marginal.

6.3. Spectra overview

As mentioned in Chap. 1, the Kα doublet or the K$\beta_{1,3}$ structure shows several satellite components besides the diagram lines. The positions are indicated in an overview figure collecting all measurements (Fig. 6.6). The assignment is explained in Tab. 1.1.
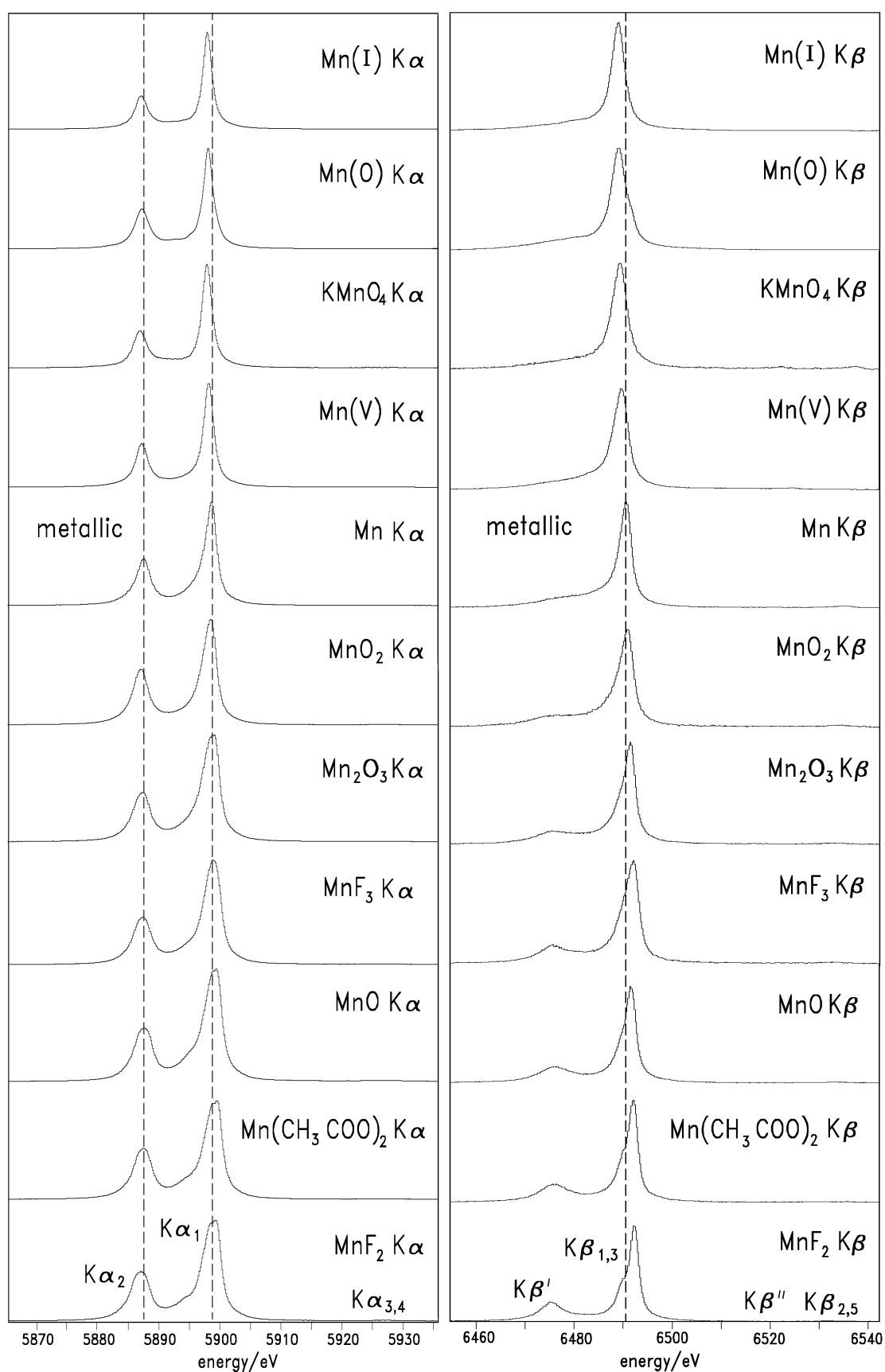
Fig. 6.6. : Overview of the measured Kα and Kβ structures. Ordering is done according to the increasing line energy.

7. RESULTS

7.1. Fits to the line shape

The components which are necessary to describe the X-ray patterns widely overlap and often cannot be resolved as individual lines. Therefore, a phenomenological approach is chosen to describe the total line shape of X-ray spectrum similar to the method applied to copper [7] and other $3d$ metals [8]. There, the pattern is constructed from the superposition of Voigt profiles (see Appendix B). The Voigt profile constitutes the convolution of a Lorentzian and a Gaussian, where the Gaussian represents the fixed response of the spectrometer (Fig. 6.5).

The fits to the line shape are performed with the program FITOS, where the spectra created by the CSDCLUSTER program are imported. In the fit, for all components the position, Lorentzian width, and intensity are free parameters. The Gaussian component is always kept fixed. An example output of FITOS is shown in Fig. 7.1. It is worth to mention that the emission spectrum is free of background events, which is achieved by a suitable source geometry (Chap. 4.3).

Position	Gauss-FWHM	Height	Low-tail	High-tail	Lorentz-FWHM	Intensity	Background	
Peak 1								
357.850	2.70	35715.92	0.00	0.000	11.49	644571.87	15.11	$K\alpha_1$
0.011	0.00	82.81	0.00	0.000	0.03	1230.52	0.93	
Peak 2								
287.191	2.70	11883.19	0.00	0.000	15.46	288495.74	15.11	$K\alpha_2$
0.027	0.00	43.72	0.00	0.000	0.10	1787.92	0.93	
Peak 3								
314.120	2.70	1671.03	0.00	0.000	59.69	156681.44	15.11	Intermediate
0.471	0.00	20.02	0.00	0.000	0.65	2308.17	0.93	
Peak 4								
530.000	2.70	120.00	0.00	0.000	29.00	5466.37	15.11	
0.000	0.00	0.00	0.00	0.000	0.00	0.00	0.93	$K\alpha_{3,4}$
Peak 5								
562.950	2.70	160.00	0.00	0.000	35.00	8796.46	15.11	
0.416	0.00	0.00	0.00	0.000	0.00	0.00	0.93	

Fig. 7.1. : Output of FITOS, displaying the fit results for the $K\alpha$ line of KMnO$_4$ compound (Fig. 7.4). Numbers under the parameter values represent their corresponding uncertainties. Zero value indicates that the parameter is fixed instead of being free for the fit.

Due to the complexity of the line shape, the fit procedure is performed iteratively. First, only the main components are fitted, which leads to an over- or undershoot of the intensity at various positions. The deviations are then taken into account by additional components, where now the main peak parameters are fixed. In the next step, the small peak parameters are fixed and the main peaks readjusted. In this way, the procedure is continued until a satisfactory agreement is achieved.

Depending on complexity, between 3 (KMnO$_4$) and 8 (Mn(CH$_3$COO)$_2$) components are needed for the phenomenological description of the line shape of the $K\alpha$ doublet. In addition the $K\alpha_{3,4}$ satellite complex was taken into account to avoid any influence on positions and widths of the main $K\alpha$ components. Due to the almost doublet-like structure and having

energies being about 30 eV higher than the $K\alpha_1$ line, a two-line fit for the $K\alpha_{3,4}$ region is sufficient. The structure of these lines owing mainly to additional L vacancies is discussed in detail by [21, 22].

The $K\beta_{1,3}$ main peak is usually described by three components. The high energetic satellites of the $K\beta_{1,3}$ structure, $K\beta''$ and $K\beta_{2,5}$, are separated by about 40 and 70 eV and fitted well enough by single lines each. The low-energy satellite structure $K\beta'$ requires in general one component.

7.2. Peak energies

A physical definition of the line energy as a centre of gravity of a single line is unsatisfactory, because the main peaks ($K\alpha_1$ and $K\alpha_2$ in $K\alpha$ spectrum and $K\beta_{1,3}$ in $K\beta$ spectrum) are already a superposition of several components. Therefore, the only unambiguous definition of wavelength or energy of the lines is possible by using the absolute maximum. Obviously, such a definition does not attribute the peak to a specific physical transition and, in addition, depends on fit model and resolution function chosen to describe the line shape.

In order to calculate the absolute maximum of the main peak, the parameters of all components contributing and as obtained from the fit have to be used (see Tabs. 7.2 and 7.3). This goal was achieved to a high precision using the program MATHEMATICA. Input values are the subpeak parameters which are the result of the lineshape fitting with FITOS. Uncertainties of the positions of the main peaks have been evaluated by varying the input parameters within their errors. In this way, the peak energy is determined with the spectrometer response taken out. Peak energies of the various compounds are given in Tab. 7.1. The value for Mn metal, as reported by Hölzer et al. [8], but readjusted by [29] because of the redetermination of the conversion constant, constitutes the absolute energy calibration.

A doublet-like splitting is observed for the MnF_2 of the $K\alpha_1$ line (Fig. 7.2). From this experiment, there is evidence for such a splitting also for other compounds with manganese being in formal ionisation state II (MnO_2 and $Mn(CH_3COO)_2$). Nevertheless, to be consistent, the peak energies are given always by the absolute maximum.
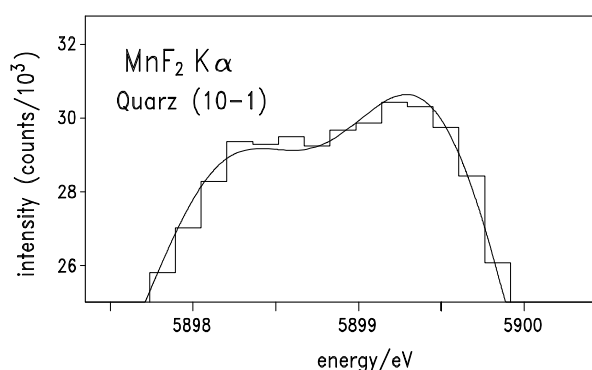

Fig. 7.2. : Detail of the $K\alpha_1$ line shape near the peak in MnF_2.

Based on physical considerations other possibilities exist to attribute the line energies of individual components to physical processes, which are discussed in Chap. 8. Furthermore, a theoretical approach in order to obtain relative energy shifts by means of molecular orbital calculations is outlined in sect. 8.4 for selected compounds.

Table 7.1. : Kα_1, Kα_2, and K$\beta_{1,3}$ peak transition energies of the various compounds derived from the angular distance to the Kα_1 peak positions for metals. The calibration energies energies are 5898.801 eV for Kα_1 and 6490.585 eV for Kβ_{13} peaks [29], which are readjusted values of [8].

	ionisation no.	no of unpaired electrons	Kα_1			Kα_2			K$\beta_{1,3}$		
Mn (metal)			5898.801	±	0.008	5887.686	±	0.008	6490.585	±	0.014
Mn(0)	0	1	5898.033	±	0.015	5887.191	±	0.018	6488.969	±	0.016
Mn(I)	I	0	5898.036	±	0.010	5887.163	±	0.012	6488.946	±	0.016
MnF$_2$	II	5	5899.397	±	0.019	5887.274	±	0.013	6492.288	±	0.026
MnO	II	5	5899.422	±	0.027	5887.721	±	0.023	6491.671	±	0.019
Mn(CH$_3$COO)$_2$	II	5	5899.479	±	0.018	5887.541	±	0.014	6492.028	±	0.024
MnF$_3$	III	4	5898.735	±	0.028	5887.437	±	0.021	6492.077	±	0.025
Mn$_2$O$_3$	III	4	5899.195	±	0.012	5887.455	±	0.010	6491.529	±	0.018
MnO$_2$	IV	3	5898.651	±	0.015	5887.149	±	0.012	6490.937	±	0.017
Mn(V) complex*	V	2	5898.201	±	0.026	5887.264	±	0.017	6489.545	±	0.027
KMnO$_4$	VII	0	5897.857	±	0.012	5886.877	±	0.011	6489.263	±	0.016

*the structure of the Mn(V) complex is described in ref. [63]

7.3. Line shape of Kα spectra

Figures 7.3 and 7.4 show the decomposition of the line shape of the Kα spectra. In Table 7.2, the parameters are given of the individual components as obtained from fits using Voigt profiles.
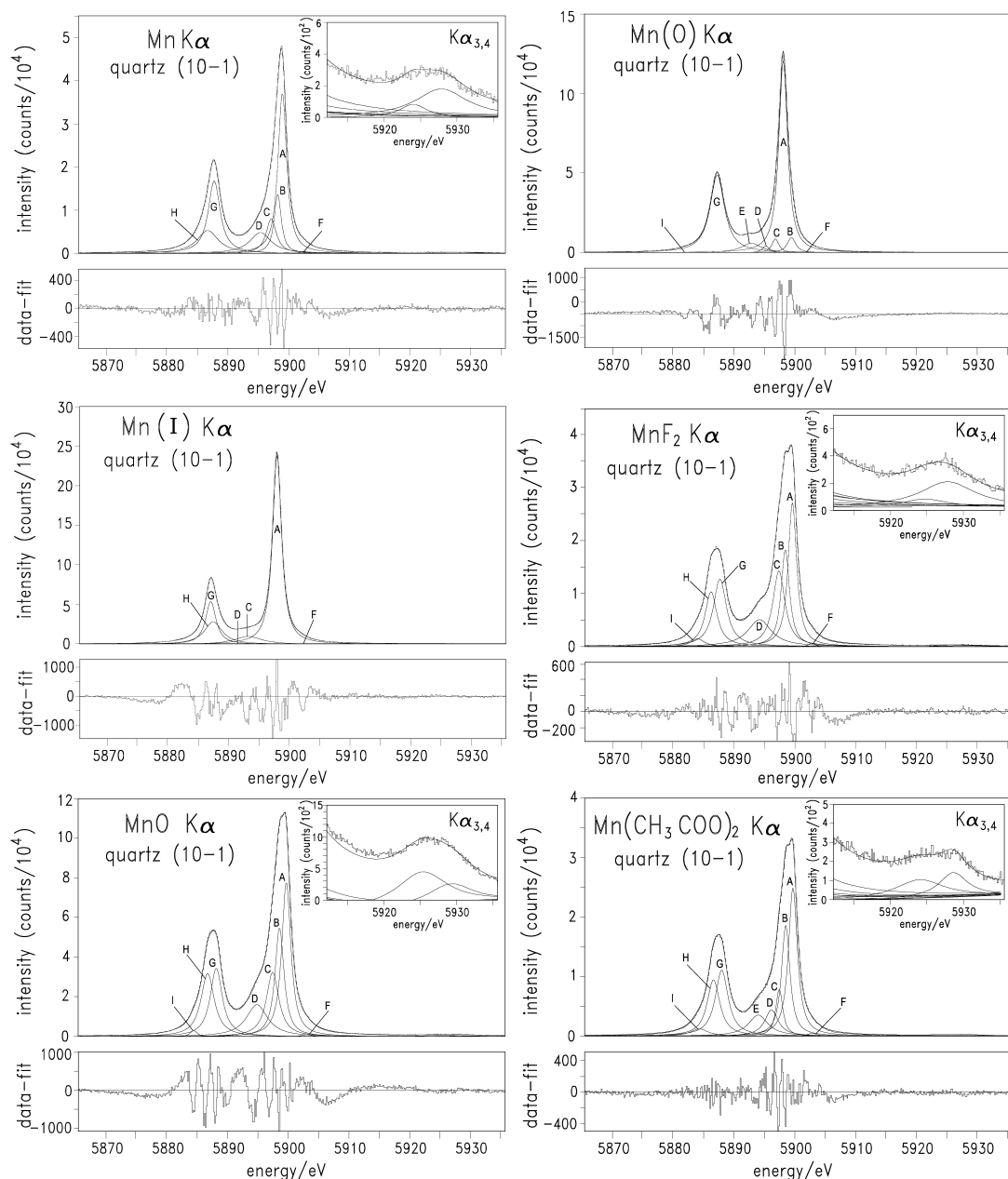
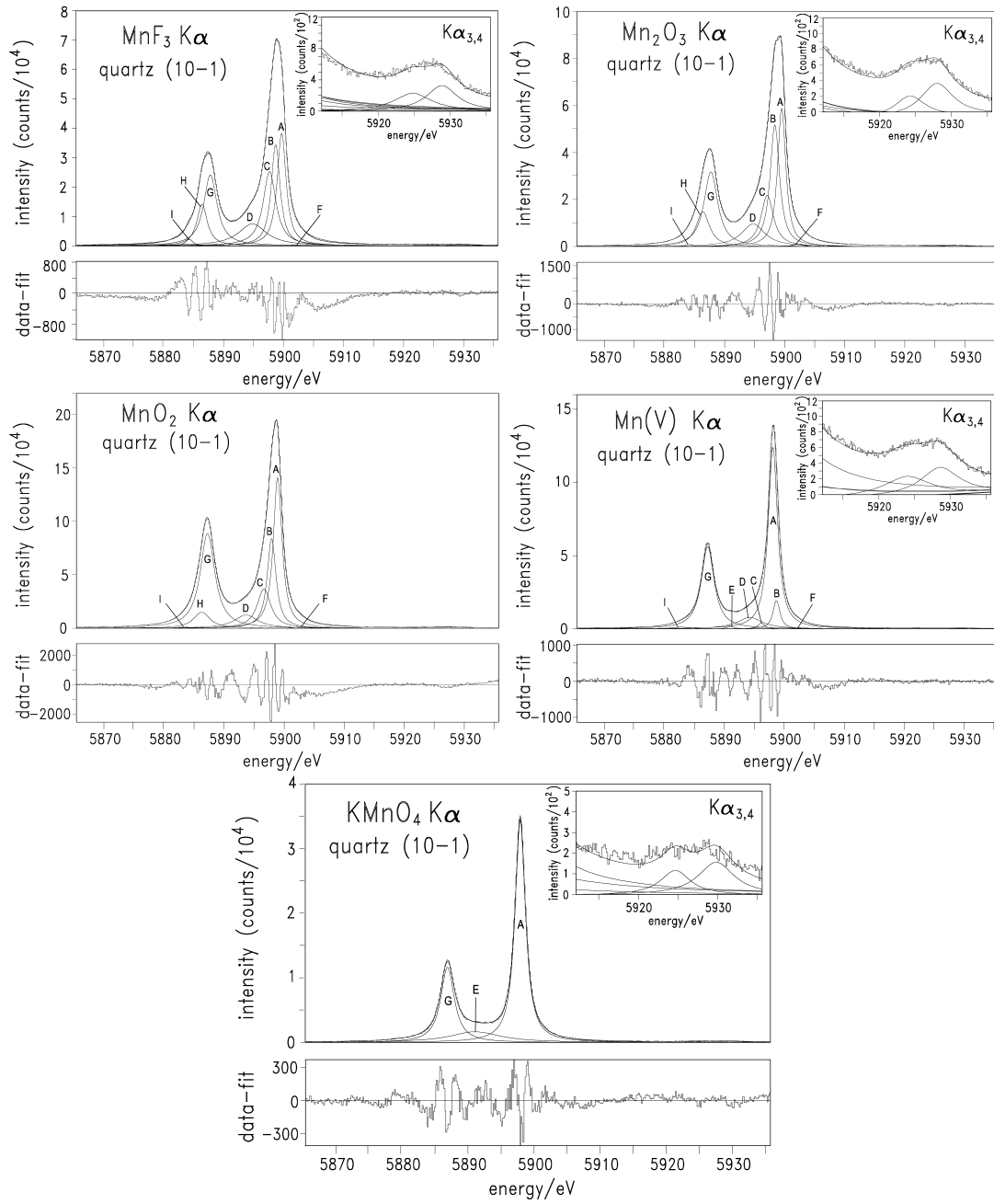**Fig. 7.3.** : Line shape of measured Mn Kα spectra: Mn metal, Mn(0), Mn(I), MnF₂, MnO, Mn(CH₃COO)₂.

Fig. 7.4. : Line shape of measured Mn Kα
spectra-continued: MnF$_3$, Mn$_2$O$_3$,
MnO$_2$, Mn(V), KMnO$_4$.

Table 7.2. : Mn Kα doublet: parameters of the components as obtained from fits using Voigt profiles. E_i: energy, I_i: intensity relative to the full intensity of the Kα doublet$_i$, L_i: Lorentz width (FWHM). Reference energy are the Kα peak energies of metallic managanese of E = 5898.801 eV (from [29]). Component notation with * denotes its belonging to Kα_1 peak and the component notation with ** denotes the contribution to Kα_2 peak.

compound	component	E_i / eV	I_i	L_i / eV	$I_{K\alpha_2}/I_{K\alpha_1}$
	$\alpha_A{}^*$	5898.955 ± 0.013	0.35 ± 0.01	1.59 ± 0.01	
	$\alpha_B{}^*$	5898.191 ± 0.029	0.10 ± 0.01	1.28 ± 0.05	
	$\alpha_C{}^*$	5897.128 ± 0.022	0.09 ± 0.01	1.93 ± 0.07	
Mn (metal)	$\alpha_D{}^*$	5895.343 ± 0.043	0.11 ± 0.01	4.16 ± 0.07	0.52
	$\alpha_F{}^*$	5902.501 ± 0.047	0.01 ± 0.01	1.25 ± 0.14	
	$\alpha_G{}^{**}$	5887.726 ± 0.013	0.22 ± 0.01	2.28 ± 0.05	
	$\alpha_H{}^{**}$	5886.667 ± 0.100	0.13 ± 0.01	4.19 ± 0.06	
	$\alpha_A{}^*$	5898.033 ± 0.002	0.51 ± 0.01	1.62 ± 0.01	
	$\alpha_B{}^*$	5899.391 ± 0.011	0.04 ± 0.01	1.56 ± 0.03	
	$\alpha_C{}^*$	5896.747 ± 0.016	0.02 ± 0.01	1.24 ± 0.03	
Mn(0)	$\alpha_D{}^*$	5895.184 ± 0.016	0.01 ± 0.01	1.24 ± 0.05	0.53
	$\alpha_E{}^*$	5892.782 ± 0.019	0.06 ± 0.01	3.96 ± 0.08	
	$\alpha_F{}^*$	5901.573 ± 0.078	0.01 ± 0.01	2.18 ± 0.08	
	$\alpha_G{}^{**}$	5887.184 ± 0.002	0.34 ± 0.01	2.79 ± 0.01	
	$\alpha_I{}^{**}$	5881.822 ± 0.042	0.01 ± 0.01	1.87 ± 0.15	
	$\alpha_A{}^*$	5898.038 ± 0.001	0.60 ± 0.01	1.68 ± 0.01	
	$\alpha_C{}^*$	5893.281 ± 0.026	0.08 ± 0.02	5.41 ± 0.12	
Mn(I)	$\alpha_D{}^*$	5891.612 ± 0.024	0.01 ± 0.01	3.06 ± 0.88	0.45
	$\alpha_F{}^*$	5902.103 ± 0.022	0.01 ± 0.01	1.87 ± 0.06	
	$\alpha_G{}^{**}$	5887.098 ± 0.013	0.16 ± 0.02	1.97 ± 0.07	
	$\alpha_H{}^{**}$	5887.498 ± 0.060	0.16 ± 0.01	3.53 ± 0.18	
	$\alpha_A{}^*$	5899.582 ± 0.004	0.23 ± 0.01	1.56 ± 0.01	
	$\alpha_B{}^*$	5898.410 ± 0.011	0.15 ± 0.01	1.56 ± 0.02	
	$\alpha_C{}^*$	5897.357 ± 0.009	0.18 ± 0.01	2.33 ± 0.04	
MnF$_2$	$\alpha_D{}^*$	5894.162 ± 0.032	0.12 ± 0.01	4.59 ± 0.08	0.46
	$\alpha_F{}^*$	5902.770 ± 0.030	0.01 ± 0.01	0.94 ± 0.08	
	$\alpha_G{}^{**}$	5887.642 ± 0.007	0.17 ± 0.01	2.52 ± 0.02	
	$\alpha_H{}^{**}$	5886.181 ± 0.011	0.13 ± 0.01	2.29 ± 0.05	
	$\alpha_I{}^{**}$	5883.946 ± 0.061	0.02 ± 0.01	2.54 ± 0.12	
	$\alpha_A{}^*$	5899.688 ± 0.007	0.25 ± 0.01	1.70 ± 0.01	
	$\alpha_B{}^*$	5898.570 ± 0.012	0.17 ± 0.01	1.69 ± 0.03	
	$\alpha_C{}^*$	5897.443 ± 0.012	0.15 ± 0.01	2.44 ± 0.04	
MnO	$\alpha_D{}^*$	5894.845 ± 0.015	0.12 ± 0.01	4.20 ± 0.04	0.45
	$\alpha_F{}^*$	5903.057 ± 0.044	0.01 ± 0.01	2.02 ± 0.14	
	$\alpha_G{}^{**}$	5888.217 ± 0.012	0.12 ± 0.01	2.20 ± 0.03	
	$\alpha_H{}^{**}$	5886.855 ± 0.014	0.19 ± 0.01	2.89 ± 0.02	
	$\alpha_I{}^{**}$	5884.425 ± 0.023	0.01 ± 0.01	1.25 ± 0.11	
<td colspan="5" align="center">continued on next page</td>

Table 7.2 – continued from previous page

compound	component	E_i (eV)	I_i	L_i (eV)	$I_{K\alpha_2}/I_{K\alpha_1}$
Mn(CH$_3$COO)$_2$	$\alpha_A{}^*$	5899.675 ± 0.005	0.25 ± 0.03	1.66 ± 0.01	
	$\alpha_B{}^*$	5898.481 ± 0.011	0.19 ± 0.05	1.61 ± 0.04	
	$\alpha_C{}^*$	5897.423 ± 0.012	0.06 ± 0.02	1.25 ± 0.05	
	$\alpha_D{}^*$	5896.182 ± 0.025	0.07 ± 0.03	2.76 ± 0.11	
	$\alpha_E{}^*$	5893.966 ± 0.020	0.08 ± 0.01	3.88 ± 0.08	0.51
	$\alpha_F{}^*$	5902.836 ± 0.055	0.01 ± 0.01	1.87 ± 0.15	
	$\alpha_G{}^{**}$	5887.928 ± 0.038	0.18 ± 0.02	2.51 ± 0.07	
	$\alpha_H{}^{**}$	5886.560 ± 0.048	0.13 ± 0.02	2.33 ± 0.14	
	$\alpha_I{}^{**}$	5884.378 ± 0.150	0.03 ± 0.01	3.63 ± 0.28	
MnF$_3$	$\alpha_A{}^*$	5899.594 ± 0.004	0.20 ± 0.01	1.68 ± 0.01	
	$\alpha_B{}^*$	5898.594 ± 0.005	0.18 ± 0.01	1.67 ± 0.02	
	$\alpha_C{}^*$	5897.568 ± 0.018	0.19 ± 0.01	2.44 ± 0.05	
	$\alpha_D{}^*$	5894.749 ± 0.034	0.13 ± 0.01	5.61 ± 0.05	0.42
	$\alpha_F{}^*$	5902.679 ± 0.295	0.01 ± 0.01	3.31 ± 0.67	
	$\alpha_G{}^{**}$	5887.717 ± 0.009	0.18 ± 0.01	2.60 ± 0.02	
	$\alpha_H{}^{**}$	5886.356 ± 0.015	0.10 ± 0.13	2.28 ± 0.03	
	$\alpha_I{}^{**}$	5884.075 ± 0.019	0.01 ± 0.01	1.25 ± 0.07	
Mn$_2$O$_3$	$\alpha_A{}^*$	5899.452 ± 0.005	0.31 ± 0.01	1.51 ± 0.01	
	$\alpha_B{}^*$	5898.323 ± 0.010	0.28 ± 0.01	1.83 ± 0.02	
	$\alpha_C{}^*$	5897.091 ± 0.019	0.11 ± 0.01	2.42 ± 0.04	
	$\alpha_D{}^*$	5894.831 ± 0.035	0.05 ± 0.01	4.92 ± 0.07	0.33
	$\alpha_F{}^*$	5902.414 ± 0.042	0.01 ± 0.01	1.87 ± 0.10	
	$\alpha_G{}^{**}$	5887.672 ± 0.018	0.16 ± 0.01	2.65 ± 0.03	
	$\alpha_H{}^{**}$	5886.366 ± 0.032	0.08 ± 0.01	2.74 ± 0.04	
	$\alpha_I{}^{**}$	5883.996 ± 0.040	0.01 ± 0.01	1.25 ± 0.20	
MnO$_2$	$\alpha_A{}^*$	5898.856 ± 0.002	0.27 ± 0.01	1.63 ± 0.01	
	$\alpha_B{}^*$	5897.862 ± 0.007	0.19 ± 0.01	1.79 ± 0.03	
	$\alpha_C{}^*$	5896.563 ± 0.016	0.10 ± 0.01	2.66 ± 0.03	
	$\alpha_D{}^*$	5893.728 ± 0.021	0.08 ± 0.01	5.66 ± 0.09	0.55
	$\alpha_F{}^*$	5902.705 ± 0.047	0.01 ± 0.01	1.87 ± 0.16	
	$\alpha_G{}^{**}$	5887.296 ± 0.029	0.23 ± 0.02	2.71 ± 0.04	
	$\alpha_H{}^{**}$	5886.544 ± 0.082	0.12 ± 0.02	3.24 ± 0.03	
	$\alpha_I{}^{**}$	5883.266 ± 0.043	0.01 ± 0.01	1.54 ± 0.21	
Mn(V)	$\alpha_A{}^*$	5898.143 ± 0.004	0.51 ± 0.01	1.76 ± 0.01	
	$\alpha_B{}^*$	5898.739 ± 0.015	0.06 ± 0.01	1.25 ± 0.03	
	$\alpha_C{}^*$	5896.247 ± 0.027	0.01 ± 0.01	1.25 ± 0.13	
	$\alpha_D{}^*$	5894.314 ± 0.034	0.09 ± 0.01	5.14 ± 0.11	0.50
	$\alpha_E{}^*$	5891.083 ± 0.027	0.01 ± 0.01	1.25 ± 0.27	
	$\alpha_F{}^*$	5902.263 ± 0.045	0.01 ± 0.01	1.29 ± 0.15	
	$\alpha_G{}^{**}$	5887.258 ± 0.002	0.32 ± 0.01	2.50 ± 0.01	
	$\alpha_I{}^{**}$	5882.825 ± 0.055	0.01 ± 0.01	3.95 ± 0.12	
KMnO$_4$	$\alpha_A{}^*$	5897.859 ± 0.002	0.73 ± 0.01	1.79 ± 0.01	
	$\alpha_E{}^{**}$	5890.866 ± 0.07	0.04 ± 0.01	9.20 ± 0.10	0.38
	$\alpha_G{}^{**}$	5886.859 ± 0.004	0.24 ± 0.01	2.40 ± 0.02	

7.4. Line shape of K*β* spectra

Figs 7.5 and 7.6 and Tab. 7.3 show the components of the K*β* line shape.
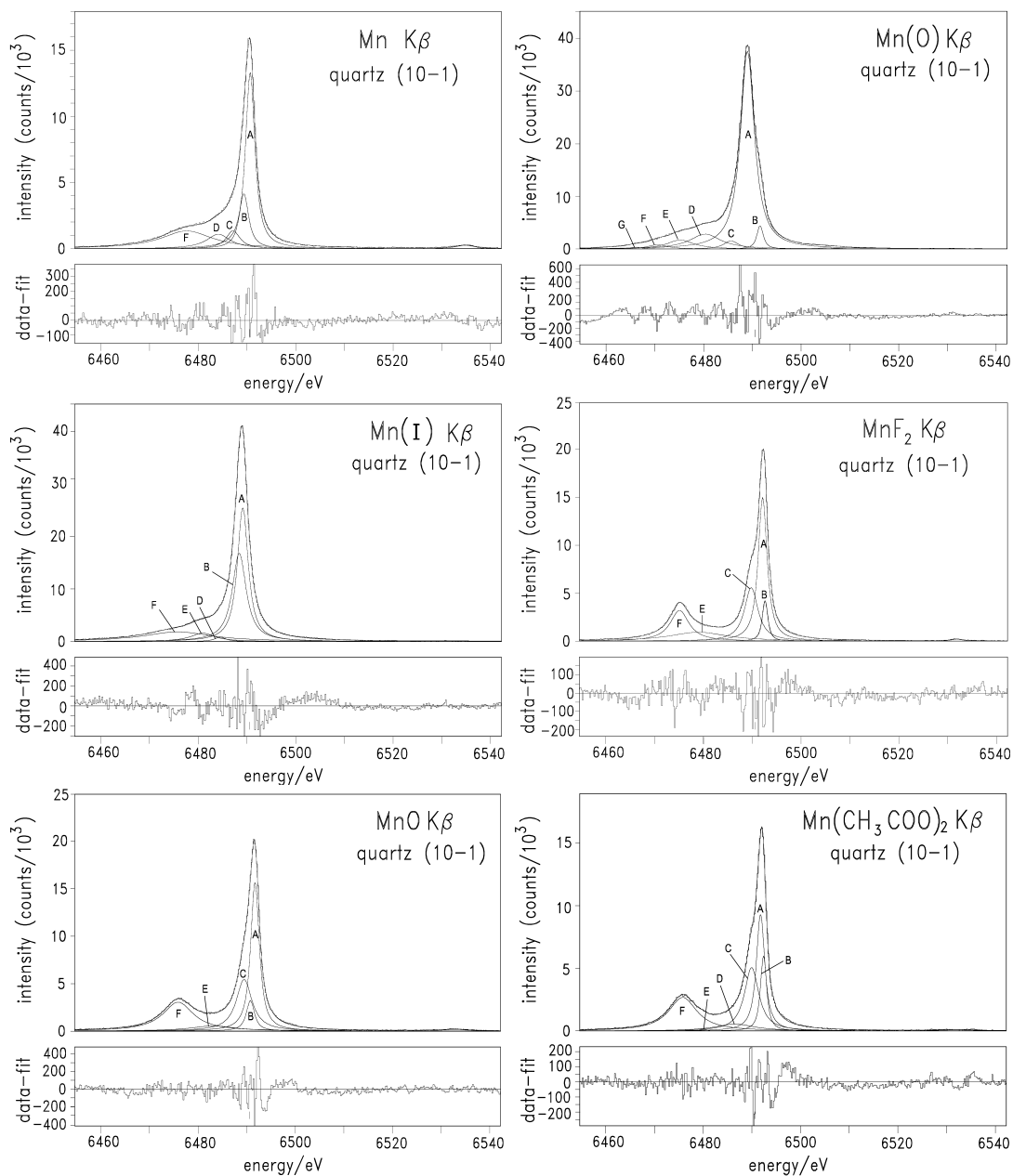

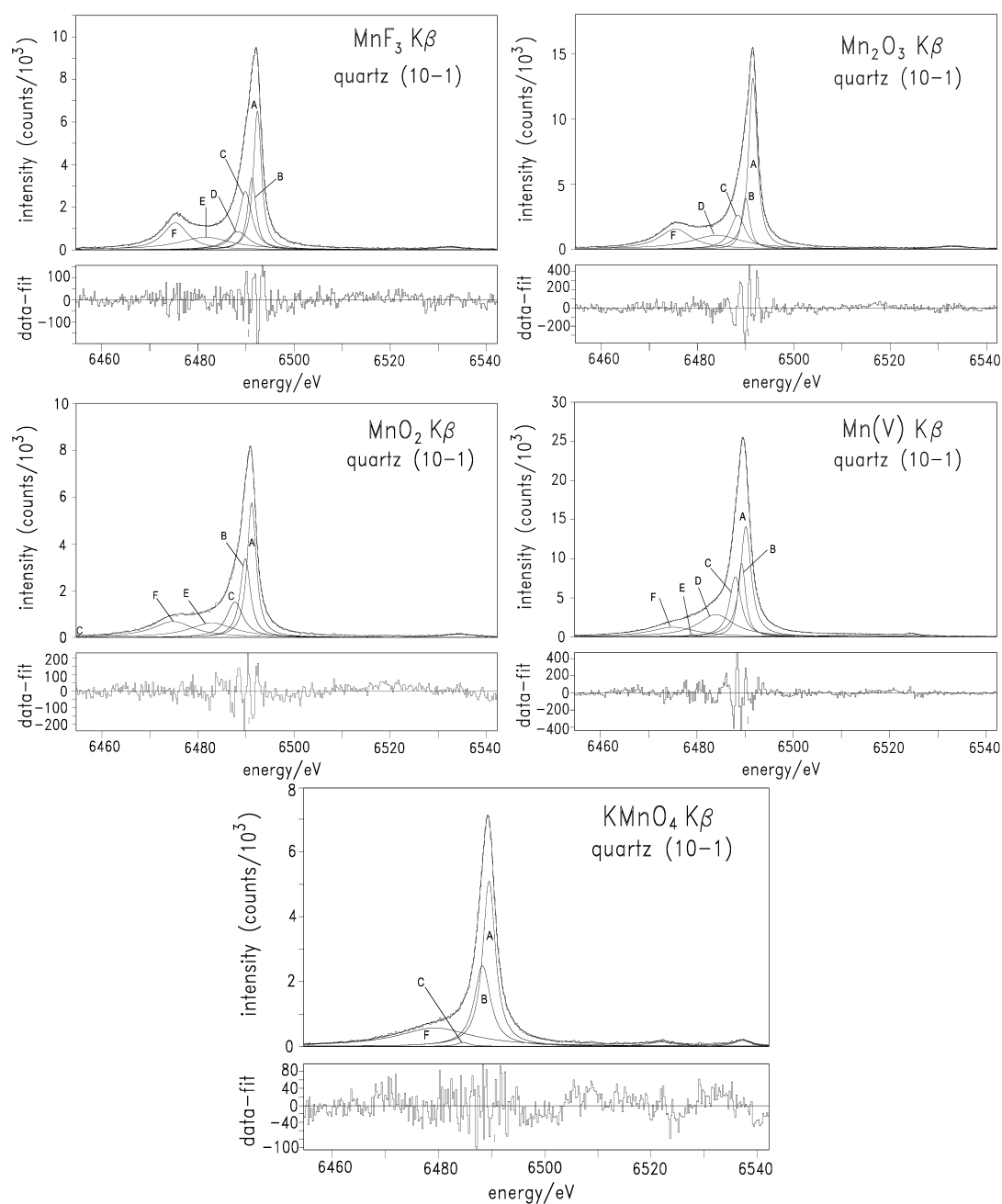**Fig. 7.5.** : Line shape of measured Mn K*β* spectra: Mn metal, Mn(0), Mn(I), MnF$_2$, MnO, Mn(CH$_3$COO)$_2$.

Fig. 7.6. : Line shape of measured Mn Kβ
spectra-continued: MnF$_3$, Mn$_2$O$_3$,
MnO$_2$, Mn(V), KMnO$_4$.

Table 7.3. : Mn Kβ complex: parameters of the components as obtained from fits using Voigt profiles. E_i: energy, I_i: intensity relative to the full intensity of the Kβ complex, L_i: Lorentz width (FWHM). Reference energy is the K$\beta_{1,3}$ peak energy of metallic mananganese of $E = 6490.585$ eV (from [29]).

compound	component	E_i (eV)	I_i	L_i (eV)
	β_A	6490.697 ± 0.007	0.44 ± 0.01	2.12 ± 0.01
	β_B	6489.398 ± 0.021	0.14 ± 0.01	2.17 ± 0.09
Mn (metal)	β_C	6487.186 ± 0.082	0.07 ± 0.01	3.30 ± 0.18
	β_D	6484.177 ± 0.095	0.10 ± 0.01	5.85 ± 0.31
	β_F	6477.692 ± 0.095	0.25 ± 0.01	12.73 ± 0.14
	β_A	6488.971 ± 0.004	0.72 ± 0.01	3.33 ± 0.01
	β_B	6491.567 ± 0.013	0.04 ± 0.01	1.34 ± 0.05
	β_C	6485.615 ± 0.072	0.03 ± 0.01	3.50 ± 0.20
Mn(0)	β_D	6480.336 ± 0.055	0.12 ± 0.01	7.66 ± 0.14
	β_E	6475.202 ± 0.071	0.06 ± 0.01	6.56 ± 0.11
	β_F	6470.577 ± 0.069	0.02 ± 0.01	4.81 ± 0.20
	β_G	6466.113 ± 0.060	0.01 ± 0.01	2.63 ± 0.16
	β_A	6489.141 ± 0.015	0.40 ± 0.02	2.52 ± 0.02
	β_B	6488.416 ± 0.033	0.34 ± 0.02	3.32 ± 0.06
Mn(I)	β_D	6484.507 ± 0.097	0.01 ± 0.01	$2.69, \pm 0.38$
	β_E	6480.929 ± 0.063	0.06 ± 0.01	5.91 ± 0.30
	β_F	6475.787 ± 0.111	0.19 ± 0.01	16.74 ± 0.13
	β_A	6492.158 ± 0.008	0.38 ± 0.01	1.98 ± 0.03
	β_B	6492.673 ± 0.021	0.06 ± 0.01	1.07 ± 0.08
MnF$_2$	β_C	6489.826 ± 0.028	0.22 ± 0.01	3.20 ± 0.05
	β_E	6479.049 ± 0.113	0.16 ± 0.01	14.02 ± 0.23
	β_F	6475.176 ± 0.017	0.18 ± 0.01	4.54 ± 0.06
	β_A	6491.805 ± 0.007	0.36 ± 0.01	1.93 ± 0.02
	β_B	6490.862 ± 0.031	0.07 ± 0.01	1.82 ± 0.15
MnO	β_C	6489.569 ± 0.041	0.24 ± 0.01	3.79 ± 0.08
	β_E	6483.224 ± 0.324	0.07 ± 0.01	10.95 ± 1.08
	β_F	6476.014 ± 0.028	0.26 ± 0.01	7.56 ± 0.09
	β_A	6491.786 ± 0.017	0.27 ± 0.01	1.86 ± 0.07
	β_B	6492.401 ± 0.012	0.12 ± 0.01	1.26 ± 0.04
Mn(CH$_3$COO)$_2$	β_C	6489.956 ± 0.032	0.26 ± 0.01	3.44 ± 0.07
	β_D	6486.555 ± 0.270	0.08 ± 0.01	9.82 ± 0.48
	β_E	6480.108 ± 0.173	0.01 ± 0.01	1.53 ± 0.62
	β_F	6475.827 ± 0.025	0.27 ± 0.01	7.01 ± 0.06
	β_A	6492.317 ± 0.011	0.26 ± 0.01	1.80 ± 0.03
	β_B	6491.155 ± 0.024	0.14 ± 0.01	1.86 ± 0.07
MnF$_3$	β_C	6489.808 ± 0.076	0.18 ± 0.01	3.09 ± 0.10
	β_D	6488.308 ± 0.079	0.10 ± 0.01	5.32 ± 0.43
	β_E	66481.525 ± 0.265	0.16 ± 0.01	13.38 ± 0.45
	β_F	6475.303 ± 0.036	0.16 ± 0.01	6.07 ± 0.14
	β_A	6491.606 ± 0.007	0.39 ± 0.01	1.93 ± 0.02
	β_B	6490.075 ± 0.019	0.11 ± 0.01	1.75 ± 0.07
Mn$_2$O$_3$	β_C	6488.457 ± 0.031	0.13 ± 0.01	3.52 ± 0.10

<div align="center">Continued on next page</div>

Table 7.3 – continued from previous page

compound	component	E_i (eV)	I_i	L_i (eV)
	β_D	6484.081 ± 0.166	0.20 ± 0.01	13.09 ± 0.26
	β_F	6475.515 ± 0.039	0.18 ± 0.01	8.01 ± 0.11
MnO$_2$	β_A	6491.156 ± 0.015	0.30 ± 0.01	2.02 ± 0.03
	β_B	6489.838 ± 0.027	0.21 ± 0.01	2.38 ± 0.11
	β_C	6487.679 ± 0.085	0.15 ± 0.01	4.04 ± 0.19
	β_E	6482.892 ± 0.260	0.17 ± 0.01	11.20 ± 0.53
	β_F	6474.806 ± 0.097	0.17 ± 0.01	10.23 ± 0.24
Mn(V)	β_A	6490.159 ± 0.012	0.31 ± 0.01	2.51 ± 0.03
	β_B	6489.313 ± 0.029	0.15 ± 0.01	1.75 ± 0.16
	β_C	6488.001 ± 0.034	0.19 ± 0.01	2.75 ± 0.09
	β_D	6483.969 ± 0.065	0.22 ± 0.01	8.96 ± 0.22
	β_E	6479.023 ± 0.099	0.01 ± 0.01	$1.53, \pm 0.39$
	β_F	6475.127 ± 0.122	0.12 ± 0.01	11.52 ± 0.20
KMnO$_4$	β_A	6489.465 ± 0.053	0.43 ± 0.05	2.70 ± 0.08
	β_B	6488.220 ± 0.144	0.27 ± 0.05	3.55 ± 0.13
	β_C	6484.622 ± 0.260	0.01 ± 0.01	2.63 ± 0.10
	β_F	6479.334 ± 0.145	0.29 ± 0.01	17.09 ± 0.29

7.5. Line width and asymmetry factor

The total line width and asymmetry factors of Kα_1, Kα_2, and Kβ_{13} lines are given in Tab. 7.4. As a simple parameter indicating approximately the asymmetry of the line shape, the asymmetry factor is used being the ratio of left (low-energy side) and right half-width half-maximum (HWHM). However, given the complexity of the line shape, a single parameter does not describe the complexity of the line shape, in particular, when various satellite or line splitting lead to a significant asymmetry (see Chap. 8).

From Tab. 7.4 it is immediately seen the influence of the correlation with the outer shells and the chemical environment. The calculated level widths without such additional interactions are 1.16, 0.34, and 0.32 eV for the $1s_{\frac{1}{2}}$, $2p_{\frac{1}{2}}$, and $2p_{\frac{3}{2}}$ atomic states [11]. Hence, the line widths of the Kα_2 and Kα_1 X-ray lines should be 1.50 and 1.48 eV, which is more than a factor of two smaller than measured for various compounds.

7.6. $I_{K\alpha_2}/I_{K\alpha_1}$ intensity ratio

For the determination of the relative intensity of the two fine structure components the various components must be attributed to one of the lines which maybe not unique. It is assumed that satellite production due to multiple vacancy production is similar. Some of the components may not be assignable, in particular, if they are used to fit intensity in between the main components (see *e.g.* KMnO$_4$ Kα (Fig. 7.4.)).

Therefore, the intensity ratio $I_{K\alpha_2}/I_{K\alpha_1}$ given is only an approximation. The small error accounts to the statistical uncertainty of the fit only and ignores the ambiguities of the choice of the components (Tab. 7.2). This problem has been discussed in detail already by Hölzer et al. [8]. Other combinations may be extracted from the values given in Table 7.2.

Table 7.4. : Magnetic moment, total width (FWHM) and asymmetry factor of the $K\alpha_1$, $K\alpha_2$, and $K\beta_{1,3}$ complexes. The asymmetry factor is given by the ratio left-to-right of the widths at half maximum. FWHM and asymmetry errors are within 50 meV.

	magnetic moment [27] μ/μ_B	FWHM / eV			asymmetry factor		
		$K\alpha_1$	$K\alpha_2$	$K\beta_{1,3}$	$K\alpha_1$	$K\alpha_2$	$K\beta_{1,3}$
Mn (metal) [8]		2.47	2.92	2.97	1.49	1.17	
Mn (metal)	1.5	2.40	2.93	2.86	1.63	1.22	1.57
Mn(0)	0.0	1.81	2.89	3.65	1.01	0.96	0.95
Mn(I)	0.0	1.71	2.59	3.11	1.01	0.84	1.18
MnF_2	6.0	3.63	3.88	2.47	2.99	1.42	1.58
MnO	5.9	3.57	3.80	2.97	2.51	1.40	1.77
$Mn(CH_3COO)_2$	5.7	3.47	3.75	2.98	2.65	1.36	2.12
MnF_3	5.0	3.43	3.66	3.95	1.10	1.28	2.72
Mn_2O_3	5.3	3.46	3.59	3.11	2.74	1.27	1.97
MnO_2	3.9	2.83	3.24	3.56	1.95	1.07	2.03
Mn(V) complex	0.0	1.92	2.61	3.76	0.98	0.97	1.27
$KMnO_4$	0.0	1.83	2.70	3.63	1.01	0.91	1.37

8. DISCUSSION

8.1. Ordering by nominal ionisation number

The measured peak-energy shifts for the Kα_1, Kα_2, and K$\beta_{1,3}$ transitions relative to metal (see Tab. 7.1) are compared to previous experimental results in Fig. 8.1. The horizontal axis is adapted to the nominal ionisation number of the manganese atom for the corresponding compound (Mn(0) to Mn(VII) from left to right). Most of the previous results for the Kα_1 and Kα_2 energies are in reasonable agreement with our data. Error estimates, however, are given only by Sanner [64] and Meisel et al. [65] (± 0.11 eV each). Also for the selection of previous K$\beta_{1,3}$ measurements mostly reasonable agreement is found with this experiment. Also here, not for all measurement an error estimate could found in the literature. The smallest errors are quoted for a recent measurement [66] with errors between 50 and 90 meV are given for the K$\beta_{1,3}$ energies.

For the Kα_1 transition, in general, a decrease of the peak energy with increasing formal ionisation number is observed, where the total change in energy is almost 1.7 eV. Metallic manganese was placed in this sequence arbitrarily to fit into the trend of the Kα_1 without deeper physical meaning. In the case of Kα_2, peak energies vary less within about 0.8 eV. Except for MnO, all peak shifts are negative relative to the metallic state in contrast to Kα_1, where the peak energies of ionic compounds typically exceed the metal value. For the K$\beta_{1,3}$ transition, the results for the energies of the various experiments span a range of about ± 1.5 eV. Such a behaviour is expected from the stronger dependence on the chemical environment of the stronger ($3p$,$3d$) shell interaction.

The metal state plays a particular role because of its complicated crystal structure, which contains 58 atoms per unit cell at four non-equivalent sites [25]. In the X-ray measurements reported here, of course, the resulting spectrum is a superposition of X-ray emission from all sites. According to the free electron density [27], we adopt the formal ionization number to II which is consistent with a determination of the valence structure in Mn metal finding 4.84 ± 0.18 for the number of $3d$ electrons [67]. However, except for the Kα_2 line and neglecting the details of the line shape, a ionisation number around 4 seems to more appropriate.

Deviating from the general dependence on the ionisation number are for all three transitions the compounds containing Mn(0) and Mn(I) atoms, which have peak energies shifts comparable to the one of KMnO$_4$. An explanation for this behaviour will be discussed in Chap. 8.5.

The change for the Kα_1 seems to be more distinct than the one for Kα_2, i. e. the fine-structure splitting itself would show a dependence on the compound. However, as can be seen from Fig. 7.2, a doublet-like splitting is observed for the MnF$_2$ of the Kα_1 line. Such a splitting has been reported earlier [30] and was traced back to core-hole $3d$-shell coupling [10, 28]. From this experiment, there is direct evidence for such a splitting also for other compounds with manganese being in formal ionisation state II (MnO and Mn(CH$_3$COO)$_2$). Therefore, identifying the peak energy with a peak shift could be misleading and a closer view to the line shape is necessary before drawing conclusions (see Chap. 8.4).
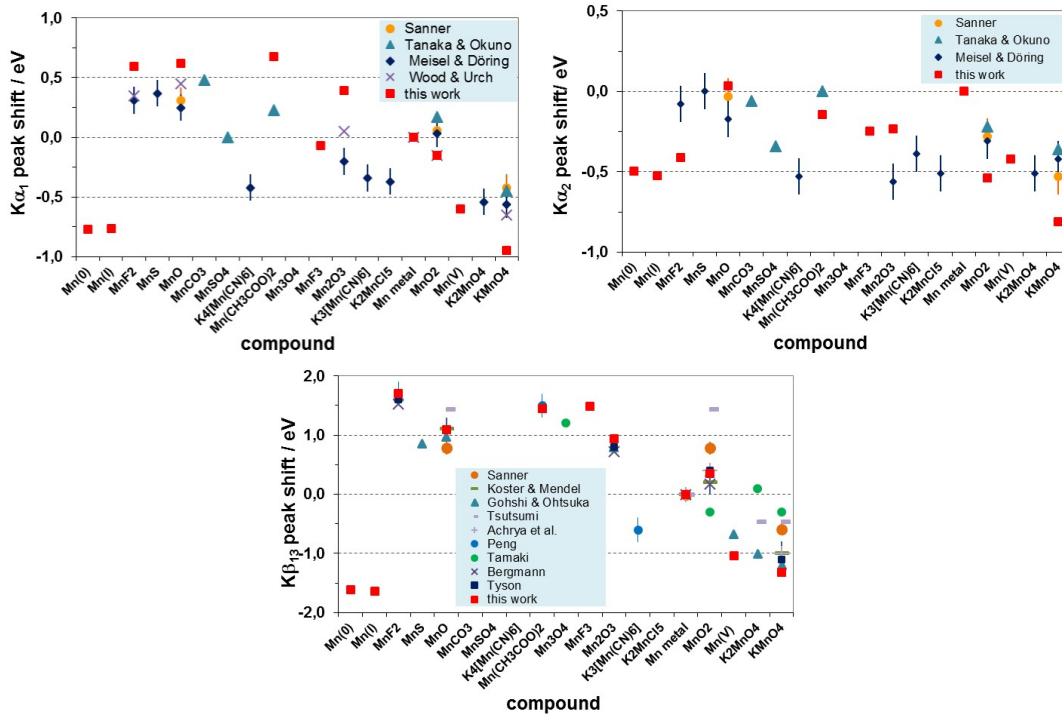
Fig. 8.1. : Comparison of measured peak-energy shift of the $K\alpha_1$, $K\alpha_2$, and $K\beta_{13}$ complexes relative to the transition energy of Mn metal. Error bars of this experiment are within symbol size. Compounds are arranged according nominal oxidation number from left (0) to right (VII). Previous $K\alpha$ data sets are given by Tanaka [68] (MnO_2, $KMnO_4$), Sanner [64] (MnO, MnO_2, $KMnO_4$), and Meisel [65] (MnF_2, MnS, MnO, $K_4Mn(CN)_6$, Mn_2O_3, $K_3Mn(CN)_6$, MnO_2, K_2MnO_4, $KMnO_4$). For the numerous $K\beta_{13}$ data, as examples results are shown of Sanner [64] (MnO, MnO_2, $KMnO_4$), Koster and Mendel [69] (MnO, MnO_2, $KMnO_4$), Gohshi and Ohtsuka [70] (MnF_2, MnS, MnO, Mn_2O_3, MnO_2, K_2MnO_4, $KMnO_4$), Tsutsumi et al. [71] (MnO, MnO_2, K_2MnO_4, $KMnO_4$), Acharya et al. [72](MnO_2, $KMnO_4$), Peng [73] (MnF_2, $K_3Mn(CN)_6$), Tamaki [74] (MnO_2, Mn_3O_4, $KMnO_4$), Bergmann [75] (MnF_2, Mn_2O_3, MnO_2), and Tyson [66] (MnF_2, MnO, Mn_2O_3, MnO_2, $KMnO_4$).

To be consistent, also in these Mn(II) compounds the peak energies (Tab. 7.1) and asymmetries (Tab. 7.4) are always given relative to the absolute maximum of the particular line for a first overview. It is not always obvious which method has been applied in the previous measurements to determine the peak energy or whether a $K\alpha_1$ splitting could be resolved at all. Therefore, the comparison of the energies of the various measurements should be regarded as an assessment of calibration standards. A refined treatment of the energy is possible by a tentative assignment of individual components of the fit (see Chap. 8.4).

In Fig. 8.2, peak widths are displayed for all compounds measured in this experiment. Comparing the measured line widths (FWHM) with existing data, as given for a few examples in Tab. 7.4, deviations found are at maximum 20%.

Inspecting at first the $K\alpha$ transition, a decrease of the line width of both fine-structure components is observed with increasing nominal ionisation number. Again, the results for the compounds with Mn(0) and Mn(I) atoms are similar to the ones for $KMnO_4$ (see Chap. 8.5).

The widths of the $K\beta_{1,3}$ transition show no significant dependence on the ionisation number, but scatter by about $\pm 0.5\,eV$ around 3.5 eV. The result for MnF_2 deviates to lower values which, however, becomes obvious by a look at the spectrum itself (Fig. 7.5). The onset of the pronounced shoulder at the long-wavelength side starts below FWHM. Very similar shapes are observed for MnO and $Mn(CH_3COO)_2$ (both containing Mn(II) atoms), but the

slightly higher onset enlarges the result for the line width by about $0.5\,\mathrm{eV}$. Consequently, FWHM alone is insufficient for the detailed description of the line shape. The onset of the shoulder is clearly revealed by the good resolution achieved in this experiment which obscures a comparison with other measurements with less known or even unknown resolution conditions.

The visibility of the shoulder at the low-energy tail of the $K\beta_{1,3}$ line demonstrate the importance of the knowledge of the resolution function. High-resolution measurements like the one of [73],[76], or this work reveal details usually inaccessible in case of moderate resolution [77].
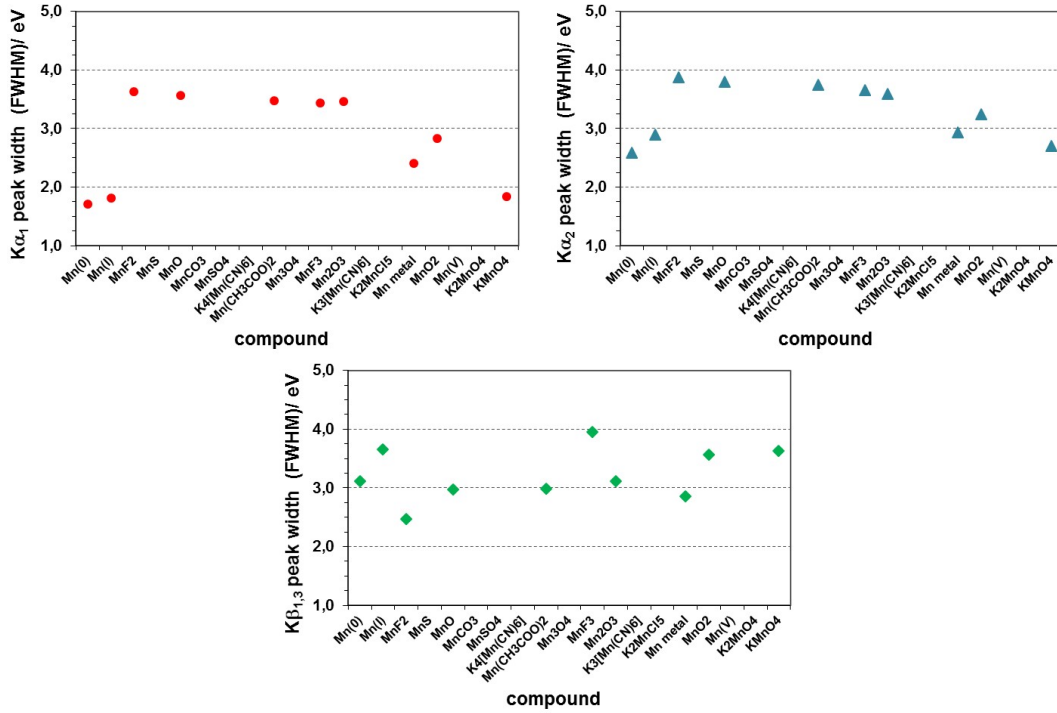
Fig. 8.2. : Measured line widths (FWHM) of the $K\alpha_1$, $K\alpha_2$, and $K\beta_{1,3}$ transitions. Uncertainty values (see Tab. 7.4) are covered by the symbol size.

8.2. Ordering by $3d$-shell electrons

It was found, *e. g.* from magnetic moment measurements, at least for Mn compounds having ionic character, that angular momenta in the $3d$ shell are usually quenched (i.e. orbital angular momenta do not contribute to the total spin) [10]. Hence, magnetic properties are determined by the total spin of the $3d$ shell electrons and its interaction of various sites in the elementary cell defining the crystal structure. The substructure of the $K\alpha_1$ and $K\alpha_2$ lines as well as of the $K\beta$ complex are assumed to reflect that spin state of the valence shell.

For the fine-structure components $K\alpha_1$ and $K\alpha_2$, the spin state manifests in the line width. As the spin-orbit interaction dominates, the overall appearance remains always the fine-structure doublet. The $K\alpha_1$ and $K\alpha_2$ splitting caused by the $(2p, 3d)$ exchange interaction cannot be resolved as it is of the order of the natural line width or less.

In contrast, in the case of the $K\beta$ the $(3p, 3d)$ exchange interaction it directly visible from a significant splitting of a $K\beta_{1,3}$ diagram line. The most prominent contributions are the

remnant of the $K\beta_{1,3}$ transition and the so called $K\beta'$ line being separated by about 17 eV. The dominant part of the splitting here is the exchange interaction, where the spin-orbit part is to small to be resolved.

In both cases, $K\alpha$ and $K\beta$, the splitting does not affect the centre of gravity of the line. Therefore, any splitting goes along with an energy shift. As the exchange interaction depends on the total spin of the $3d$ shell, which is related to the number of unpaired n_{unp} electrons, also the energy shift dependence on n_{unp} should reflect the spin status. Such a trend, as already described by Meisel et al. [65], is confirmed in this experiment. The peak shifts are shown relative to the peak energy of the Mn metal in Fig. 8.3.
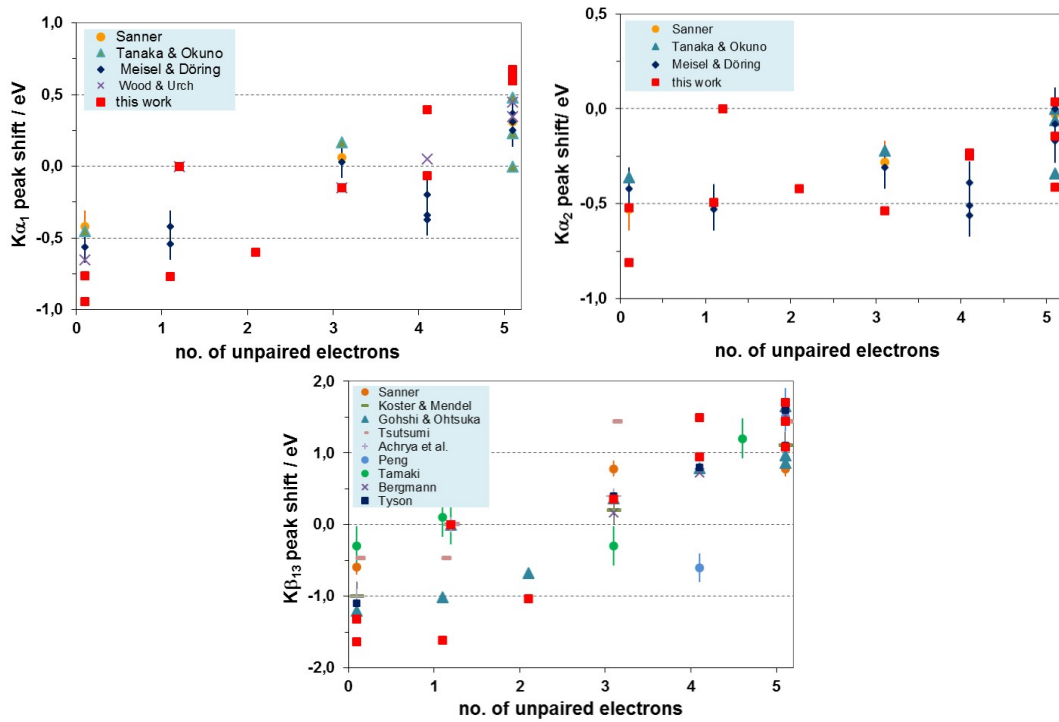
Fig. 8.3. : $K\alpha_1$, $K\alpha_2$, and $K\beta_{1,3}$ peak energy shifts as a function of the number of unpaired electrons relative to metallic manganese.

Describing the gross behaviour by a linear fit to the data of this experiment, the energy dependence on the ionisation number of the $K\alpha_1$ component (slope $0.31/n_{unp}$) was found to be about three times larger than the one of $K\alpha_2$ (slope $0.10/n_{unp}$), *i. e.* the energy splitting of the $K\alpha$ fine structure itself shows an energy dependence. The slope of the $K\beta_{1,3}$ energy dependence exceeds the one for the $K\alpha_1$ by another factor of two (slope $0.66/n_{unp}$). The value for manganese metal has not been included in the straight line fit (see below).

For metallic manganese, the estimate for number of unpaired $3d$ electrons n_{unp} from the magnetic moments at the individual sites fails. It results in $n_{unp} = 1.1 - 1.5$ depending on the model [25], which obviously does not follow the systematics observed for the compounds. Inspecting Fig. 8.3 suggests rather values $n_{unp} \approx 4$ without claiming this to be a mandatory physical interpretation.

8.3. Line shape

8.3.1. Kα doublet

Noteworthy, that already an unbiased fit to the line shape provides evidence for the splitting as predicted for the exchange interaction [28, 31]. *E. g.* in the case of a $3d^5$ valence shell and ignoring mixing and multiple vacancies, one expects for the Kα_1 and Kα_2 a splitting into 4 and 2 components with relative population corresponding to the statistical weight of 15:11:7:3 and 6:4, respectively.

Additional components contributing to the line shape may originate from satellite lines owing to multiple vacancy production. As already found in the analysis of Deutsch et al. [7] for copper, and Hölzer [8] for other transition metals, a significant contribution from an additional $3p$ vacancy can be excluded. Such a contribution would manifest as a component at the high energy tail of the Kα_1 line, which is not observed within the accuracy of this experiment.

More likely is the occurance of an additional $3d$ vacancy because of a much lower binding energy (Fig. 1.4), which enhances the probability for a shake-off process. One component in the low-energy tail was tentatively attributed to such an additional $3d$ vacancy in the analyses of the transition metal spectra [7, 8]. In this analysis, also a broadening or shoulder of the Kα_1 low-energy tail is found in all cases except for the case KMnO$_4$. However, a discrimination between additional vacancy and a component originating from splitting caused by the exchange interaction is not feasible without further theoretical input. The only evidence, that the component is due to splitting comes from the fact, that it is clearly absent in the case of KMnO$_4$ and difficult to attribute for the compounds with Mn(0) and Mn(I) configurations (Figs. 7.3 and 7.4).

8.3.2. Kβ complex

As mentioned above, for the K$\beta_{1,3}$ line numerous studies exist on the influence of the chemical environment [77], in particular for organic compounds because of the biological importance of manganese. A detailed study for ionic compounds of manganese is given by [76]. The measurements presented here were performed to make available Kα and Kβ spectra taken at identical conditions (except Bragg angle angle and the corresponding focal length) to exclude systematic effects added to the measurement.

The expected strong dependence is observed of the line shape on the compound composition in good agreement with previous measurements. For the K$\beta_{1,3}$ itself, three components are needed in the phenomenological fit (Figs. 7.5 and 7.6 and Tab. 7.3). The low-energy satellite structure Kβ' requires in general only one component in the fit. One or two broad components are necessary to consider the intensity in the energy range between K$\beta_{1,3}$ and Kβ'.

The intensity of the Kβ' component decreases as expected for increasing ionisation number, *i. e.* decreasing number of unpaired electrons for high-spin states. Also the decrease of the Kβ' - K$\beta_{1,3}$ splitting with decreasing n_{unp} shows the expected behaviour [10, 28]. For Mn(0) and Mn(I), the spectra are similar to the case Mn(VII), *i. e.* show the typical properties of a low-spin configuration.

For Mn(II) compounds, the asymmetry of the low-energy tail appears not only as a broadening but rather as a pronounced shoulder. The shoulder is due to the spin-flip component (^{4}D)^{5}P of the $(3p, 3d)$ coupling [28, 73] (see Chap. 1.6). In the fit , this requires

a component at about 2.5 eV below the K$\beta_{1,3}$ peak energy. Therefore, as mentioned above, FWHM value is does not reflect properly the total line width.

8.4. Theoretical approach to the energy shift

Calculation of the observed K X-ray shifts and line shapes for Mn compounds presents a challenging exercise. The correct description of the sharing of Mn $3d$ electrons and the valence electrons of partner atoms as well as and the non-localised $4s$ electrons requires a theoretical understanding of combining inner shell multiplets with mixing of molecular wave functions as well as the coupling of the core holes with the various $3d$ shell configurations.

Thus, even in a more modest approach, where the centres of gravity of the individual transitions Kα_1, Kα_2, or K$\beta_{1,3}$ should be reproduced, faces at least the problems to attribute fit components to a transition. Tentatively, for the comparison with the calculations outlined below, the line energies were defined as centre of gravity of the up to 4 components and up to two components for the Kα_1 and Kα_2 transition, respectively. For the K$\beta_{1,3}$, all components $(1-3)$ below the main peak are considered. In this way, the splitting due to the exchange interaction is taken approximately into account.

As a first attempt, a multi-configuration Dirac-Fock and an average-energy Dirac-Fock code was used [78] to calculate the K X-ray energies for varying $3d$ occupancy in the Mn atom. Here, it is assumed that an effective number of $3d$ electrons can be associated with the Mn oxidation state. However, such a free ion approximation though providing a relativistic treatment of hole states proved to be inadequate because the electron density contributions at the $3d$ level from the valence electrons of the ligands are neglected. This approximation leads to a significant overestimation of energy shifts by up to 9 eV. Also, the calculated Kα fine structure splitting in manganese is found to be 11.9 eV [29], whereas the experimental result is 11.1 eV [8, 29].

The contributions from the ligand atoms and the sharing of Mn $3d$ electrons with the neighbouring atoms are incorporated in molecular orbital calculations, which, however do not account for the multiplet splitting [10]. Therefore, a calculation was asked for within a relativistic density functional approach [79]. The code CLUSTER, partly developed at the University of Kassel [80], was used with which the electronic structure of the hole states $1s^{-1}$ and $2p^{-1}$ was calculated for a selection of Mn compounds (Tab. 8.1). Aim of this study was to investigate whether the gross features can be reproduced, *i. e.* essentially the change of the electron-density distributions causing the Kα_1 and Kα_2 energy shifts.

Table 8.1. : Nearest atom neighbour coordinates (F or O) used in the RLDA calculations with the CLUSTER code (in 10^{-10} m.). The manganese atom is placed in the origin (0,0,0).

	(x,y,z)	(x,y,z)	(x,y,z)	(x,y,z)	(x,y,z)	(x,y,z)	
MnF$_2$	(-0.95,-0.95,-1.66)	(0.95,0.95,-1.66)	(1.49,-1.49,0)	(-1.49,1.49,0)	(-0.95,-0.95,1.66)	(0.95,0.95,1.66)	[81]
MnO	(2.22,0,0)	(-2.22,0,0)	(0,2.22,0)	(0,-2.22,0)	(0,0,2.22)	(0,0,-2.22)	[82]
Mn(CH$_3$COO)$_2$ I	(0.53,1.05,1.86)	(-0.53,-1.05,-1.86)	(-1.31,-0.94,1.48)	(1.31,0.94,-1.48)	(-1.53,1.49,-0.37)	(1.53,-1.49,0.37)	[83]
II	(0.12,1.57,-1.44)	(-1.32,-1.12,-1.35)	(-0.01,-1.60,1.56)	(1.98,-0.57,-0.74)	(-1.85,0.39,1.18)	(1.00,1.36,1.41)	
MnF$_3$	(0,0,2.09)	(0,0,-2.09)	(0,1.91,0)	(0,-1.91,0)	(1.79,0,0)	(-1.79,0,0)	[84]
Mn$_2$O$_3$ I	(1.25,-0.80,1.41)	(1.36,1.22,-0.80)	(-0.76,1.39,1.17)	(-1.25,0.80,-1.41)	(-1.36,-1.22,0.80)	(0.76,-1.39,-1.17)	[85]
II	(1.26,1.42,-0.80)	(1.36,-0.80,1.21)	(-0.76,1.17,1.37)	(-1.26,-1.42,0.80)	(-1.36,0.80,-1.21)	(0.76,-1.17,-1.37)	[86]
MnO$_2$	(-0.86,-0.86,-1.44)	(0.86,0.86,-1.44)	(1.34,-1.34,0)	(-1.34,1.34,0)	(-0.86,-0.86,1.44)	(0.86,0.86,1.44)	[87]
KMnO$_4$	(-1.31,-0.76,-0.54)	(1.31,-0.76,-0.54)	(0,1.52,-0.54)	(0,0,1.61)	—	—	[88]

For the examples chosen for the calculation, the nearest neighbours of the metal ion are arranged in Tab. 8.1. These selected Mn compounds have octahedral or tetrahedral geometry and each is modelled as a cluster with a Mn atom embedded in six (MnF$_2$, MnO,

$Mn(CH_3COO)_2$, MnF_3, Mn_2O_3, MnO_2) or four ligand atoms ($KMnO_4$), where only O and F atoms are considered as neighbours (see Tab. 8.1). The vectors of these atoms with respect to the manganese atom —which we place at the origin— have been extracted from the available data on the electronic structure of the respective manganese compounds. For $Mn(CH_3COO)_2$ and Mn_2O_3, the two different (equally frequent) Mn sites (I and II) are calculated separately.

All results for the energy shifts calculations were related to the case $KMnO_4$ with tetrahedral geometry (Fig. 8.4 and Tab. 8.2) because the calculation of precise absolute energies is beyond such approaches. The results are given again with respect to the number of unpaired electrons n_{unp} and relative to the $KMnO_4$. The theoretical treatment of Mn metal is beyond the ability of the CLUSTER code.
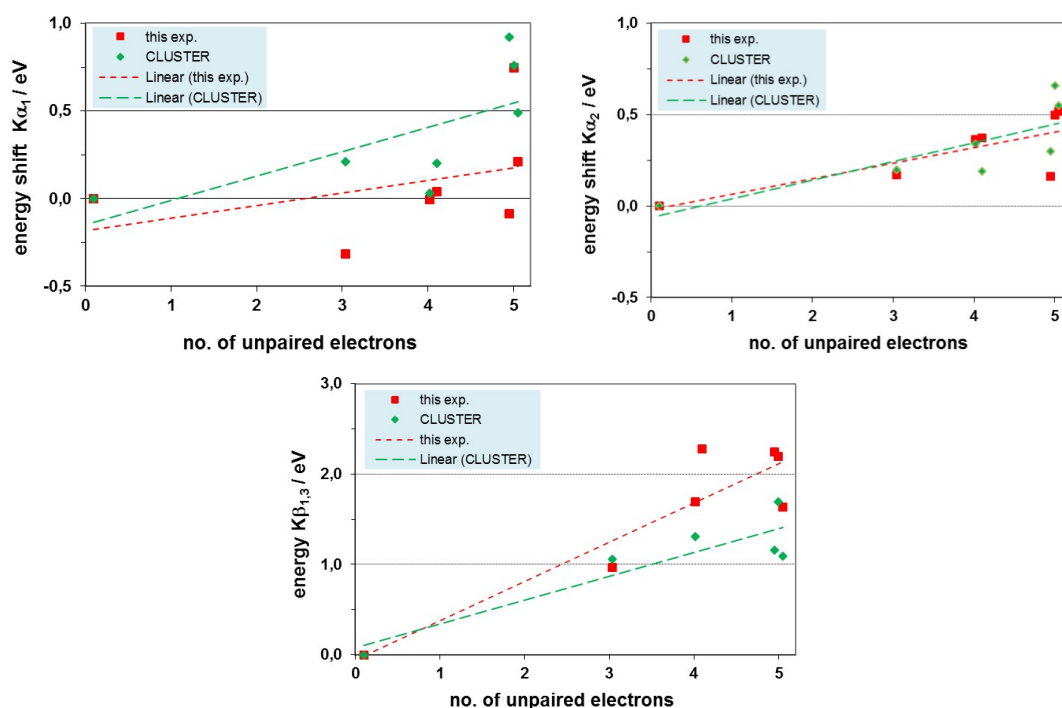
Fig. 8.4. : Comparison of measured and calculated peak energies of the Mn $K\alpha_1$, $K\alpha_2$, and $K\beta_{1,3}$ transitions. Data () are compared to the results obtained by the molecule code CLUSTER () [79]. The slope parameters of the linear fit are for Mn $K\alpha_1$, $K\alpha_2$, and $K\beta_{1,3}$ $0.072/n_{unp}$, $0.085/n_{unp}$, and $0.43/n_{unp}$ for the data and $0.14/n_{unp}$, $0.10/n_{unp}$, and $0.27/n_{unp}$ for the calculated energy shifts.

In view of the crude approximation of the geometry with only 6 or 4 nearest neighbours, reproducing the general trend constitutes a reasonable agreements. In particular, the proportionality to the number of unpaired electrons is recovered. Both in experiment and calculation the variation of the energy with electronegativity of the ligand seems to be more important than the nominal ionisation number (see, *e. g.* MnF_2, MnO, $Mn(CH_3COO)_2$ at $n_{unp} = 5$ corresponding to Mn(II)). Such a dispersion for Mn(II) compounds has been reported also by [76].

Finally, one can state that the trend coincides generally spoken between experiment and theoretical calculations for the $K\alpha_2$ transition. For the $K\alpha_1$ transition, the trend is slightly overestimated by the calculation, where it is underestimated for the $K\beta_{1,3}$ line. The interpretation is such that in the case of the $2p_{1/2}$ to $1s_{1/2}$ transition the description is quite realistic because both orbitals in the relativistic description are spherical symmetric. In the code due to the density functional description these orbitals are always averaged out in the

Table 8.2. : Spectral line shifts ΔE for the manganese Kα_1, Kα_2, and Kβ transitions as obtained from RLDA calculations compared to the experimental results. Experimental values are calculated as centre of gravity from the individual fit components. Energy shifts are given relative the compound KMnO$_4$.

| | ΔE / eV | | | | | |
| | Kα_1 | | Kα_2 | | K$\beta_{1,3}$ | |
	RLDA	exp.	RLDA	exp.	RLDA	exp.
MnF$_2$	0.92	-0.09	0.30	0.16	1.16	2.25
MnO	0.49	0.21	0.55	0.52	1.06	1.64
Mn(CH$_3$COO)$_2$	0.76[a]	0.75	0.66[a]	0.50	1.69[a]	2.20
	0.39[b]		0.39[b]		1.22[b]	
MnF$_3$	0.20	0.04	0.19	0.37	—	2.28
Mn$_2$O$_3$	0.03[a]	0.00	0.34[a]	0.36	1.18[a]	1.60
	0.26[b]		0.04[b]		1.31[b]	
MnO$_2$	0.21	-0.32	0.20	0.17	1.06	0.97
KMnO$_4$	0	0	0	0	0	0

[a] cluster model I

[b] cluster model II

angle so that angle distribution does not take effect. Both orbitals the $p_{1/2}$ and the $p_{3/2}$ are then very similar to each other, so that the result for the $p_{3/2}$ to $s_{1/2}$ transition becomes comparable [79]. For the K$\beta_{1,3}$ transition, the stronger influence of the environment seems to be underestimated.

8.5. High-spin vs. low-spin states

In the overview plot (in Fig. 8.1) compounds are ordered about with increasing energy of the Kα_1 peak energy. It coincides with increasing nominal oxidation number except for Mn(0) and Mn(I). The same trend is observed for the K$\beta_{1,3}$ line. As a further systematics, the decrease of the line widths both for the Kα_1 and the K$\beta_{1,3}$ transition is observed (Fig. 8.2).

Mn(II) compounds show the typical pattern of high-spin states, where the $(np, 3d)$ exchange interaction causes a broadening proportional to the total $3d$ spin with the characteristic appearance of a strong Kβ' component. The Kα_1 line widths decrease and reach minimal values of ≤ 2 eV for Mn(V), Mn(I), and Mn(0), which indicates that in all these compounds the Mn $3d$ shell forms a low-spin state as narrow as for an empty $3d$ shell (Mn(VII)). Also for the Kα_2 lines, large widths are found for the cases Mn(II), Mn(III), and Mn(IV). The narrowest lines are observed in Mn(VII), Mn(V), Mn(I), and Mn(0), which corroborates the assumption of low spin.

As the spin state is correlated with the magnetic properties, the systematics with respect to the unpaired electrons should be similar for the magnetic moment as is demonstrated in Fig. 8.5. Comparing the Kα_1 and Kα_2 dependence on the number of unpaired electrons n_{unp} and the magnetic moments (Tab. 7.4), a similar trend is found. The agreement with a linear dependence is better in the case of the magnetic moment. This is not surprising, because the experimentally determined magnetic moment takes into account the true spin status better than n_{unp}, which reflects the nominal ionisation state.

As discussed earlier, FWHM is insufficient to charaterise the broadening of the K$\beta_{1,3}$
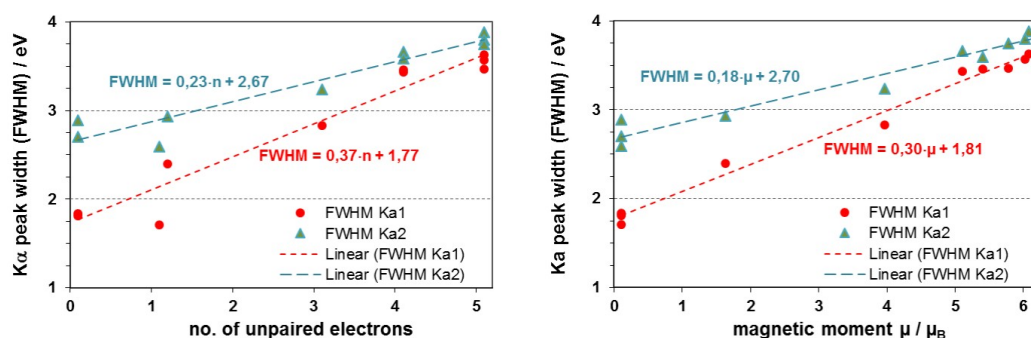
Fig. 8.5. : Dependence of the line widths of the $K\alpha_1$ and $K\alpha_2$ transitions on the number of unpaired electrons (top) and the magnetic moment of the atomic shell (bottom).

transition. The spin-state assignment of various compounds is seen more clearly by intensity and energy of the $K\beta'$ component. As the centre of gravity is assumed to be constant, the $K\beta_{1,3}$ energy must decrease with decreasing $K\beta'$ intensity. The largest energy splitting is found to be 17.1 eV for MnF_2 decreasing to 15.8 eV for MnO_2. For ionisation states Mn(VII), Mn(I), Mn(0) as well as for metal the $K\beta'$ peak is absorbed into the long $K\beta_{1,3}$ low energy tail. The appearance of any intensity in the $K\beta'$ region reveals that the interplay with ligands even in a very clean case like $KMnO_4$ exceeds the simplified picture.

9. SUMMARY

The experiment was originally motivated from the necessity to improve X-ray calibration standards to a precision of $10 - 20 \, \text{meV}$ in the few keV range which corresponds to the regime of characteristic X-radiation from the $3d$ transition metals. Such a goal is challenging in the case of fluorescence X-rays because most of the presence of incomplete electron shells cause a manifold of interactions. Consequently, the X-ray line shapes show the full complexity of a many-body problem. Precision measurements have been performed for the $3d$ transition metals by previous experiments at the above-mentioned level $\frac{\Delta E}{E} \leq 10^{-5}$ [8]. The results of these measurements are used here as absolute energy calibration.

It was one aim of the study to explore, which precision is achievable for the energy determination for compounds, where a strong variation of the line shape depending on the chemical environment is observed. Secondly, having available an ultimate resolution device, it would be interesting to see to which extent the underlying physical aspects of electron-electron and the core-hole $3d$-shell coupling could be recognizable by an unbiased analysis directly from the data, in particular for the Kα doublet.

As a case study, Kα and Kβ lines for various manganese compounds have been measured. Manganese is the element of the $3d$ transition metals with the $3d$ shell half filled which is regarded to be a particular stable configuration. The ability is demonstrated to determine and identify in detail characteristics of small chemical effects also from the Kα fluorescence radiation.

The measurements were performed with a Johann-type Bragg spectrometer using spherically bent crystals and set up at the Institut für Kernphysik at Forschungszentrum Jülich. The spectrometer achieves a resolution of $\approx 400 - 600 \, \text{meV}$ for energies of $5.9 - 6.4 \, \text{keV}$, which is close to the theoretical limit for a crystal bending radius of $3 \, \text{m}$. The spectrometer is equipped with a dedicated vacuum system which enables X-ray studies in an energy range from $2 - 15 \, \text{keV}$ without significant loss of performance.

The results show an overall agreement for line energies and line widths with previous studies. However, in a few cases deviations of up to 40% are observed, which maybe traced back to unclear experimental conditions like resolution functions. In some cases, experimental errors on energies could be reduced by up to one order of magnitude. The precise knowledge of the spectrometer response allows for a deconvolution of natural line width and response function. As a result, total line widths measured in this work show a trend to lower values compared to previous data (up to 20%).

The analysis of the line pattern reveals clearly the expected dominance of the core-hole $3d$-shell coupling for the broadening of the fine-structure components Kα_1 and Kα_2. The multiplet splitting caused by this interaction is already recognizable in an unbiased fit. This, together with the knowledge of the resolution, allows an unambiguous parametrisation of the line shape which may be confronted with the results of theoretical calculations. An assumption —based on experimental evidence and molecular orbit calculations— confirms directly, that in manganese the spin state of the $3d$ shell is not affected by creation and de-excitation of a core-hole.

As the line pattern is characteristic for specific groups of compounds it maybe used for material characterisation. This is already applied to widely for Kβ transitions, as their chemical effects are rather pronounced and differences are visible also in moderate resolution devices [10, 28, 75, 77]. As the precise deconvolution of the response allows for a parametrisation of the line shape, this method could benefit when applied to Kα pattern which are a factor of 8 more intense than the Kβ transition.

The spectrometer resolution in this experiment is dominated by the aberration owing to the rather small Bragg angle of $\approx 40°$. By applying a crystal providing Bragg angles at around $60°$ or even larger, such geometrical aberrations would decrease by a factor of at least two. Consequently, in such experiments the influence of the resolution function on the line shape almost vanishes, which enables the resolution of further details of Kα transitions approaching eventually a model-free parametrisation of the line shape.

A.   APPENDIX - CCD READOUT AND CLOCK SEQUENCING

In a CCD, the pixels are defined in horizontal direction by the electrode structures and in vertical direction by the channel stops (see Fig. 3.4). This format is used to create an image region and a store region of pixels, where the pixels in any row are linked by a common electrode structure but divided by the perpendicular channel stops. At the base of the store region, a line readout section or serial register is created. The electrodes in this register are arranged at right angles to, and to coincide with, the pixel structure of the rows in the store region. A single row of pixels may be transferred from the store region into the serial register, and then clocked, one pixel at a time, into the output node of the CCD.

For simplicity and convenience we call image area signals $I\varphi1$, $I\varphi2$, $I\varphi3$, storage area signals $S\varphi1$, $S\varphi2$, $S\varphi3$, and readout section signals φR ($reset$), $R\varphi1$, $R\varphi2$ and $R\varphi3$.

Image integration is the exposure time of the image section to the source, prior to transfer of the image section charge into the store section. Integration usually occurs with a single electrode energised, typically phase 2 in a 3-phase device. Once the desired integration time is achieved, a frame transfer operation is performed to transfer charge from the image section to the store section. The image and store section clocks are operated simultaneously. The crossover point occurs at 50% amplitude, with rise times of the order of 500 ns. Once this operation is complete (typically 20-30 ms) integration in the image section can begin again.

Fig. A.1 shows the actual clock pattern which is used in our experiments at Forschungszentrum Jülich. Number of clock cycles corresponds to the number of CCD rows. In our case, the CCD store region has 602 rows (Fig. 3.5). In image and storage section are normally 4 separate clocks, in both sections they have the same parameters (width and delays) and the same shape [47].
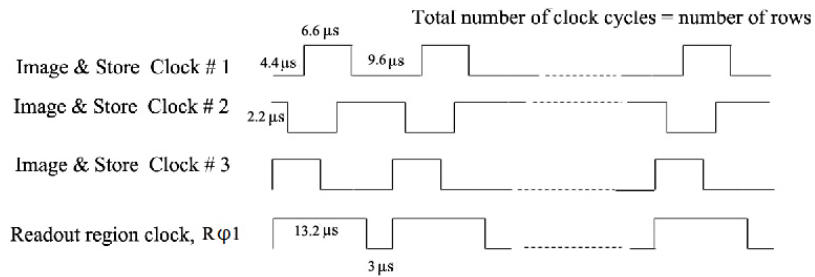
Fig. A.1.   : Frame transfer clock operation.

After frame transfer, the charge in the store section is transferred one row at a time into the serial register by performing a single cycle of the store section clocks only. The charge in the serial register is then transferred one pixel at a time onto the output node of the CCD. The rise and fall times of the reset and serial clocks are typically 100 ns. The crossover point can vary with CCD type. In some cases 100% clock overlap may be required to ensure complete charge transfer.
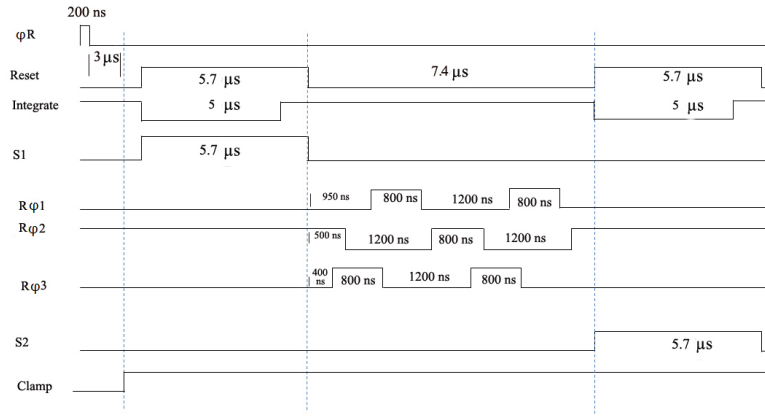
Fig. A.2. : CCD output clock pattern.

The read-out of charge from a single row of the store section of the CCD proceeds as follows. A single cycle of store section clocks transfers the charge from the final row of the store section into the serial register (Figure A.1). The following sequence, illustrated in Fig. A.2, is then repeated for each pixel in the serial register, equivalent to the number of pixels in the readout register (in our case 610) of the CCD.

The output node of the CCD is reset by pulsing the Reset pulse (φR) with a width of 200 ns. After 3 μs delay Reset, Integrate and S1 (sampling 1) pulses come together. They lead the readout region pulses, which are indicated as $R\varphi 1$, $R\varphi 2$ and $R\varphi 3$. These are 3 type of clocks which are essential for serial register readout. $R\varphi 3$ is set after 400 ns delay from the end of S1 pulse, then $R\varphi 2$ and $R\varphi 1$ are set.

Reset and Integrate pulses occur again after 7.4 μs delay from the time they appeared firstly. S2 (sampling 2) pulse comes in parallel with them and finally the Clamp pulse level goes down. The clamp pulse is up during the whole readout cycle. Widths and delays for all of the pulses are indicated in Figure A.2. Reset, integrate, clamp and sampling signals are used for CCD output amplification. The serial register clocks are cycled. On the falling edge of $R\varphi 3$, the charge is transferred from the end of the serial register onto the output node of the CCD. The CCD output charge level is then available for sampling.

Table A.1 summarises the CCD timing.

Table A.1. : CCD22 optimized operating voltages.

parameter	optimized value
Exposure time	10 s
One row (602 pixels) transfer from image to storage area	16.2 μs
Whole image area transfer	9.7 ms
One row transfer from storage area	16.2 μs
One pixel readout from serial/readout area	22 μs
One row readout from serial/readout area	13.420 ms
Whole store region transfer and readout	8.088 s
Entire CCD readout (602 x 610 pixels)	8.097 s

The final set of optimized CCD operating voltages is shown in Table A.2.

Table A.2. : Optimised voltages for CCD22 operation.

purpose voltage	indication	optimised value (V)
Image clock	$I\varphi 1$, $I\varphi 2$, $I\varphi 3$	3.5
Store clock	$S\varphi 1$, $S\varphi 2$, $S\varphi 3$	7.5
Serial clock	$R\varphi 1$, $R\varphi 2$, $R\varphi 3$	13
Reset pulse	φR,	9.5
First output drain	1 Vod	20
Second output drain	2 Vod	20
Third output drain	3 Vod	20
Output gate	Vog	1.9
Guard ring	Vgr	20
Substrate	Vss	1.5
input drain	Vid	16.8
reset drain	Vrd	15.3
common collector voltage	Vcc	5

B. APPENDIX - VOIGT PROFILE

The Voigt function is a widely used line profile for analysis in spectroscopy. The Lorentzian

$$L(x) = \frac{\Gamma}{2\pi} \cdot \frac{1}{(x - x_0)^2 + \frac{\Gamma^2}{4}} \tag{B.1}$$

represents the natural line shape of a spectral line and a typical detector response is parametrized as a Gaussian

$$G(x) = \frac{1}{\sqrt{2\pi}\sigma} \cdot e^{-\frac{(x-x_0)^2}{2\sigma^2}}, \tag{B.2}$$

where σ and Γ denote the standard deviation of the Gaussian and the width (FWHM) of the Lorentzian. x_0 denotes the center of the Gauss or Lorentz curve. The measured profile is given by the convolution $L \otimes G$ given by the Voigt integral

$$I(x) = \int_{-\infty}^{\infty} exp(-\xi^2) \frac{d\xi}{(a^2 + (v - \xi)^2)} \tag{B.3}$$

which is needed for the fitting function

$$V(x) = \frac{1}{2\sigma^2} \frac{A_v}{N} \cdot I(x) \tag{B.4}$$

and according to [89] can be represented using the complex error function $\omega(z \in \mathbb{C})$. Here A_v is the amplitude of the Voigt curve. The Voigt integral can be represented in the following way:

$$I(x) = \frac{\pi}{a} Re\,\omega(v + ia), \tag{B.5}$$

where $v = \frac{x - x_0}{\sqrt{2}\sigma}$ and $a = \frac{\Gamma}{2\sqrt{2}\sigma}$ and for $\omega(z)$ one has the following formulas:

$$\omega(z) = exp(-z^2) \cdot erfc(-iz), \tag{B.6}$$

$$erfc(z) = 1 - erf(z), \tag{B.7}$$

$$erf(z) = \frac{2}{\pi} \int_0^z exp(-t^2) dt. \tag{B.8}$$

C. APPENDIX - HIGH PERFORMANCE SCADA SYSTEM FOR MONITORING AND CONTROL OF CRYSTAL SPECTROMETER

C.1. Concepts of SCADA systems

The acronym SCADA denotes "Supervisory Control and Data Acquisition" [57]. The major function of SCADA is acquiring data from remote devices such as motors, valves, pumps, transmitters etc. and providing overall control remotely from a SCADA Host software platform. This provides process control locally so that these devices turn on and off at the right time, supporting the control strategy and a remote method of recording data and events (alarms) for monitoring these processes. SCADA Host platforms also provide functions for graphical displays, alarming, trending and storage of data. SCADA systems operate with coded signals over communication channels in order to provide control of remote equipment. The control component of the system can be combined with a data acquisition component by adding the use of coded signals over communication channels to acquire information about the status of the remote equipment for display or for recording functions.

Functions of SCADA systems are logically devided in two main groups: monitoring and control. Under monitoring those operations are considered, which observe, track and check the status of operations and activities of individual components or applications and devices of a set-up. They provide a way to supervise the overall processes that are performed and ensure the reporting services to the system. In this way, personnel serving the set-up governed by SCADA system has information if all the processes are running correctly and if some hardware or software problems took place during the operation. Generally, under monitoring inactive operations are considered, for instance device check-ups and status reports. It does not consider any kind of motion, only the supervision.

Control function is another feature of SCADA systems. It implies the active operations which are connected to action. This means turning hardware components on and off, activating the switches, controllers, motors, rotating the moving parts of the system, reacting on alarm situations by making decisions independently of human intervention, for example disabling/enabling the process or activating/deactivating the certain parts of the system.

Human-Machine Interface (HMI) realizes the control and monitoring functions of SCADA systems on the basis of the Graphical User Interface (GUI). It makes the management of a certain hardware set-up convenient and easy to use. User can perform the desirable actions by clicking the buttons located on HMI and monitor the results of actions which are directly registered and reflected on a screen.

C.2. Labview© -based SCADA system for the spectrometer

The crystal spectrometer which is used for the measurements done in the scope of current work is controlled and monitored by the Labview© -based SCADA system. The scheme of the hardware set-up used for monitoring and control purpose is shown on Fig. C.1. It consists of three main components:

- Personal Computer used for hosting the Labview© software, for monitoring the crystal and arm positions (angles) and for controlling the stepper motors;

- Stepper motors for the crystal and arm rotations and for controlling the focal distance.

- FieldPoint crate to collect and pass the results of monitoring (e.g. results of measurements done by FieldPoint modules) to Labview© in order to display them directly on a screen.

The list of parameters is shown in Table 4.3.
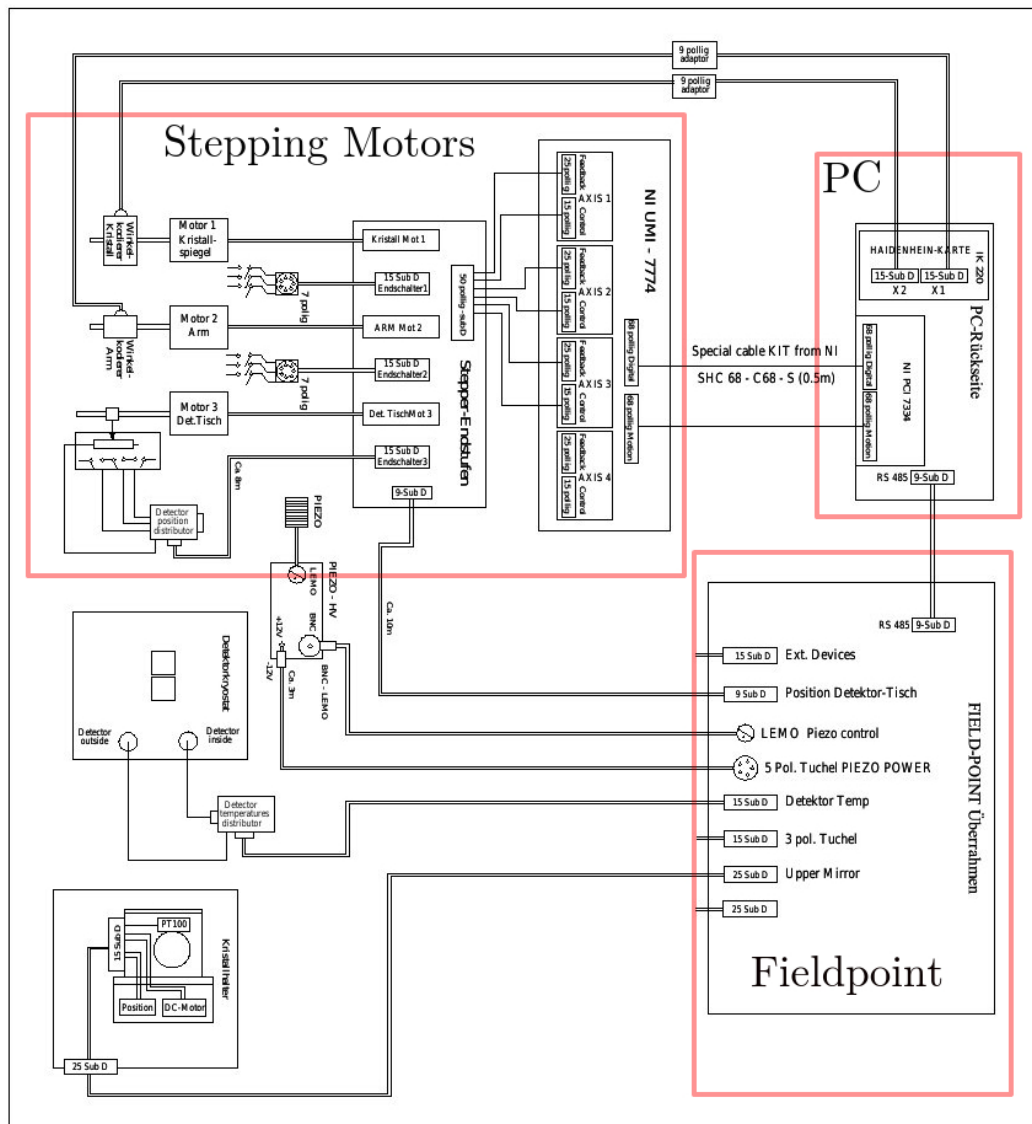
Fig. C.1. **:** Scheme of interconnection of hardware resources used for crystal spectrometer monitoring and control.

A personal computer hosts the spectrometer control panel which is projected in Labview©
in a form of the Human-Machine Interface, representing the graphical interface for the
user/operator. The idea of this interaction is to allow effective operation and control of the
machine from the human end, whilst the machine simultaneously feeds back information that
aids the operators' decision making process. The goal of the graphical user interface design
is to produce a user interface which makes it easy (self explanatory), efficient, and enjoyable
(user friendly), *i. e.* the operator has to provide minimal input while non-instructive outputs
are minimized. The human-machine interface of the Labview©-based system dedicated to
the IKP crystal spectrometer is shown on Figure C.2. The following sections describe the
software system, the controlled hardware and its electronic components in detail.
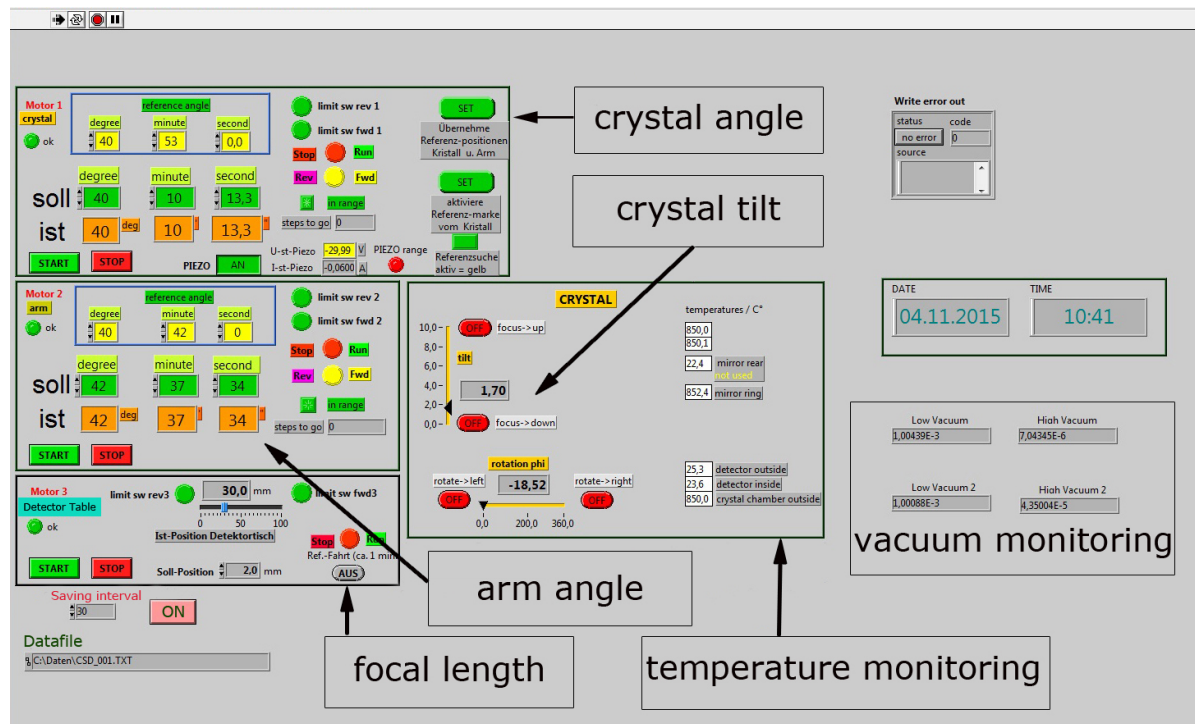
Fig. C.2. : The human-machine interface of Labview©-based monitoring and control system dedicated to
IKP spectrometer. The main parameters are crystal angle Θ_{CRY}, arm angle Θ_{ARM} and the focal
distance Y_{CD}, the crystal rotations along its vertical and horizontal axis (crystal tilt).

C.3. Spectrometer setting

C.3.1. Crystal angle Θ_{CRY}

The crystal angle is set by the rotation of the crystal around its vertical axis which defines the
orientation of the diffracting planes towards the detector. From Labview© this is done by
changing the crystal angle on Fig. C.2. The desired angle is usually given in "SOLL" field, in a
form of degrees, minutes and seconds. Text boxes indicated by "IST" label reflect the current
position of the crystal which is the actual crystal angle. When pressing the start button, crystal
starts to rotate from "IST" to "SOLL" position and as a result in both fields the same angles are
displayed.

Crystal rotations are physically done using the stepper motors. They are a kind of DC
electric motor that divides a full rotation into a number of equal steps. DC motors rotate

continuously when DC voltage is applied to their terminals. The stepper motor is known by its property to convert a train of input pulses (typically square wave pulses) into a precisely defined increment in the shaft position. Each pulse moves the shaft through a fixed angle. Stepper motors effectively have multiple "toothed" electromagnets arranged around a central gear-shaped piece of iron. The electromagnets are energized by an external driver circuit or a micro controller. To make the motor shaft turn, first, one electromagnet is given power, which magnetically attracts the gear's teeth. When the gear's teeth are aligned to the first electromagnet, they are slightly offset from the next electromagnet. This means that when the next electromagnet is turned on and the first is turned off, the gear rotates slightly to align with the next one. From there the process is repeated. Each of those rotations is called a "step", with an integer number of steps making a full rotation. In that way, the motor can be turned by a precise angle.

Crystal position is calculated by the help of angular encoder. It works with a special round-shaped disk located under the crystal support and divided in 36000 stripes. Crystal rotation is measured through this disk which is operated by the stepping motor. Rotation by the mentioned number of stripes corresponds to one complete rotation of the disk and correspondingly the crystal. In this way, counting the number of stripes as a result of rotation gives information about the rotation of the crystal.

The angular encoder is connected to the commercial counter board IK-220 [90]. The PC counter board connects two HEIDENHAIN measuring systems with sine wave output signals directly to personal computer, meaning that it serves two angular encoders: one from crystal and another from spectrometer arm. The interpolation electronics included on the IK-220 generates up to 200 counts per input signal period. This results in a finest measuring step of 1/200 th part of the signal period. As well as the interpolation and counting electronics, the IK-220 also has an interval counter which allows simultaneous storage of both counter values at predetermined distances. Storage of both counter values can be initiated independently for each axis (crystal and arm) by an external signal. Experiments have shown that with an optimised software routine it is possible to read two count values into Random Access Memory (RAM) in under $20\,\mu$s. Finally they are stored in 16 bit data registers, which are read out by Labview$^{\copyright}$-based program.

From angular encoders the IK-220 receives two incremental sine wave signals shifted by $90°$ to each other, the period of which corresponds to a particular linear or angular movement. According to which sine type signal comes first, the information about the direction of rotation is provided. The interpolation electronics convert one period of the input signals into 25 or 50 TTL signal periods. The TTL signals are fed to a counter internal circuit which is programmed to count one, two or four edges per TTL signal period (in our case four). This means that it's achieved to generate up to 200 counts for each period of the input signals. Considering the HEIDENHAIN counter card resolution, one complete $360°$ rotation corresponds to 36000x200=7200000 counts, resulting one count to be equal to 0.18" angular change of crystal position.

To convert the number of counts to millimeters with a linear measuring system:

$$Value\,[mm] = count * \frac{Signal\,period\,[mm]}{Evaluation\,*\,Interpolation} \tag{C.1}$$

In our measurements typically four fold evaluation and 50-fold interpolation is used. To convert the number of counts to degrees:

$$Value\,[°] = \frac{Count\,*\,360[°]}{Evaluation\,*\,Interpolation\,*\,Number\,of\,stripes} \tag{C.2}$$

Stepping motors are controlled from the NI PCI-7334 module [91], which is a commercial product of NATIONAL INSTRUMENTS company. This module is located in the PC serving the spectrometer and governed by Labview©-based system. The 7334 controllers are exclusively stepper motor controllers for PCI bus computers. They provide fully programmable motion control for up to four independent or coordinated axes of motion (in our case only three of them are used: for crystal angle, arm angle and detector position (focal distance)), with dedicated motion input/output for limit switches. When entering the new crystal position ("SOLL") the program calculates the difference between the current and desirable (new) position and calculates the number of counts and direction of rotation (clockwise (CW) or counter-clockwise (CCW)). This information is delivered to NI PCI 7334, which generates the corresponding signals as digital command outputs, which are spread out by 68-pin motion input/output connector. One important feature which is also used in our system is the trajectory generator, being an embedded component of the mentioned controller. Trajectory generator calculates the instantaneous position command that controls the acceleration and the velocity of the stepping motor while it moves the axis to its target position. Parameters are previously defined from software.

The NI PCI-7334 controller supports both major industry standards for stepper command signals - step and direction, or independent CW and CCW pulse outputs. The output configuration and signal polarity is programmed in advance as follows: when step and direction mode is configured, each commanded step (or microstep) produces a pulse on the step output. The direction output signal level indicates the command direction of motion, either forward or reverse. CW output is used for forward-commanded motion and CCW output for reverse-command one. In either case, the active polarity of both outputs are set either to active-low (inverting) or active-high (non-inverting). In our case it's done in a way that logic high corresponds to forward direction of motion.

The input information is converted to digital signals on Phase A and Phase B into 32 bit counter values. This provides two signals that are $90°$ out of phase. The leading phase, A or B, determines the direction of motion. The transition states of the relative signal phases provide distinct pulse edges that cause count up or down pulses in the direction determined by the leading phase (see Fig. C.3).
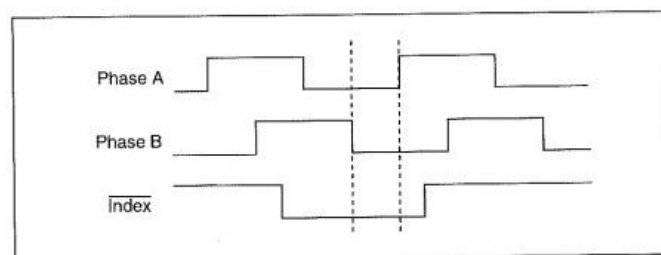
Fig. C.3. : NI PCI 7334 controller output signals for motion control [91].

The index signal is primarily used with the Find Index function. This function uses the number of counts per revolution ($360°$ rotation) to initiate a search move that locates the index position. When a valid index signal transition occurs during the Find Index sequence, the position of the Index signal is captured very accurately. This is used to establish a reference zero position for absolute position control. Reference position is usually marked when starting the measurements, meaning that, one knows the angle corresponding to this position. Later on, when necessary, this position can be activated using the upper mentioned method. Reference angles for crystal and spectrometer arm are considered in Labview©-based program and can be seen on Fig. C.2. After entering the reference angle, "SET" button

is used to transfer the value to the system and by clicking the "ACTIVATE" button crystal and arm are positioned back to their reference angles.

NI PCI-7334 controller receives the signals from limit switches which are used to define the range of movement for crystal and spectrometer arm. The limit switches are necessary to use, because if the stepper motors move the crystal and the arm beyond the pre-defined borders, there has to be a mechanism that stops them immediately.

The NI PCI-7334 controller is connected to NI UMI-7774 device [92] (see Fig. C.1), which is a set of standalone connectivity accessories designed to be used with 73xx series motion controllers for up to four axes of simultaneous or independent control. In our case three axes are used: for crystal angle, for arm angle and for the focal distance. The NI UMI-7774 connects third party stepper drives and/or feedback and digital input/output to National Instruments motion controllers. Each axis controller of NI UMI-7774 consists of two internal modules for feedback and control purposes. They are equipped with 25 and 15-pin connectors respectively. Control unit is designed to receive and transmit the control-type signals to stepper motors. These signals are number of steps and direction of rotation, originating from NI PCI-7334. Feedback unit is dedicated to work with limit switches used in spectrometer set-up and transfer the information coming from them to NI PCI-7334. As it's seen UMI-7774 represents a distributor, directing the control and feedback signals to individual axes of spectrometer (see Fig. C.4).
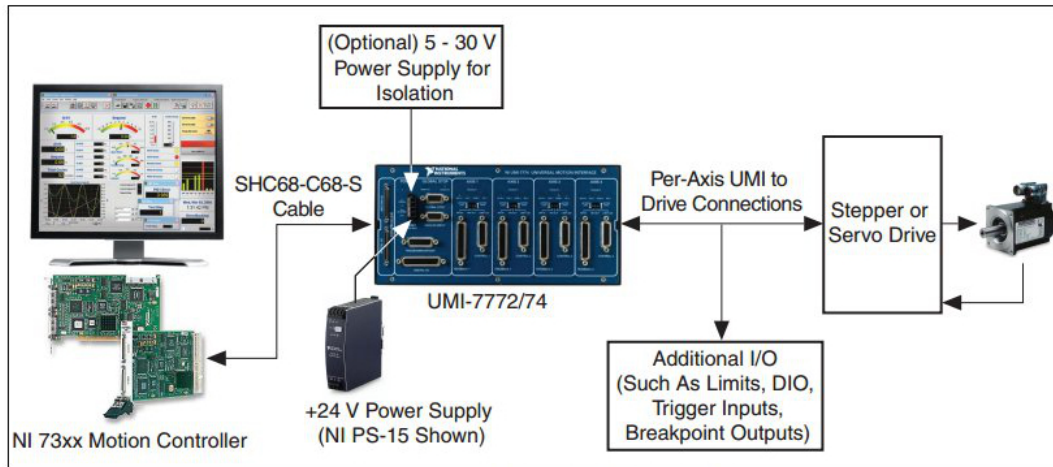
Fig. C.4.   : NI UMI-774 connection diagram [92].

The NI UMI-7774 has connections available for forward limit, reverse limit and home (same as reference position) sensors or switches. The limit sensors are located at physical ends of travel (see Fig. C.5).

The limits and home inputs are optically isolated sinking inputs on the NI UMI-7774. A sinking input is an input terminal that sinks current by providing a path to a supply common or ground. To cause current to flow through the input, the voltage applied to the limit and home inputs must be greater than 3.5 V and less than 30 V (in our case we have +12 V). Also, the source must be able to provide at least 7.2 mA to turn on the optical isolator and result in an ON condition. When the applied voltage is below 2 V, the input results in an OFF condition. For the end of travel limits to function correctly, the forward limit are located at the forward or positive end of travel, and the reverse limit at the negative end of travel. Configurations are done on the NI PCI-7334 motion controller using the NI motion driver software.
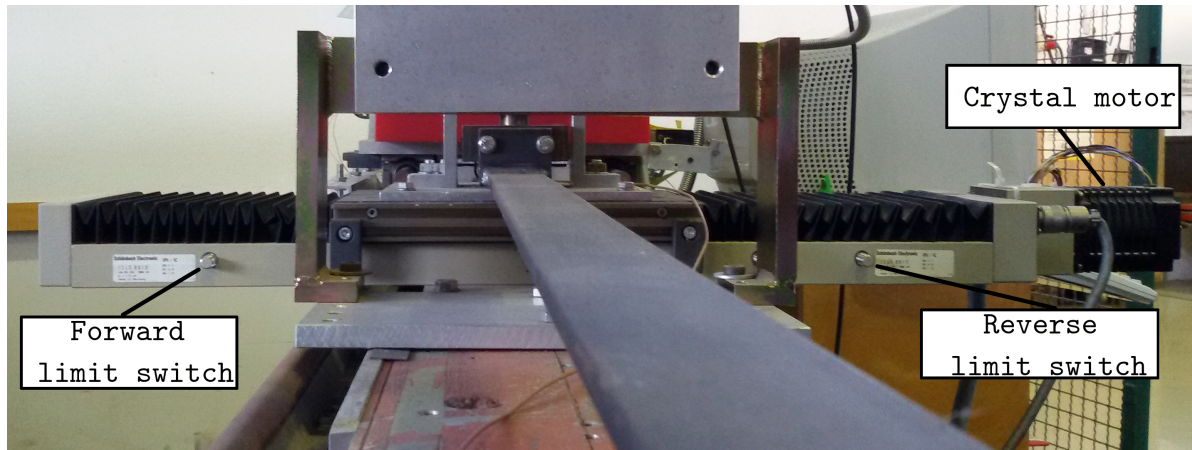
Fig. C.5. : Crystal linear table equipped with stepping motor and the forward and reverse limit switches.

The NI UMI-7774 routes 16 of the general-purpose digital input/output lines of the NATIONAL INSTRUMENTS' motion controller to a single 25-pin D-SUB connector. All 16 digital signals are optically isolated on the NI UMI-7774. These signals are configured in advance as inputs or outputs on the motion controller. To access the 16 (eight inputs and eight outputs) digital signals on the motion controller, one end of an additional SHC68-C68-S cable is connected to the 68-pin digital input/output connector on the motion controller and the other end to the 68-pin digital input/output connector on the NI UMI-7774 (see Fig. C.6).

1	NI 73xx Series Motion Controller	4	UMI-7774/72 Digital I/O Connector
2	NI 73xx Motion I/O Connector	5	SHC68-C68-S Cable
3	UMI-7774/72 Motion I/O Connector	6	NI 73xx Digital I/O Connector
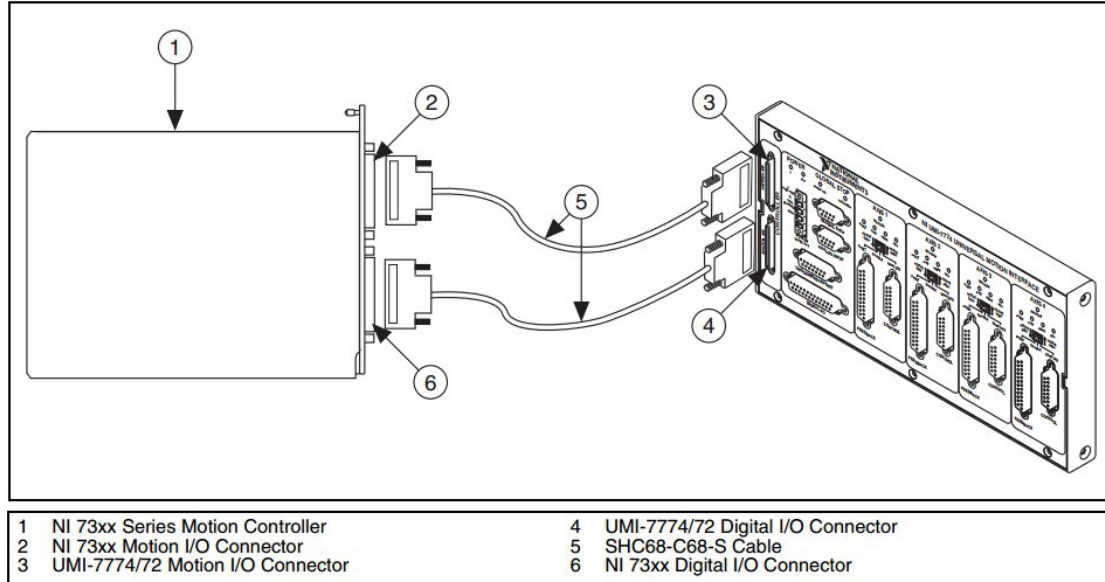
Fig. C.6. : NI UMI-774 connected to an NI PCI-7334 motion controller [92].

The "Stepper-Endstufen" crate [93] (see Fig. C.1) is the hardware complex, that directly communicates with stepper motors and limit switches. It consists of electronic cards (see Fig. C.7) receiving the signals originating at NI PCI-7334, containing the control-type commands (steps and direction), distributed by NI UMI-7774 and delivers them in appropriate format to stepper motors and to limit switches of the crystal, arm and detector table. Feedbacks provided by limit switches are directed to NI UMI-7774, from where through the KIT cable and 68-pin digital connector they are distributed to NI PCI-7334 and recorded

in 16 bit data registers. Labview©-based program reads these registers and displays their contents on a sreen. If the crystal position is between the borders defined by forward and reverse limit switches, then the corresponding "In Range" buttons are green. If the motors are at the border of switches then the buttons become red and the motors are commanded to stop.
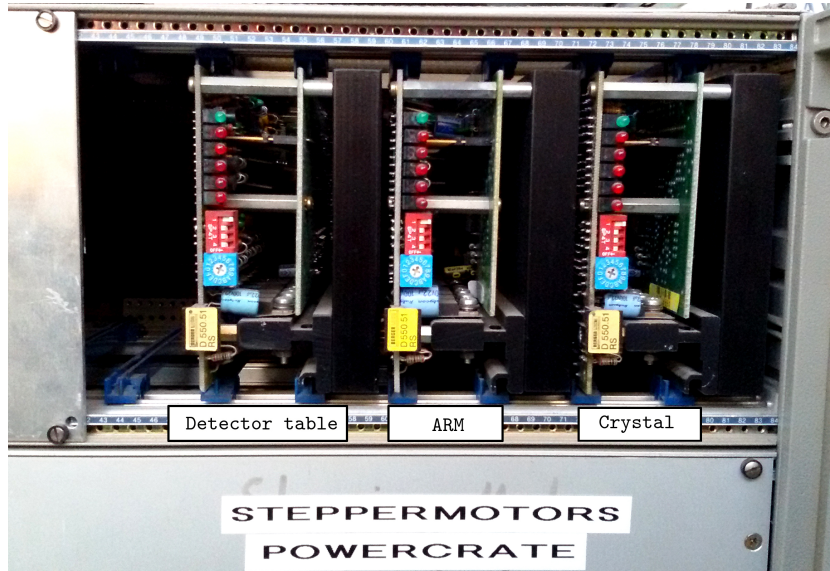
Fig. C.7. : Electronic cards for the control of stepping motors.

C.3.2. Fine adjustment of crystal angle

To control the small instabilities, the value of crystal angle is continuously monitored and readjusted by a feedback loop with a ceramic piezo-electric element (Fig. C.8). It simultaneously stabilizes the angular orientation crystal-detector to ≤ 0.2 seconds. When a current flows through a piezoelectric material, it creates a physical deformation which is proportional to the applied electric field, known as indirect piezoelectric effect [94].
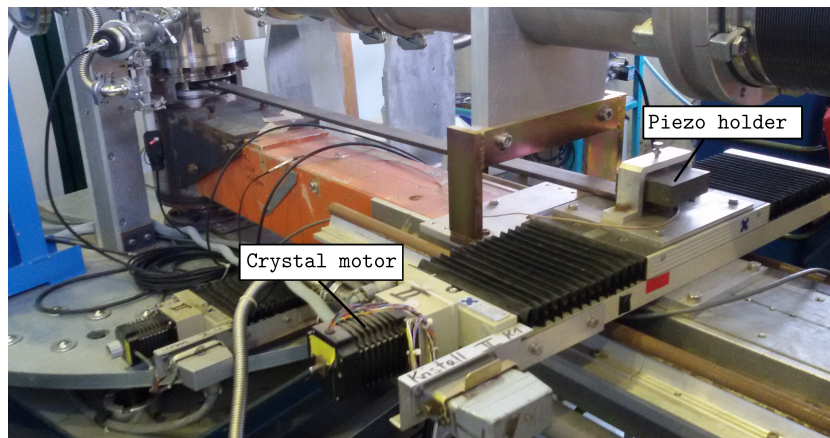
Fig. C.8. : Crystal rotation outside the vacuum is done using the special shaft which is connected to the crystal motor. Fine adjustment is done by Piezo-element, housed in a Piezo holder.

This precise deformation can be used to position objects with extreme accuracy. This piezo-actuator effect converts electrical energy into mechanical energy. In our setup 0-5 V is applied

to the piezo-element from FIELD-POINT crate (see Fig. C.1), which is internally amplified to 100 V, causing its expansion to 30 micron, corresponding to the crystal angle change by $\Delta\Theta=4.8$". In Labview$^{©}$-based program demonstrated on Fig.C.2, crystal angle is set first by "SOLL" position. After crystal rotation there is always a small difference between the "SOLL" and "IST" positions, which is effectively compensated using the piezo-element. Pressig the "PIEZO" button, activates the piezo-element, stabilizing the crystal angle. Fig.C.2 displays the real-time values of piezo voltage and current. Green color of "Piezo range" lamp informs about the successful operation of piezo-element, red color is usually the sign that piezo is unable to stabilize the crystal angle.

C.3.3. Crystal tilt

Crystal is tilted using the small-size motor located at crystal support Fig. C.9. It has a connection to crystal's linear potentiometer, changing the resistance according to the crystal tilt position. Figure C.2 serves the crystal tilting, using the voltages as input parameters for potentiometer (see Chap. 5.1.6).
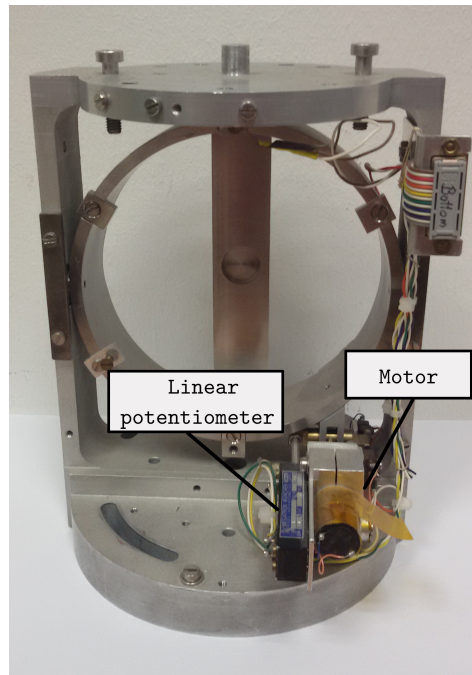
Fig. C.9. **:** Crystal support with motor and linear potentiometer.

C.3.4. Spectrometer arm angle Θ_{ARM}

The support arm of spectrometer bearing both crystal holder and detector can be rotated independently (arm angle), leaving the crystal-detector setting untouched. As explained in Chap. 5, this approach was developed in order to scan by arm rotation the fluorescence target to select the region of maximum intensity of emitted X-rays (see 5.1.5). When changing the arm angle, the crystal rotates together with the detector. Hence, the arm angle must be moved by twice $\Delta\Theta$ and the crystal angle by $\Delta\Theta$ in opposite direction in order to keep the position in the X-ray source.

From point of view of electronics, principle of arm movement is the same like in case of crystal. Separate part of Labview$^{©}$-based program panel is dedicated to arm control purpose

(labeled as arm angle on Figure C.2). Electronics involved in this operation are the same: NI PCI-7334 for generating the control signals (steps and direction for stepper motors), NI UMI-7774 as a signal distributor, directing the signals to corresponding axes, and "stepper-Endstufen" for direct communication with arm motors and limit switches (Fig.C.10). Angular encoder (or disk) of spectrometer arm has 5000 stripes, corresponding to one complete revolution. Stepper motor has to perform 1000 steps for one revolution, corresponding one spindle rotation of 5 mm. If we consider that the distance from the center of the arm disk to the stepper motor axis is 600 mm, this leads to one step corresponding to 1.58" of the arm rotation. Reference angle for spectrometer arm is different than for crystal and this is pre-defined at NI PCI-7334. Arm control needs no Piezo control, because the stepper motor accuracy is fulfilling and the crystal-detector orientation is not regulated by arm.
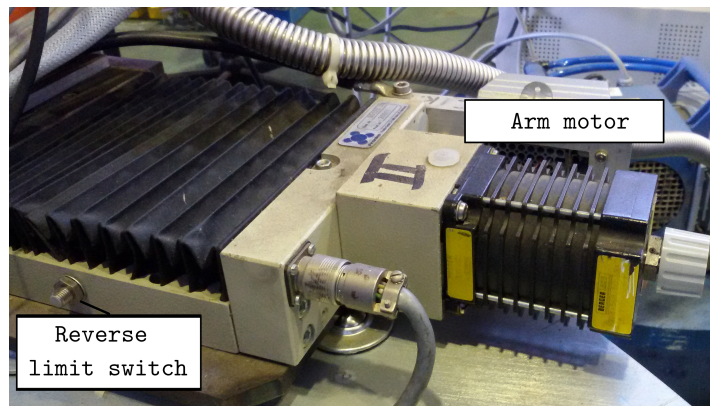
Fig. C.10.   **:** Spectrometer arm linear table with stepping motor and limit switches.

C.3.5. Crystal-detector distance (focal length Y_{CD})

For high-precision measurements of X-rays, one of the factor that plays an important role is the focal distance. Labview©-based program makes possible to regulate this distance using the button click. One can enter the desired value in millimeters and press the "START" on Figure C.2. Positive value instructs the system to increase the distance, negative is for decreasing. Forward and reverse limit switches ensure that detector moves only within the predefined borders (Fig. C.11). This ensures, that in case of mistakenly entered value, detector will be stopped at the end of its track, avoiding the overstretching of the metallic bellows in front and behind of detector cryostat.
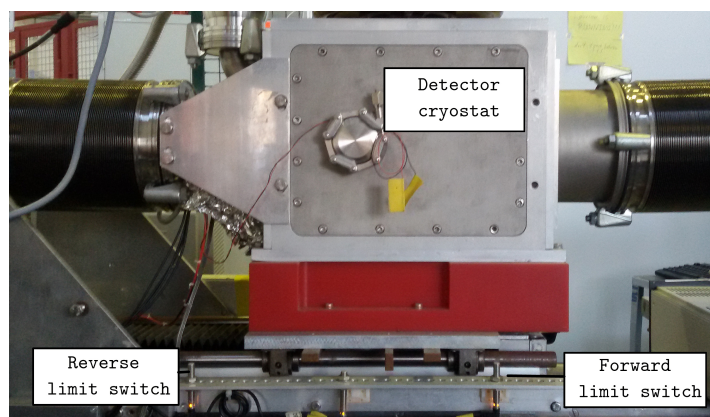
Fig. C.11.   **:** Limit switches along the detector table controlling the focal distance.

Stepper motors and limit switches are controlled by already known NI PCI-7334, NI UMI-7774 and "Stepper-Endstufen", moving the detector at desired distance. Detector movement is convoyed by a linear potentiometer (Fig. C.12), changing its resistance along the way. Resistance change causes the change of applied voltage on the potentiometer, which is calibrated in a system to the distance travelled. As a result of calibration, millimeters entered in Labview©-based program is translated into the voltage, that has to applied on the potentiometer in order to move the detector and potentiometer by the indicated distance. Stepper motors move the detector forward or backward until the desired position i.e. the corresponding resistance is reached on the potentiometer.
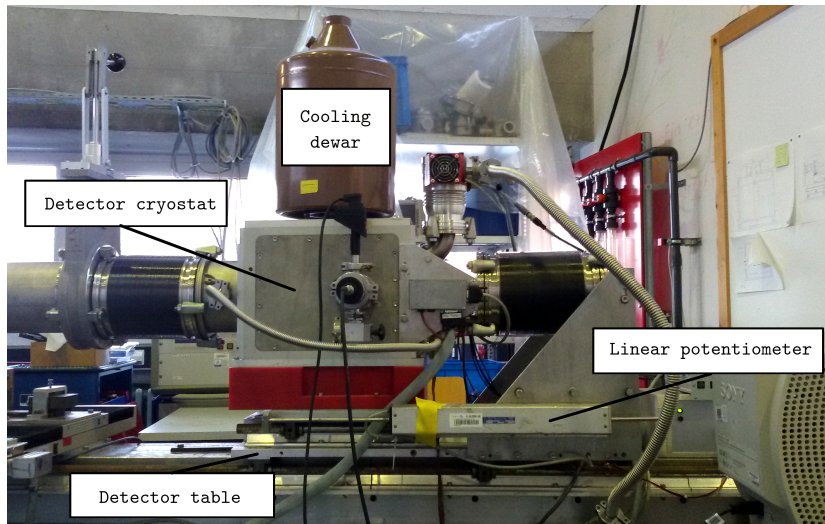
Fig. C.12. : Detector table equipped with linear potentiometer.

C.3.6. Principle of working of the limit switches

Each linear table of the spectometer is equipped with capacitive limit switches [95] (proximity sensors) shown on Fig. C.13. They define and control the borders between which the stepping motors can operate.
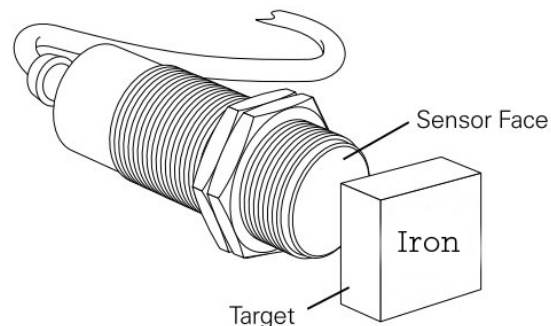
Fig. C.13. : Capacitive proximity sensor/limit switch [95].

Capacitive proximity sensors in our experiments are used for non-contact detection of metallic objects and especially made of iron. They use the variation of capacitance between the sensor and the object being detected. When the object is at a preset distance from the

sensitive side of the sensor, an electronic circuit inside the sensor begins to oscillate. The rise or the fall of such oscillation is identified by a threshold circuit that drives an amplifier for the operation of an external load. A screw placed on the backside of the sensor allows regulation of the operating distance. The sensing surface of a capacitive sensor is formed by two concentrically shaped metal electrodes of an unwound capacitor. When an object approaches the sensing surface it enters the electrostatic field of the electrodes and changes the capacitance in an oscillator circuit. As a result, the oscillator begins oscillating. The trigger circuit reads the oscillator's amplitude and when it reaches a specific level the output state of the sensor changes. As the target moves away from the sensor the oscillator's amplitude decreases, switching the sensor output back to its original state (see Fig. C.14).
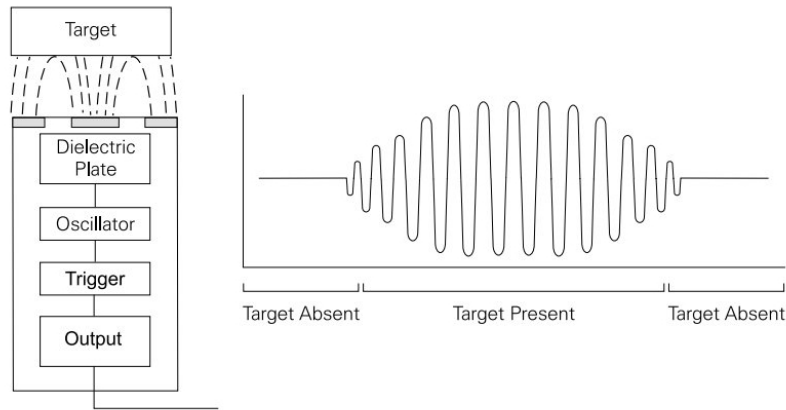
Fig. C.14. : Capacitive proximity switch operation [95].

In our case the sensitive distance is 1.5 mm. When the crystal's or arm's axis approaches the capacitive limit switch at this distance, the signal of +12V is generated, instructing the NI PCI-7334 to immediately stop the stepper motors activity. This signal is provided through the 68-pin digital input via the special cable KIT from National Instruments (Fig. C.1).

C.4. Monitoring of the spectrometer

C.4.1. Temperature measurements

Four main temperatures are measured at crystal spectrometer. Temperatures inside and outside of the detector cryostat and the crystal. Measurements are done using the PT-100 resistance thermometers (RTDs) [96]. They are sensors used to measure temperature by correlating the resistance of the RTD element with temperature. RTD elements consist of a length of fine coiled wire wrapped around a ceramic or glass core. The element is usually quite fragile, therefore it is placed inside a sheathed probe to protect it. The RTD element used in our experiment (model number S651PDX24B) is made from a pure copper. The material has a predictable change in resistance as the temperature changes and it is this predictable change that is used to determine temperature. RTD sensing elements have a repeatable resistance versus temperature relationship (R vs. T) and operating temperature range. The R vs T relationship is defined as the amount of resistance change of the sensor per degree of temperature change. The relative change in resistance (temperature coefficient of resistance) varies slightly over the useful range of the sensor.

The significant characteristic of metals used as resistive elements is the linear approximation of the resistance versus temperature relationship between 0 and 100°C. The equation below defines the temperature coefficient of resistance, α; its units are $\Omega/°C$.

$$\alpha = \frac{R_{100} - R_0}{100R_0} \tag{C.3}$$

R_0 = the resistance of the sensor at 0°C.
R_{100} = the resistance of the sensor at 100°C.

To characterize the R vs. T relationship of RTD over a temperature range that represents the planned range of use, calibration is usually performed at temperatures other than 0 and 100°C. This is necessary to meet calibration requirements, although RTD's are considered to be linear in operation it must be proven that they are accurate with regard to the temperatures they will actually be used. Calibration can be made at any temperature between -100 and 500°C.

In our case for PT-100 resistance thermometer 0°C corresponds to $100\,\Omega$. Thermometer is operated under $1 - 3\,\text{mA}$ constant current. Temperature change means the resistance change, leading to the change of voltage because of constant current, which is read out by specific control unit of NATIONAL INSTRUMENTS (FP-RTD-122 discussed in chapter C.5.1) and converted to the temperature value.

C.4.2. Monitoring the vacuum

Labview$^©$-based program measures vacuum in detector cryostat and at the rest part of spectometer. Measurements are done using the COMBIVAC CM 31 device [97]. It is a universal vacuum gauge which combines two principles of measurement - Pirani (Thermovac) and cold cathode (Penningvac) - for the measurement and control of vacuum pressures within the entire range between $1 \cdot 10^{-9}$ mbar and atmospheric pressure. The built-in RS 232 C interface permits computer controlled operation as well as the exchange of measurement data between the COMBIVAC CM 31 and a computer. This combination instrument is equipped with three measurement channels, two THERMOVAC channels and one PENNINGVAC. Six switching thresholds, three logarithmic chart recorder outputs and the self-monitoring facility permit integration of the COMBIVAC CM 31 into complex vacuum control arrangements. The two THERMOVAC channels are immediately active as soon as the line voltage is applied. The PENNINGVAC channel may be switched on and off through the second THERMOVAC channel. Measurement range for THERMOVAC channels is from $1 \cdot 10^{-3}$ to 1000 mbar, for PENNINGVAC $1 \cdot 10^{-9}$ - $1 \cdot 10^{-2}$ mbar.

C.4.3. THERMOVAC vacuum gauge (Pirani method)

The Pirani method of measurement makes use of the thermal conductivity of the residual gas. Heat conduction is another characteristic feature of gases which is closely related to the particle density. The thermal energy is transferred by molecule collisions. The efficiency of the transfer depends on the mean free path length of the particles. At a certain pressure range, the thermal conductivity is proportional to the pressure, but disturbing effects such as heat flow, thermal radiation, heat conduction from the contacts, etc. are to be expected.

The basic concept of a Pirani vacuum gauge relies on a thin wire (Fig. C.15) heated to a constant temperature, which is significantly higher than the temperature of the surrounding gas in the vacuum. The wire (typical diameter: 5 - 25 μm; length between 50 and 100 mm)

transfers the heat to the gas and is simultaneously part of an electrical circuit, for example of a Wheatstone bridge. The pressure dependent temperature can be derived from the monitored wire resistance. The actual parameter (the electric power that is required for the temperature stabilization) is pressure-dependent due to the proportionality of the thermal conductivity of a gas to the pressure. With a Wheatstone bridge, which is used for temperature stabilization,
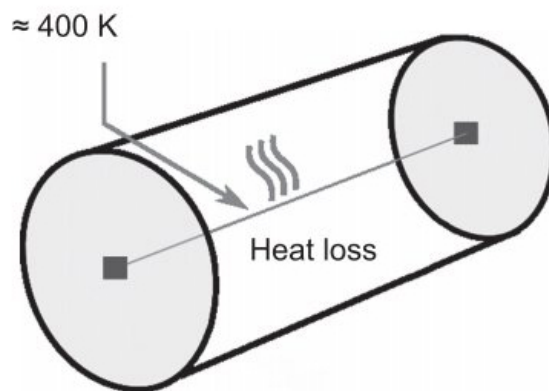
Fig. C.15. : Cut through a Pirani vacuum gauge

the difference between the heater voltage and a defined reference voltage can be measured at the same time. The difference between the actual and the reference voltage is adjusted to zero at a pressure value, where heat conduction does not play a role any more. This calibration mainly eliminates the unwanted effects of heat radiation and thermal conduction at connector pins of the wire. In general, the reference voltage corresponds with the heating voltage that has to be applied when the pressure in the system is far below the lower measuring limit.

Since the thermal conductivity of a gas is also a function of the average speed of the molecules and thus a function of the molar mass of the gas, thermal conductivity vacuum gauges measure the pressure dependent on the gas type. Therefore, the display is usually calibrated for nitrogen and air.

C.4.4. PENNINGVAC vacuum gauge (cold cathode method)

In case of PENNINGVAC (cold cathode), to measure the pressure a gas discharge is ignited within the sensor by applying a high voltage. In a cold cathode, the gas is ionized by collisions with electrons in the measurement volume, moving in crossed electric and magnetic fields in spiral paths. If a high voltage potential is applied between cathode and anode (Fig. C.16), all charged particles are accelerated towards the the corresponding electrode. During this process, other molecules can be ionized through inelastic collisions and secondary electrons can be generated. The accelerated particles initiate the gas discharge. The ionization of the residual gas is mainly achieved via electron ionization. Therefore, it is important to preserve those electrons in order to increase the ionization probability and to assure the discharge as long as possible, especially at low pressures. This is achieved with the additional external magnetic field. Penning cell contains two parallel cathodes with a ring anode between them. A strong permanent magnet encloses the cell. The magnetic field lines point perpendicular to the electric field vector and have typical strength of 100 up to 200 mT. The voltage difference between the cathodes and the anode is around 2 kV. In this configuration the potential energy surface reaches a saddle point in the middle of the anode ring, where all electrostatic forces are nearly cancelled out. Electrons are emitted from the cathode and accelerate towards

the ring anode. As soon as one component of the velocity vector is perpendicular to the magnetic field, the Lorentz force holds the electron on a spiral trajectory inside the anode, where the ionization occurs. Positive charged ions follow the electric field to the cathode. The
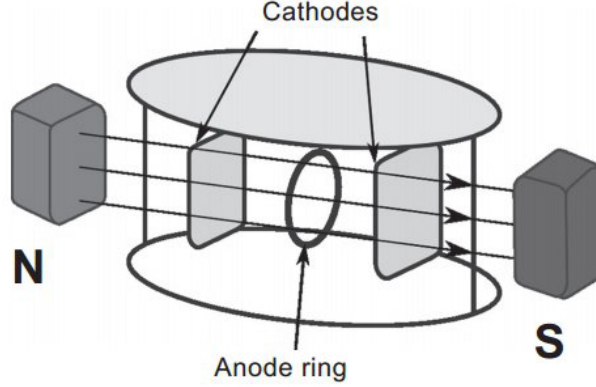
Fig. C.16. : Schematic sketch of a cold cathode gauge (Penning type).

impact of the ions generates a discharge current that can be measured. Ions are influenced by the magnetic field only slightly because of their high mass as compared to electrons. The correlation between the pressure and the discharge current is described by $p = const \cdot I^m$, where m varies between 1 and 1.4 depending on the design of the gauge. Hence, the discharge current is proportional to the pressure over a wide range. The ionization energy and the ionization probability are typically different for different atoms and molecules. Therefore, pressure measurement with cold cathodes is gas-type dependent. Typically, cold cathodes are used for pressure ranges below 10^{-3} mbar. Starting with this pressure the mean free path length is sufficient to keep the recombination probability low and the power needed for their operation reasonable. The lower pressure limit is given by the smallest detectable ion current, which is typically reached if the pressure drops to 10^{-11} mbar.

COMBIVAC CM 31 converts the measured vacuum to the output voltage. For THERMOVAC measurements

$$U_a = \frac{10}{6}(logP + 3) \tag{C.4}$$

For PENNINGVAC

$$U_a = \frac{10}{7}(logP + 9) \tag{C.5}$$

where U_a represents the output voltage in V and P is the measured pressure in mbar. As already mentioned data transfer from COMBIVAC CM 31 to the computer controlled under Labview$^{©}$ is done using the RS 232 C interface. When receiving messages through the interface, processing of commands entered via the keyboard may be delayed (up to 2 s max.). The instrument is controlled via the computer and when no transmission is in progress the instrument can be controlled via its keyboard. The RS 232 C interface requires at least 3 lines: Transmit line (TxD; Transmit data), Receive line (RxD; Receive data) and Reference ground (GND; Signal ground). The connections are made through a 9-way Sub-D connector. For the transmission of data, only characters from the 7-bit ASCII code are used. The baud rate is fixed to 2400 baud. The data format is fixed to:1 start bit, 7 data bits + 1 space, 1 stop bit. A parity bit is not generated and no parity check is run on received data.

C.5. FieldPoint front-end

Labview© system governs the whole spectrometer via the FieldPoint commercial modules from National Instruments housed in FieldPoint crate (Fig.C.17). On one hand they communicate with several intermediate devices (stepper motors, limit switches, potentiometers, resistance temperature detectors (RTDs)) which are in direct contact with spectrometer components. On the other hand all the monitoring and control information gather in these modules and the Labview©-based program reads them out and reflects on a screen. Four different types of FieldPoint modules are used in our experimental setup:
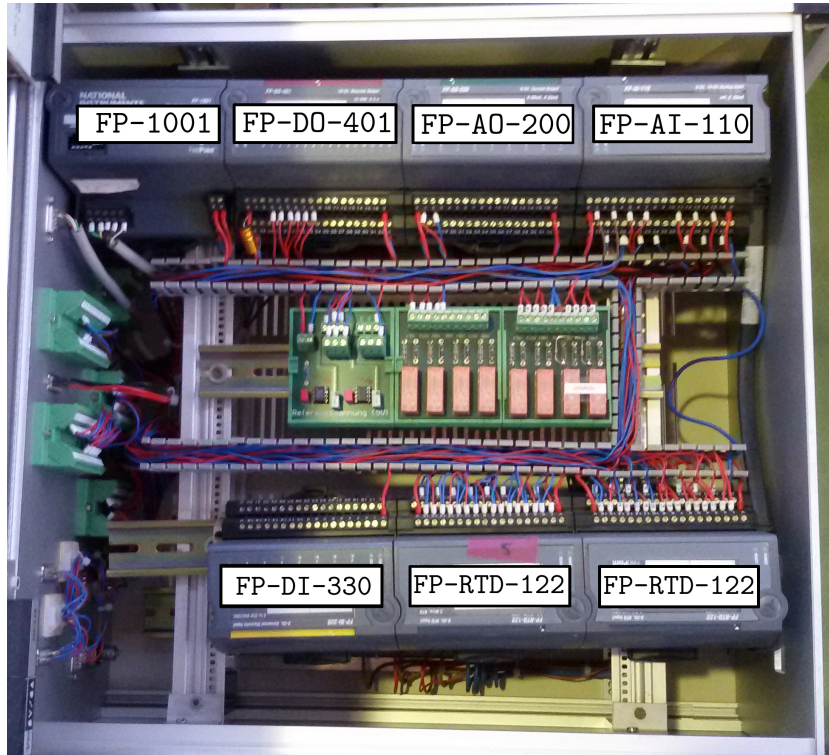
Fig. C.17. : FieldPoint crate housing the FieldPoint modules.

C.5.1. Fieldpoint modules

FP-1001

The FP-1001 is a network module for the FieldPoint system [98]. The FP-1001 FieldPoint network module connects an industrial RS-485 network to FieldPoint I/O modules using a simple ASCII protocol. Connection is done directly to any RS-485 adapter card installed in a host PC. Because RS-485 is inherently a multi-drop network, the FP-1001 does not provide a separate RS-485 repeater. The FP-1001 communicates over RS-485, utilizing full-duplex mode. It is optically isolated, which prevents fault coupling between the RS-485 network and the FP-1001. Network address and the baud rate are set using the switches. The addresses of the terminal bases in a FieldPoint bank (network module and I/O modules) are automatically configured by the network module to be sequentially higher than the network module's address (by default network address 0 and a baud rate of 115.2 kbps).

The power requirements for a FieldPoint bank that uses an FP-1001 network module are

calculated as follows:

$$Power = 1 \ Watt \ 1.55 \ * \ \Sigma(I/O \ Module \ consumption) \tag{C.6}$$

This is the amount of power the network module consumes from the power supply to power itself and the I/O modules. It does not include any power consumed by devices that are wired to the terminal bases. The operating instructions for each FieldPoint I/O module contain power consumption information.

FP-DO-401

In our experiment FP-DO-401 is used to supply the crystal onboard motor with 0-30 V signal [99], in order to tilt the crystal. Tilting continues as long as the "focus up" or "focus down" (Fig. C.2) buttons are being pressed. The whole process is organized in a way, that at the end we have reflected beam intensities for particular tilt positions, which makes possible to select a position of maximum reflectivity.

The FP-DO-401 is a FieldPoint discrete output module with 16 discrete output channels. Sourcing outputs supply 2 A per channel, 8 A^2 per module. The terminal base provides connections for each of the sixteen output channels and an external supply for field devices. Although the external supply is not needed for the internal operation of FP-DO-401, the outputs source current from this external supply. Each channel has an output terminal (V_{out}), a common terminal (COM) and a supply terminal (V_{sup}). The discrete outputs consist of optically-isolated sourcing outputs. In the ON state, a transistor is turned on between the positive external supply voltage and the output terminal. In the OFF state, this transistor is turned off, allowing only a small leakage current to flow. The impedance of the loads driven by the output channels are chosen in a way that the current supplied by any one channel in the ON state is no more than 2 A, and the total current supplied by all channels at any one time is no more than 8 A^2. The following formula ensures the total current per modul is not exceeded. Square of the current of each channel is added up and the result must be equal or less than 8 A^2. For example, one channel with 2A and four channels with 1 A would be as follows:

$$(2A)^2 + (1A)^2 + (1A)^2 + (1A)^2 + (1A)^2 \leq 8A^2 \tag{C.7}$$

In the ON state, there is an effective resistance of 0.3 Ohms between the output and the supply voltage. This resistance causes a voltage drop between the external supply voltage and the output voltage. For example, if the external supply voltage is 24 V and the output current is 1 A, the output voltage is 23.7 V (24 V - (1 A x 0.3 Ω)=23.7 V).

Labview$^{\copyright}$-based block diagram serving the FP-DO-401 module is shown on Fig. C.18.
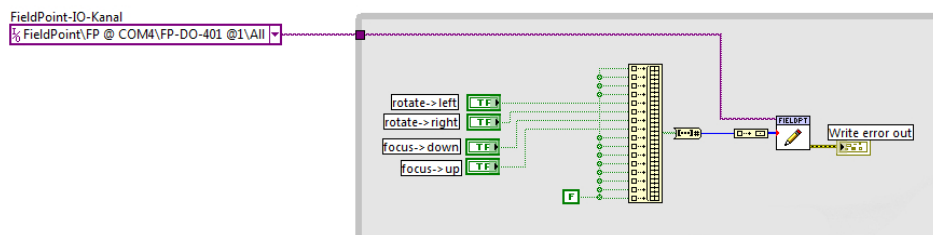
Fig. C.18. : Labview$^{\copyright}$-based block diagram for the FP DO 401 module.

On this block diagram the "focus-up" and "focus-down" variables are of boolean type. They are an input parameters of an array generator combining and converting the input values to a binary output which is finally synchronously written to a FieldPoint item. A FieldPoint item represents a channel or group of channels on a FieldPoint module.

FP-AO-200

The FP-AO-200 is a FieldPoint analogue output module with eight 0-20/4-20 mA current loop outputs [100]. It receives the operating power from the terminal base where it's mounted. The FP-AO-200 sources current from an external loop supply to a load / field device (in our case this is the Piezo-element). The terminal base provides connections for both the external loop supply and for the eight output channels. Each channel has an output terminal (I_{out}), a common terminal (COM) and a supply terminal (V_{sup}).

The output circuit of the FP-AO-200 is a sourcing current output, which means that it is designed to source current provided by an external loop supply to a device or load capable of sinking this current to the common voltage of the loop supply. The FP-AO-200 operates with an external loop supply from 5 to 24 VDC; however, this voltage dictates the maximum load impedance which the FP-AO-200 can drive. With a 24 VDC loop supply, each output can drive up to $1\,k\Omega$ of load impedance. With a 5 VDC loop supply, each output can only drive up to $100\,\Omega$. The FP-AO-200 updates the output channels as new values are sent to it by the network module. The time it takes to respond to a change on a single channel is between 3 and 6 ms. The response time to changes on all eight channels is 24 to 27 ms. Output ranges of each channel is configured independently for either $0 - 20\,\text{mA}$ or $4 - 20\,\text{mA}$ operation. In our case first version is selected. In this output range an over-range capability of 0.5 mA is considered, thus the actual full scale range is $0 - 20.5\,\text{mA}$. This extended range feature allows to compensate for span and offset errors in field devices. Each output channel is equipped with a monitoring circuit which compares the actual output current to the desired one. If the FP-AO-200 cannot source the desired output for one or more channels, an error condition is usually reported to the network module. Generally the cause of this error is an open current loop - either the load device or the loop supply is disconnected. However, this method or detection also catches errors caused by a load impedance that is too high, or a loop supply voltage that is too low, to provide the desired output current.

In our experiment FP-AO-200 supports the Piezo-element by sourcing a current provided by an external loop supply. Corresponding Labview©-based block diagram is shown on C.19. Sourcing current is made to be an input parameter of an array which is finally synchronously written to a FieldPoint item. Actual voltage and current values of Piezo-element is displayed on a screen for visualisation. Piezo-element stabilizes the crystal angle by reducing the difference between the "SOLL" (desirable) and "IST" (actual) angles.
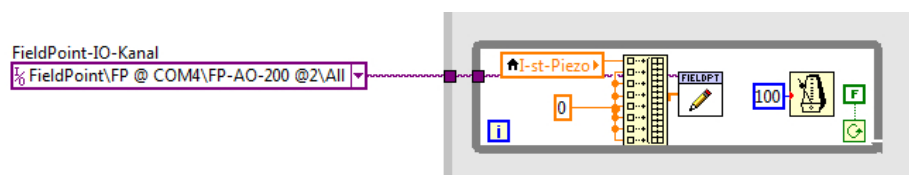
Fig. C.19. : Labview©-based block diagram for the FP-AO-200 module.

FP-AI-110

The FP-AI-110 is a 16-bit FieldPoint analogue input module with eight analogue input channels [101]. It can be used with voltage or current input signals and has three configurable filter settings (50 Hz, 60 Hz and 500 Hz) to reject noise. The hot plug and play operation allows to install it onto powered terminal base without disturbing the operation of other modules. The FP-AI-110 receives operating power from the terminal base. The terminal base provides connections for each of the eight input channels and an external supply to power field devices. Each channel has a separate input terminal for voltage (V_{in}) or current (I_{in}) inputs. Both voltage and current inputs are referenced to the COM terminals. The high accuracy of the FP-AI-110 module is accomplished by the use of 16-bit analogue-to-digital converter and through the use of a self-calibrating architecture. The FP-AI-110 continuously self calibrates the analogue-to-digital converter using a stable voltage reference. This method ensures that the measurements remain accurate over the time and temperature variations. The calibration occurs automatically and transparently to the application.

Input values for FP-AI-110 in our experiment are: high and low vacuum values for the detector cryostat and the rest part of the crystal spectrometer, crystal tilt position and the detector position. All of these values are interpreted by FP-AI-110 as input voltages ranging from 0 to 10.4 Volts. As it's described in earlier sections crystal and detector positions are monitored via the potentiometer, changing the resistance according to the position change. Resistance change leads to the voltage change, which is the input parameter for FP-AI-110.

Labview©-based block diagram reading the input voltages of FP-AI-110, calibrating them and displaying on a screen is shown on Fig. C.20. Corresponding inputs of this module is read out using the by FieldPoint read function through the dedicated driver (FP Read Polymorphic.vi). Read-out values are displayed in an appropriate format. Vacuum levels are displayed in mbar, crystal tilt (around the horizontal axis) as voltage corresponding to that tilt position and the detector position in millimeters (Fig.C.2).
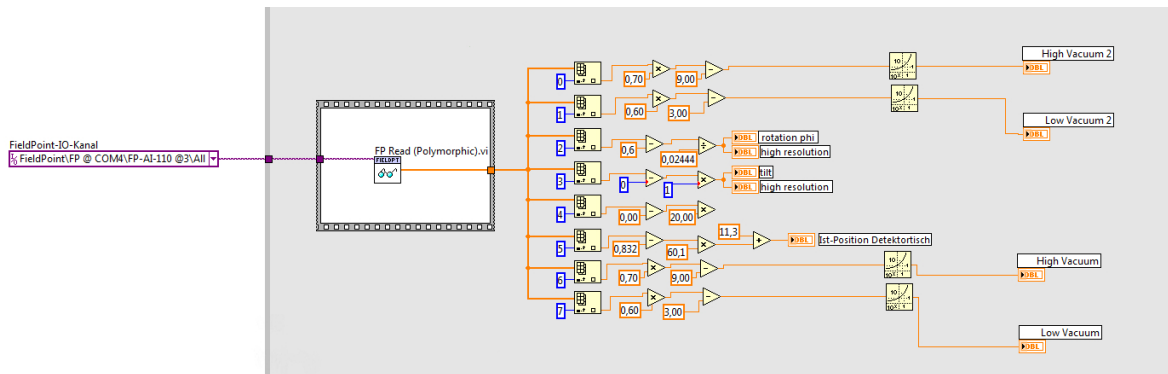
Fig. C.20. : Labview©-based block diagram for the FP-AI-110 module.

FP-RTD-122

The FP-RTD-122 is a FieldPoint RTD and resistance input module with eight 3-wire analogue input channels [102]. RTDs are known for their accuracy, repeatability, linearity and long term stability. Each input channel of the FP-RTD-122 can be used to measure the temperature of platinum RTDs or to measure the resistance of the RTD or other resistive device directly. The inputs are all filtered against 50 and 60 Hz noise, both common and normal mode. The 3-wire compensation works with the most common RTDs and is more accurate than typical

bridge techniques. Hot plug and play operation, safety isolation, noise filtering and 3-wire compensation work to ensure the stability of the operation. The terminal base provides connections for each of the three wires of a 3-wire RTD, can be also used with 4-wire and 2-wire RTDs (in our case the last one is used). There are excitation (EXCITE), sense (SENSE) and common (COM) terminals. The wiring connections depend on the number of wires on the RTD used in the system. The FP-RTD- 122 has eight input channels. All eight channels share a common ground reference that is isolated from other modules in the FieldPoint system. Each channel pulses a 0.25 mA excitation current out of the EXCITE terminal. The excitation current returns through the COM terminal. The SENSE terminal measures resistance and compensates for lead resistance errors. Each channel is filtered, then sampled by a 16-bit analogue-to-digital converter.

C.5.2. Temperature measurements

The FP-RTD-122 can be used to measure resistance directly in ohms. This capability is especially useful for RTDs that the FP-RTD-122 does not directly support or for measuring resistive devices others than RTDs. Two resistance ranges can be chosen: 400 and 4000 Ω. Any resistance value outside of the selected range, including the open circuit, results in an "out of range" error being reported for the affected channels.

The FP-RTD-122 can directly measure the temperature of a platinum RTD of either 100 or 1000 Ω nominal resistance and for 6 TCR (temperature Coefficient of Resistance or alpha, α) values. The TCR of an RTD is the average temperature coefficient of the resistance of the RTD from $0°C$ to $^{1}00°C$ and is the most common method of specifying the behaviour of an RTD.

The FP-RTD-122 linearises the resistance value and returns a reading in units of temperature. In our case the temperature range is set to -200 to $+850°C$ for all of the channels. RTD types are specified by material composition, nominal resistance at $0°C$, and TCR. The FP-RTD-122 can directly measure the temperature of platinum RTDs of either 100 or 1000 Ω nominal resistance. These RTDs are commonly referred to as PT100 or PT1000 RTDs, respectively.

The FP-RTD-122 uses a linearisation curve known as the Callendar-Van Dusen equation to measure the temperature of RTDs. The equation is as follows:
Temperatures below $0°C$:

$$R_T = R_0[1 + AxT + BxT^2 + C * T^3x(T - 100°C]$$ (C.8)

Temperatures above $°C$:

$$R_T = R_0[1 + AxT + BxT^2]$$ (C.9)

T = temperature in $°C$; R_T = RTD resistance at temperature T; R_0 = RTD nominal resistance at $0°C$; A, B, C are the coefficients for each of TCR values.

Input values for FP-RTD-122 in our experiment are: the temperatures inside and outside of detector and the crystal temperature. Labview©-based block diagram reads the parameters measured by this module in 300 millisecond interval and displays them on a screen is shown on Fig. C.21.

Two FP-RTD-122s are used in our monitoring and control system, because each of of them can measure only eight parameters (temperature/resistance) because of eight input channels. They are read out channel by channel by FieldPoint read function and the read-out values are manipulated individually before displaying on a screen. Manipulations are needed to consider the results of calibration in order to display them in a high precision. Temperature labelled R1 is controlled by an alarm system, which is programmed to alert if R1 goes beyond the pre-defined values (in our case beyond -95 and $-105°C$).

Fig. C.21. : Labview©-based block diagram for the FP-RTD-122 module.

C.6. Labview©-based block diagrams
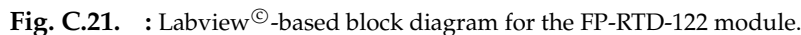
Block diagram stands in the background of Labview©-user interface which is shown on Fig. C.2 and makes it operational. Block diagrams are the alternative of standard programming scripts, which functions are described in a form of graphical blocks. The last subsections described how the FieldPoint modules are governed at this level. The next subsections cover the spectrometer axes (crystal, arm and detector table) control on the level of block diagrams.

C.6.1. Initialization of the communication port

At first stage the communication ports and the motion controller has to be initialized. Controller initialization is done by element 1 on Fig. C.22. It initializes the specified controller according to the settings as configured in Measurement & Automation Explorer (MAX) which is the part of Labview© package. Board ID which is shown on a figure is a unique number assigned by MAX to send and receive commands and data to or from a specific NI motion controller (in our case this is the NI-PCI-7334). Outputs of this block are the "Bd ID Out" provided for flow control and for the connection to another element and the "Error Out" to provide the error information if it occurs. Controller initializer is connected to Set I/O Port Direction element (2) and to the Set I/O Port Polarity element (3) in order to setup the communication ports for operation. (2) Sets the direction of a general-purpose I/O port as input or output. In our case it's set to input by direction indicator which is the bitmap of directions for the bits in the I/O port. Set I/O Port Polarity element sets the bit polarity in a general-purpose I/O port. In our case all the bits are set to active high. From this point, signals are directed to corresponding axes.

C.6.2. Crystal axis control

As described earlier crystal and arm positions are monitored using the IK-220 HEIDENHAIN cards. To operate them under Labview©, the system needs to load their drivers, i.e. small programs which are kind of mediator between the apparatus and the high level software (Labview©). Common drivers are supplied by manufacturer (National Instruments in this case). At first stage of angular setup, these drivers are loaded and the IK-220s are initialized from Labview©-based program (Fig. C.23).

Crystal can be set to a reference position, which is considered as the null position or the initial position of the crystal. As it's already known, the reference angle is entered in a form
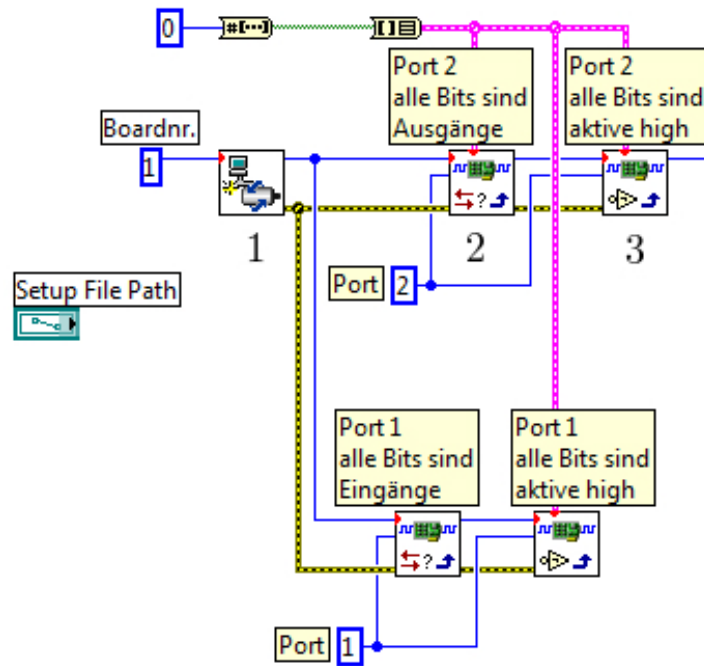
Fig. C.22. : Labview©-based block diagram for the initialization of the motion controller and the Input/Output port.

of degrees, minutes and seconds from the user interface of Labview©. First the reference position is set-up (1) and then is activated (2), leading to search of the indicated position and then adjustment of the crystal at that position. At this point the IK-220 cards point to the actual position of the crystal which is equivalent to the reference angle.

The crystal angle is set up first via the stepper motors and then the fine adjustment with piezo-element is demonstrated on Figure C.24 using the Labview© block diagrams. When the START button is pressed, crystal stepper motors start to act, based on the parameters like the number of steps, motor acceleration factor, which are the entry parameters of Load Velocity element/block (1). Output of this element is used for the flow control and is connected to Load Acceleration element (2), which loads the maximum acceleration and/or deceleration value for an axis. Acceleration defines how quickly the axis comes up to speed and is typically limited to avoid excessive stress on the motor, mechanical system, and/or load. A separate, slower deceleration is useful to provide the gentle stop. The next element on the way is the Set Operation Mode element (3), which is used both during initialization and during normal motion control operation to configure the mode of operation for all trajectory commands to the axis. In absolute position mode which we use, target positions are interpreted with respect to an origin, reference, or zero position. The origin is the limit switch or encoder index position. An absolute position move uses the preprogrammed values of acceleration and velocity to complete a trajectory profile with an ending position equal to the loaded absolute target position. Set Operation Mode element (3) is connected to the Load target Position element (4) which loads the target position for the next axis move. Target positions can be anywhere within the 32-bit position range. Desired (SOLL) and reference angles are already entered. Steps to be done is calculated and displayed on a screen and the Start Motion element (5) commands the stepper motors to start the operation. At the end crystal's actual position (IST) is nearby the desired value. At this point, the Piezo-element is used to decrease the difference between SOLL and IST values by changing the applied voltage. Actual values
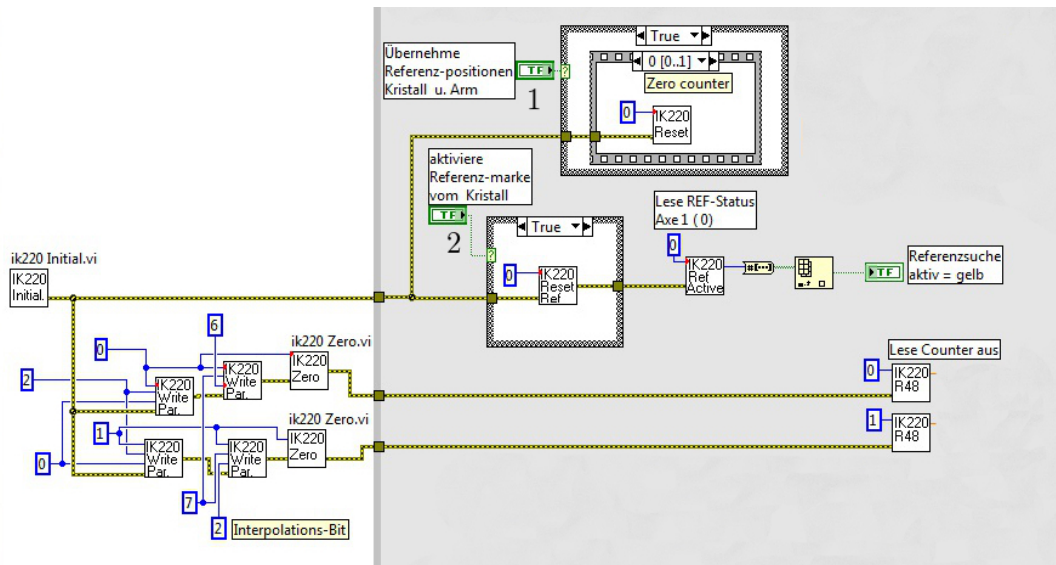
Fig. C.23. : Labview©-based block diagram for HEIDENHAIN IK-220 cards. Demonstrates the initialisation of the driver programs of IK-220, reference angle adoption and activation.

of the voltage and current of Piezo is displayed permanently. Tolerance limit is set to 3" of angular difference. If this is satisfied the Piezo In Range lamp becomes green on Figure C.2, reporting the successful operation of Piezo. Pressing the STOP/HALT button when stepper motor is running, causes the activation of Stop Motion element (6) attempting to stop the motor(s) with a near infinite rate of deceleration.
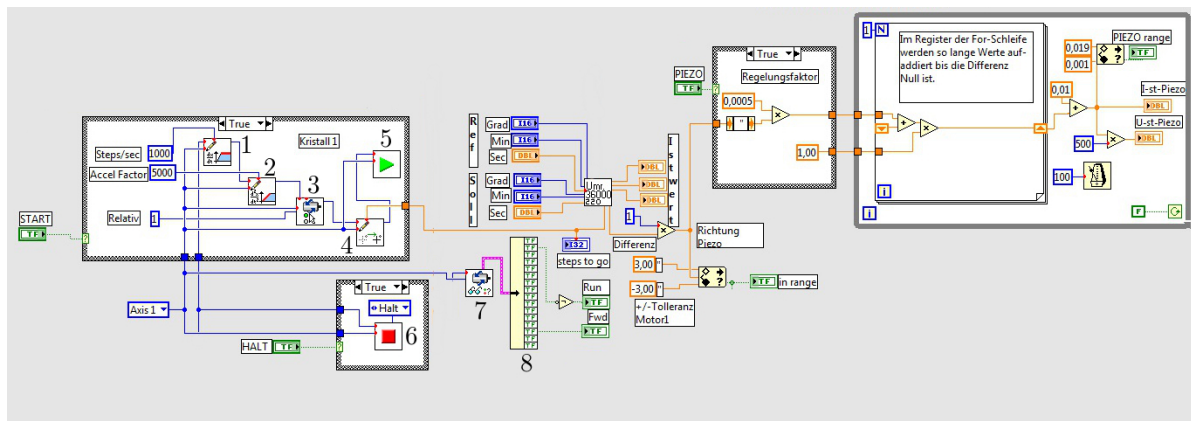
Fig. C.24. : Labview©-based block diagram for crystal angle setup.

Element 7 is the Read per Axis Status element, reading the motion status on a per-axis basis. Output value (Per Axis H/W Status) is a cluster of motion status for the axis. The Read Per Axis Status returns the trajectory and motion I/O status and also the success or failure status of the most recent Find Reference sequence. Element 8 decomposes the contents of the input claster in a way that each cluster element is output via the separate channel. As a result, when the crystal motors are running, the corresponding lamp "RUN" and also the direction indicator (forward or reverse) is activated on Figure C.2.

C.6.3. Arm axis control

Spectrometer arm is controlled by similar Labview©-based block elements as in case of crystal. Start and stop motion elements activate and halt the arm stepper motor. Reference and SOLL positions are entered, activated and displayed on a screen. Operating parameters of arm are different: acceleration factor of the stepper motor is 2000 instead of 5000 and the number of stripes of arm disk is 5000 insead of 36000 (Fig. C.25). Arm axis is not equipped with high-precision Peizo-element, because there is no need for that. Stepper motors set the arm angle in a precision of 10" of angle, which is sufficient, because the bragg angle adjustment is perfectly done at crystal level. Thus, the tolerance level in arm stepper motors is set to ±10". If this is satisfied then the angle is in range, reported by the corresponding green lamp on Fig C.2. When the arm motor is running, the corresponding lamp "RUN" and also the direction indicator (forward or reverse) is activated. Crystal and arm angle adjustment finalizes the bragg angle set up procedure. As it's proved by experiment, Labview© monitoring and control system serves this purpose quite effectively and provides the high-level long-term stability.
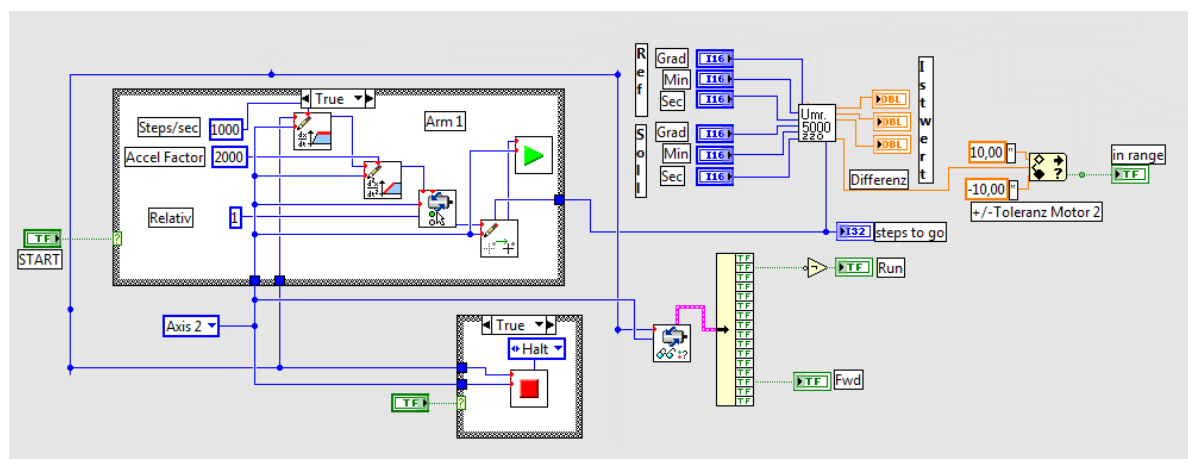
Fig. C.25. : Labview©-based block diagram for arm angle setup.

C.6.4. Detector axis control

Detetcor axis control gives possibility to change the focal distance between the crystal and the detector. Current position is monitored using the linear potentiometer, changing its resistance when the detector is moving. Labview©-based block diagram which is use for detector axis control is shown on Figure C.26. Number of steps and acceleration factor are defined for the stepper motor numerically and set as input parameters. Distance the detector must travel is given in millimeters. Positive sign indicates the crystal direction (i.e. decrease of focal distance) and the negative sign is for opposite direction.

Detector axis control considers the reference movement of the detector, which is defined in advance. This ensures that the detector can be set at any time to the position which is equivalent to the null position, or the starting point. Reference movement is realized by using the Find Reference element (1 on Fig. C.26) in Labview©-based block diagram. It executes a search operation to forward reference position, which is selected as a search type. Input parameters are the axis number and the Board ID, which is a unique number assigned by Measurement & Automation Explorer (MAX) used to send and receive commands and data to or from a NI motion controller.Setting the Find Reference search type to Forward Limit
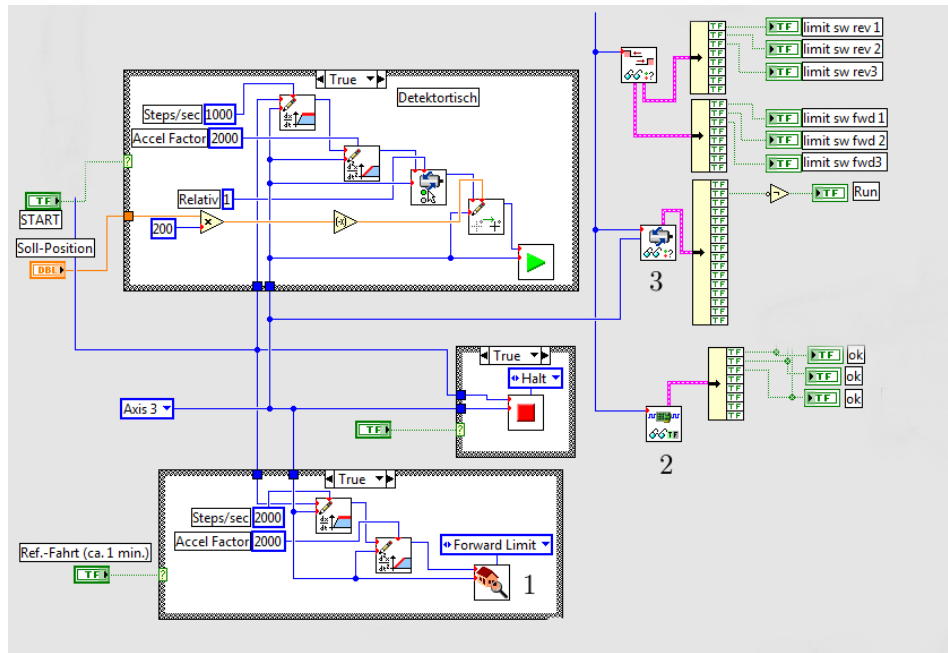
Fig. C.26. **:** Labview$^{©}$-based block diagram for detector axis control.

initiates a search sequence to find the forward limit. The search is performed at the maximum find velocity which is specified in advance. The velocity of the axis is set to this value during the find operation. When the search operation initiates the axis,

starts moving in the direction of the limit. When the axis encounters the limit in that direction the search completes and the function returns a true value.

C.6.5. Read Input/Output Port

This is achieved using the Read Port element (2 on Fig. C.26). It reads the logical state of the bits in an I/O port (On or Off, True or False). Input parameters are the port number and the Board ID. Output is the port data, representing the the bitmap of the logical state of the I/O port. Readout is executed continuously in order to monitor the signals connected to an input port. The polarity of the bits in the port determines whether an On state is active high or active low. Port state is monitored for each axis. If there is no error during the readout, then the status "OK" is activated and displayed at individual axis panels (Fig. C.2).

C.6.6. Status of limit switches

Each linear table of the spectrometer is equipped with limit switches in order to prevent damages of the spectrometer from motion operations outside before defined borders. Therefore, the status of the limit switches is permanently monitored.

The status of limit switches is read out by using the Read Limit Status element (3 on Fig. C.26) from Labview$^{©}$-based block diagram. It reads the instantaneous state of the hardware or the software limit inputs. Input value for this control element is the board ID, indicating the axis for which the limits are assigned. Two outputs are available: forward and reverse limits. Forward Limits is the bitmap of forward limit status. For axis X - if true, forward limit is True (On). If false, forward limit is false (Off). The same for reverse limit switches. The polarity of the limit inputs determines whether an On state is active high or active low. When Limit

Type = Software Limits, this element returns the state of the forward and reverse software limits. A True (On) indicates that the forward or reverse limit position for the corresponding axis has been reached or exceeded.

C.7. Archiving the monitored data

Archiving data is an important feature of Labview©-based monitoring and control systems. The monitor parameters are saved in an ASCII text file in regular time intervals providing an electronic logbook for further analysis. This is especially important when troubleshooting the hardware or software problems of the crystal spectrometer. The sequence of values of could be evidence for malfunctions and a selection criterion for later data analysis. Figure C.27 shows the Labview©-based block diagram implementing the data archive.
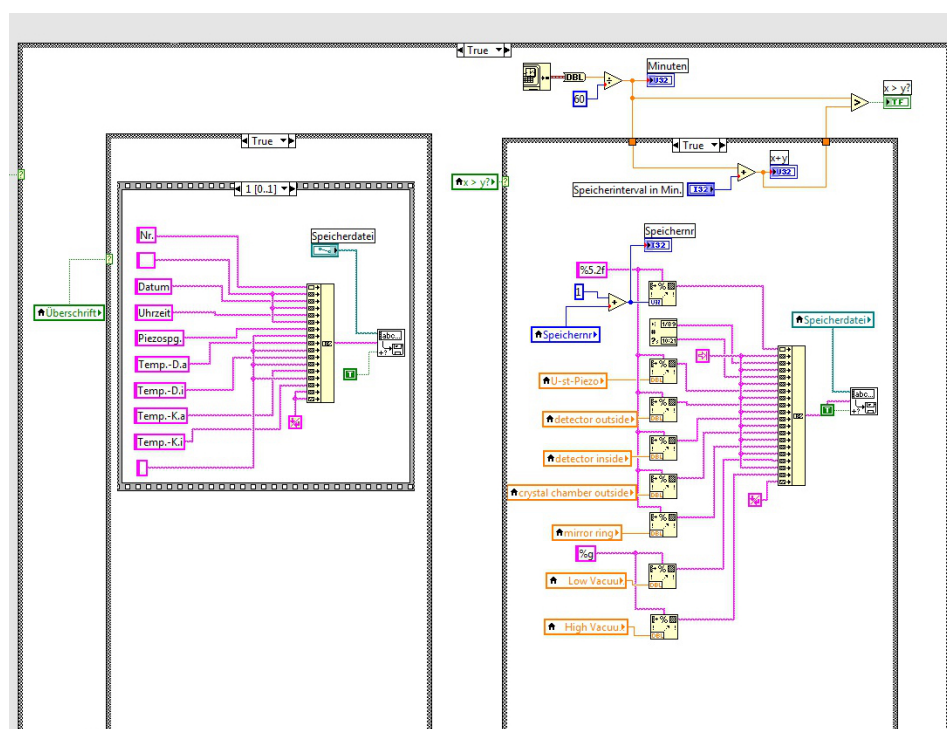
Fig. C.27. : Labview©-based block diagram for archiving the monitored data.

The time interval for saving is an adjustable parameter. Normally five minute is the time interval used in our experiment. Name and path to the archive file is entered from Figure C.2 and clicking the "ON" button starts the archiving procedure. Data are saved in a string format in a TXT file (Fig. C.28). First at the beginning of the file column titles are written: record number, date, time, piezo voltage, detector temperature outside, detector temperature inside, crystal temperature outside the chamber, crystal temperature inside the chamber, vacuum in cryostat, vacuum in the rest of the spectrometer syste). Data are have to be converted to text strings before archiving. The converter elements are shown on the right side frame on Figure C.27.

Fig. C.28. : Labview©-txt data file of temperature values, measured and archived by using Labview©.

LIST OF FIGURES

LIST OF TABLES

BIBLIOGRAPHY

[1] S. Lenz *et al.*, Phys. Lett. B **416** 50–55 (1998).

[2] D. Gotta *et al.*, Nucl. Phys. A. **660** 283 (1999).

[3] D. Gotta, *Precision spectroscopy of light exotic atoms*, Prog. Part. Nucl. Phys. 52, 133–135 (2004).

[4] D. F. Anagnostopoulos, R. Sharon, D. Gotta, and M. Deutsch, Phys. Rev. A **60**, 2018 (1999).

[5] Th. Strauch, diploma thesis, *Aufbau eines Bragg Kristallspektrometers und Test mit Barium L$\gamma_{2,3}$-Spektren*, Universität Siegen, Germany (2005).

[6] Ch. Weidemann, diploma thesis, *Messung der chemischen Verschiebung von Kα- und Kβ-Übergängen in Mangan*, Universität Jena, Germany (2007).

[7] M. Deutsch *et al.*, Phys. Rev. A **51**, 283 (1995).

[8] E. Hölzer *et al.*, Phys. Rev. A **56**, 4554 (1997).

[9] C. T. Chantler, M. N. Kinnane, C.-H. Su, and J. A. Simpson, Phys. Rev. A **73**, 012508 (2006).

[10] P. Glatzel and U. Bergmann, Coord. Chem. Rev. **249**, 65 (2005), and references therein.

[11] M. O. Krause and J. H. Oliver, J. Phys. Chem. Ref. Data, Vol **8**, No. 2, 329 (1979).

[12] S. I. Salem and P. L. Lee, At. Data Nucl, Data Tables, **18**, 233 (1976).

[13] K. Sakurai and H. Eba, Nucl. Instr. Meth. B **199**, 391 (2003).

[14] C. J. Pollock and S. DeBeer, Acc. Chem. Res. 48, 2967 (2015).

[15] Ph. Wernet *et al.*, Phys. Rev. A **63** 050702 (2001).

[16] I. Lindgren, J. El. Spect. Rel. Phen., **137-140**, 59 (2004).

[17] F. de Groot, Coord. Chem. Rev. **249**, 31 (2005).

[18] M. Oku, K. Wagatsuma, and T. Konishi, J Electron Spectrosc. Relat. Phenom. **98-99**, 277 (1999).

[19] A. Meisel, G. Leonhardt, and R. Szargan, X-Ray Spectra and Chemical Binding, vol. **37** of *Chemical Physics*, Springer (1989).

[20] M. O. Krause, *Atomic Radiative and Radiationless Yields for K and L Shells*, J. Phys. Rev. Data, Vol **113**, No. 2 (1959).

[21] M. Fritsch *et al.*, Phys. Rev. A **57**, 1686 (1998).

[22] L. G. Parratt, Phys. Rev. **50**, 1 (1936).

[23] J. Benard, *L'oxidation des métaux*, Tome II, Gauthier-Villars Editéur, Paris, 132 (2005).

[24] G. F. Guillermet *et al.*,Int. J. Thermophysics **11** 05 (1990).

[25] N. Môri and T. Mitsui, J. Phys. Soc. Japan **25**, 82 (1968).

[26] Calculations based on http://hyperphysics.phy-astr.gsu.edu/hbase/tables/fermi.html#c2.

[27] David R. Lide, ed., *CRC Handbook of Chemistry and Physics*, CRC press, Boca Raton, FL, USA (2005), p. 12-233.

[28] P. Glatzel, PhD thesis, *X-ray Fluorescence Emission Following K Capture and 1s Photoionization of Mn and Fe in Various Chemical Environments*, Universität Hamburg (2001).

[29] R. Deslattes, E. G. Kessler, Jr., P. Indelicato, L. de Billy, E. Lindroth, and J. Anton, Rev. Mod. Phys., vol. **75**, no. 1, 35 (2003).

[30] V. M. Pessa, J. Phys. C: Solid State Phys. **8**, 1769 (1975).

[31] R. P. Gupta and S. K. Sen, Phys. Rev. B **10**, 71 (1974).

[32] P. Indelicato *et al.*, Eur. Phys. J. D **3**, 29 (1998).

[33] U. Köbler, A. Hoser, and J. -U. Hoffmann, Phys. B **382**, 98 (2006).

[34] W. L. Bragg, Proc. Cambridge Philos. Soc.**17**, 43 (1913).

[35] A. E. Sandström, *Handbuch der Physik.*, Band XXX, Springer, Berlin, 78 (1952).

[36] J. Als-Nielsen *et al.*, *Elements of modern X-ray Physics.*, John Wiley and Sons Ltd, 1st edition, West Sussex, England (2001).

[37] E. Wagner, Phys. ZS **17**, 407 (1916).

[38] H. H. Johann, Z. Phys. **69**, 185 (1931).

[39] J. Eggs, K. Ulmer, Z. angew. Phys. **20(2)**, 118 (1965).

[40] G. Zschornack, G. Müller, and G. Musiol, Nucl. Instrum. Meth. **200**, 481 (1982).

[41] T. Johansson, Z. Phys. **82**, 507-515 (1933).

[42] D. F. Anagnostopulos *et al.*, Nucl. Instr. Meth. A **545**, 217 (2005).

[43] D. S. Covita *et al.*, Rev. Scient. Instr. **79**, 033102 (2008).

[44] D. Gotta and L. M. Simons, Spectr. Chim. Acta B **9**, 120 (2016).

[45] M. Sanchez del Rio and R. J. Dejus, Proc. SPIE Int. Soc. Opt. Eng. **3448**, 246 (1998); *ibidem* **5536**, 171 (2004); http://www.esrf.eu/computing/scientific/xop2.1.

[46] J. R. Janesick, *Scientific Charge-Coupled Devices*, SPIE press, USA, (2000).

[47] N. Nelms, PhD thesis, *A New Determination of the Charged Pion Mass and Muon Neutrino Mass Upper Limit from Exotic Atom X-ray Spectroscopy*, University of Leicester (2002).

[48] A. D. Holland *et al.*, Proc. SPIE **2808**, 414 (1996).

[49] N. Nelms *et al.*, Nucl. Instr. Meth. A **484**, 419 (2002).

[50] M. M. H. Khan, Master thesis, *Characterization of Emission Spectra of an ISOVOLT 3003 X-ray Tube by using a Fast Readout Charge-Coupled Device*, Aachen University of applied science, Germany (2013).

[51] H. Gorke *et al.*, AIP conf. proc. **793**, 341 (2005).

[52] *Bragg crystal were manufactured in collaboration with* Carl Zeiss AG, D-73447 Oberkochen, Germany.

[53] Synthetized according to J Du Bois,*et al.*, Journal of the American Chemical Society, 1996, 118(4), 915-916.

[54] Dimanganese Decacarbonyl Mn(0), commercial, bought from Alfa Aesar GmbH & Co KG, 76185 Karlsruhe, Germany.

[55] Cyclopentadienylmanganese Tricarbonyl Mn(+I) (CAS Number: 12079-65-1), commercial, bought from Stem Chemicalc Inc, 67800 Bischheim, Strasbourg France.

[56] P. Indelicato *et al.*, Rev. Scient. Instr. **77**, 043107 (2006).

[57] S. A. Boyer, *Supervisory Control And Data Acquisition*, ISA society, USA, (2004).

[58] N. Nelms, program xcCCD, priv. comm.

[59] N. Nelms, program XCAM, priv. comm.

[60] D. Gotta, program CSDCLUSTER, priv. comm.

[61] D. Gotta, program FITOS, priv. comm.

[62] L. Simons, program XTRACK, priv. comm.

[63] J. Du Bois et al., J. Am. Chem. Soc. **118**, 915 (1996).

[64] V. H. Sanner, *Die K−Emissions- und Absorptionsspektren der Elemente Kalium bis Kupfer und einiger ihrere Oxide*, Inaugural–Dissertation, Uppsala, 1941.

[65] A. Meisel and E. Döring, *Über den Einfluss chemischer Bindung auf das Kα Dublett von Mangan*, Leipzig (1962).

[66] T. A. Tyson et al., Phys. Rev. B **60**, 4665 (1999).

[67] S. Raj et al., Phys. Rev. B **65**, 193105 (2002).

[68] S. Tanaka and G. Okuno, Jap. Jour. of Phys. **10**, 45 (1935).

[69] A. S. Koster and H. Mendel, J. Phys. Chem. Solids **31**, 2511 (1969).

[70] Y. Gohshi and A. Ohtsuka, Spectrchim. Acta B **28**, 179 (1973).

[71] K. Tsutsumi, H. Nakamori, and K. Ichikawa, Phys. Rev. B **13**, 929 (1976).

[72] B. S. Acharya, Rajeev, and L. Pradhan, Jap. J.Appl. Phys. 29, 1278 (1990).

[73] G. Peng et al., J. Am. Chem. Soc. **116**, 2914 (1994).

[74] Y. Tamaki, X-ray Spectrom., **24**, 235 (1995).

[75] U. Bergmann et al., J. Phys. Chem. B 102, 8350 (1998).

[76] S. Limandri *et al.*, Chem. Phys. **367**, 93 (2010).

[77] S. D. Gamblin and D. S. Urch, Jour. El. Spectrosc. Rel. Phenom. **11**, 179 (2001) and references therein.

[78] J. P. Desclaux, *A Relativistic Multiconfiguration Dirac-Fock Package*, Methods and Techniques in Computational Chemistry, edited by E. Clementi, (STEF, Cagliari, 1993), Vol. A: Small Systems of METTEC, 253.

[79] B. Fricke and K. Rashid, priv. comm.

[80] J. Anton. et. al., J. Phys. B (At. Mol. Opt. Phys.) **40**, 2453 (2007).

[81] W. Jauch, J. R. Schneider, and H. Dachs, Solid State Comm. **48**, 907 (1983).

[82] B. Gilbert et al., J. Chem. Phys. **107**, 2839 (2003).

[83] C. Cheng and S. Wang, Acta Cryst. C **47**, 1734 (1991).

[84] M. A. Hepworth and K. H. Jack, Acta Cryst. **10**, 345 (1957).

[85] S. Geller, Acta Cryst. B **21**, 821 (1971).

[86] R. Norrestam, Ac. Chem. Scand. **21**, 2871 (1967).

[87] W. H. Baur, Acta Cryst. B **32**, 2200 (1976).

[88] J. Palenik, Inorg. Chem. **6**, 503 (1967).

[89] C. J. Batty *et al.*, Nucl. Instr. Meth. 137 (1976) 179.

[90] HEIDENHEIN IK-220 module user manual;
http://irtfweb.ifa.hawaii.edu/tcs3/tcs3/vendorinfo/Heidenhain/IK220/IK220en.pdf

[91] NI PCI-7334 4 axis stepper motion controller user manual;
http://www.ni.com/pdf/manuals/322504b.pdf

[92] NI PCI-7774 4 Axis Univeral Motion Interface;
http://www.ni.com/pdf/manuals/373359c.pdf

[93] N. Dolfus, Stepper-Endstufen, priv. comm.

[94] S. Katzir, The beginnings of Piezoelectricity, Springer (2006).

[95] Capacitive Proximity Sensors, Theory of Operation;
http://www.softnoze.com/downloads/Sensor%20Basics%203.pdf

[96] Grundlagen zur Pržisions-Temperaturmessung mit PT-100;
https://www.greisinger.de/

[97] COMBIVAC CM 31, LEYBOLD VACUUM;
http://dps-vakuum.de/BetriebsAnleitung/Betriebsanleitung_COMBIVAC_CM31.pdf

[98] Fieldpoint FP-1001 RS-485 Network Module user manual;
http://www.ni.com/pdf/manuals/370706a.pdf

[99] Fieldpoint FP-DO-401 16-Channel, 5 to 30 V Discrete Output Module user manual;
http://www.ni.com/pdf/manuals/371886a.pdf

[100] Fieldpoint FP-AO-200 8-Channel, 20 mA Loop Output Module user manual;
http://www.ni.com/pdf/manuals/323343a.pdf

[101] Fieldpoint FP-AI-110 8-Channel, 16-Bit Analog Input Module user manual;
http://www.ni.com/pdf/manuals/373280b.pdf

[102] Fieldpoint FP-RTD-122 8-Channel, 3-Wire RTD and Resistance Input Module user manual;
http://www.ni.com/pdf/manuals/373348b.pdf

ERKLÄRUNG

Ich versichere, dass ich die von mir vorgelegte Dissertation selbständig angefertigt, die benutzten Quellen und Hilfsmittel vollständig angegeben und die Stellen der Arbeit - einschliesslich Tabellen, Karten und Abbildungen -, die anderen Werken im Wortlaut oder dem Sinn nach entnommen sind, in jedem Einzelfall als Entlehnung kenntlich gemacht habe; dass diese Dissertation noch keiner anderen Fakultät oder Universität zur Prüfung vorgelegen hat; dass sie - abgesehen von unten angegebenen Teilpublikationen - noch nicht veröffentlicht worden ist, sowie, dass ich eine solche Veröffentlichung vor Abschluss des Promotionsverfahrens nicht vornehmen werde.

Die Bestimmungen der Promotionsordnung sind mir bekannt. Die von mir vorgelegte Dissertation ist von Prof. Dr. D. Gotta betreut worden.

Publikationen

[1]. M. Jabua, D. Gotta, Th. Strauch, Ch. Weidemann, B. Fricke, K. Rashid, **Kα X-ray emission in manganese compounds**, Spectrochimica Acta Part B: Atomic Spectroscopy, **doi:10.1016/j.sab.2016.04.006**

LEBENSLAUF

Persönliche Daten	
Name:	Malkhaz Jabua
Gebursdatum:	29.04.1988
Geburtort:	Zugdidi, Georgien
Staatsangehörigkeit:	Georgisch
Familienstand:	Ledig

Promotionsstudium	
seit November 2012	Forschungszentrum Jülich
	Universität zu Köln
Doktorarbeit	Ultimate Resolution X-ray Spectroscopy of Chemical-Effects in Manganese Compounds

Studium	
Oktober 2009 - Juli 2011	Master der Informatik der Staatlichen
	Technischen Universität Georgiens
	Tiflis, Georgien
	Gesamtnote: "mit Auszeichnung"
Masterarbeit	Readout Upgrade for the focal Plane Detector of the Jülich Bragg Spectrometer
Oktober 2005 - Juli 2009	Bachelor der Informatik der Staatlichen
	Technischen Universität Georgiens
	Tiflis, Georgien
	Gesamtnote: "mit Auszeichnung"

Schulbildung	
September 1994 - Juni 2005	Schule #1, Zugdidi, Georgien
	Gesamtnote: "mit Auszeichnung"